
Dissertation

# Spaceborne imaging spectroscopy of the three phases of water

## - Assessment of joint inverse methods -

*Author:*
**Niklas Bohn**

*A thesis submitted in fulfillment of the requirements for the degree of Dr. rer. nat.*

*in the*

Radiation and Remote Sensing Group
Institute of Meteorology
Department of Earth Sciences

Berlin, 2021

Erstgutachter: Prof. Dr. Jürgen Fischer
Zweitgutachter: Prof. Dr. Luis Guanter
Drittgutachterin: Prof. Dr. Kerstin Schepanski

Tag der Disputation: 08. Juni 2022

# Eigenständigkeitserklärung

Hiermit versichere ich, dass ich die vorliegende Arbeit selbstständig verfasst und keine anderen als die angegebenen Quellen und Hilfsmittel benutzt habe. Die Arbeit wurde in keinem früheren Promotionsverfahren eingereicht.

Potsdam, 26.12.2021

Niklas Bohn

# Abstract

Water is one of the most essential substances on Earth as it occurs in all three thermodynamic phases both in the atmosphere and the surface: solid water in terms of snow and ice grains, liquid water enclosed in-between ice crystals and leaves of vegetation, and gaseous water forming the water vapor in the atmosphere. The different phases of water control large amounts of the environmental energy cycle and a quantitative mapping on a global scale is of particular importance as it provides a valuable input to climate models and helps to understand underlying processes. The three phases of water show subtle differences in absorption shape in the optical range of the solar spectrum, so that a quantitative mapping requires high-resolution measurements of solar radiation reflected from Earth's surface. The technique of imaging spectroscopy provides such measurements, but has been almost entirely applied to small local scales based on airborne sensors. However, a new generation of orbital missions, including the Italian Hyperspectral Precursor of the Application Mission (PRISMA), NASA's Earth Surface Mineral Dust Source Investigation (EMIT), the German Environmental Mapping and Analysis Program (EnMAP), ESA's Copernicus Hyperspectral Imaging Mission (CHIME), and NASA's Surface Biology and Geology (SBG) designated observable, is expected to deliver high-resolution data both on a global scale and daily basis. This requests for independently applicable retrieval algorithms including a rigorous quantification of uncertainties. In this context, this thesis presents two new spectroscopic retrieval methods to quantify the three phases of water from space, which are aligned with future instrument characteristics, adapted to an increased atmospheric path as well as to a different ground sampling distance. Both algorithms use the optimal estimation formalism that assumes Gaussian error distribution and leverages prior knowledge as well as measurement noise in an inversion scheme that also produces posterior uncertainty estimates. The first method couples atmospheric radiative transfer simulations from the MODTRAN code to a surface reflectance model based on the Beer-Lambert law. A unique coupling of the 3D Hyperspectral Simulation of Canopy Reflectance (HySimCaR) model and the EnMAP end-to-end Simulation tool (EeteS) is exploited for a sensitivity analysis of estimated vegetation liquid water content. Furthermore, the retrieved values are validated with concurrent field measurements of canopy water content. The second algorithm is based on a

simultaneous retrieval of atmosphere and surface state and exploits statistical relationships between reflectance spectra and additional surface parameters to estimate their most probable quantities. Retrieved snow and ice properties are investigated based on a sensitivity analysis and validated with laboratory and field measurements from the Greenland Ice Sheet. Finally, the applicability of the proposed methods to forthcoming spaceborne imaging spectrometers is demonstrated on the example of PRISMA cryosphere observations by providing retrieval maps of surface liquid water and ice grain size as well as associated retrieval uncertainties. The results from this thesis show that spaceborne imaging spectroscopy permits improved atmospheric water vapor estimations, facilitates a prediction of vegetation drought stress and wildfire potential, and contributes to the understanding of biophysical processes on Earth's Ice Sheets in the context of climate change. Concurrently, three key aspects have been identified to be of particular importance for globally applicable retrieval algorithms: (i) considering topographic characteristics, such as surface slope and aspect as well as sky view factor and shadow fraction, (ii) integrating directional effects depending on illumination and observation conditions, (iii) accounting for mixed pixels by determining influences from background reflectance and fractional cover. Overall, this thesis demonstrates that upcoming launches of several imaging spectroscopy missions open new perspectives in regularly monitoring and mapping atmosphere and surface properties including the three phases of water on a global scale. These maps will provide a valuable input to the modeling of biological and physical processes that help to better understand climate change and to predict and adapt to its socioeconomic consequences.

# Zusammenfassung

Wasser ist eine der wichtigsten Substanzen auf der Erde, da es in allen drei thermodynamischen Phasen sowohl in der Atmosphäre als auch auf der Oberfläche vorkommt: festes Wasser in Form von Schnee und Eiskörnern, flüssiges Wasser zwischen Eiskristallen und als Bestandteil von Pflanzenblättern sowie gasförmiges Wasser, das den Wasserdampf in der Atmosphäre bildet. Die verschiedenen Wasserphasen steuern große Teile des ökologischen Energiekreislaufes, so dass eine quantitative Kartierung auf globaler Ebene von besonderer Bedeutung ist. Sie leistet außerdem einen wertvollen Beitrag zur Klimamodellierung und hilft, die zugrunde liegenden Prozesse besser zu verstehen. Die drei Phasen des Wassers weisen feine Unterschiede in ihrer Absorptionsform im optischen Bereich des solaren Spektrums auf, so dass eine quantitative Bestimmung hochauflösende Messungen der von der Erdoberfläche reflektierten Sonnenstrahlung erfordert. Die Technik der abbildenden Spektroskopie liefert solche Messungen, wurde aber bisher fast ausschließlich auf der Grundlage von flugzeuggestützten Sensoren auf kleinen lokalen Skalen angewandt. Eine neue Generation von Weltraummissionen, darunter die italienische Hyperspectral Precursor of the Application Mission (PRISMA), die Earth Surface Mineral Dust Source Investigation (EMIT) der NASA, das deutsche Environmental Mapping and Analysis Program (EnMAP), die Copernicus Hyperspectral Imaging Mission (CHIME) der ESA und das NASA Surface Biology and Geology (SBG) Observable, soll jedoch hochauflösende Daten sowohl auf globaler Ebene als auch auf täglicher Basis liefern. Dies erfordert unabhängig anwendbare Kartierungsalgorithmen einschließlich einer präzisen Quantifizierung der Unsicherheiten. In diesem Zusammenhang werden in dieser Arbeit zwei neue spektroskopische Methoden zur Quantifizierung der drei Phasen von Wasser aus dem Weltraum vorgestellt, die auf die zukünftigen Instrumentencharakteristika abgestimmt sind und sowohl an einen längeren Weg der Strahlung durch die Atmosphäre als auch an eine andere räumliche Auflösung auf dem Erdboden angepasst sind. Beide Algorithmen verwenden den Formalismus der Maximum-a-posteriori-Schätzung, der von einer Gauß'schen Fehlerverteilung ausgeht und sowohl Vorwissen als auch Messrauschen in einem Inversionsschema nutzt, das zusätzlich a posteriori Unsicherheitsschätzungen liefert. Bei der ersten Methode werden atmosphärische Strahlungstransfersimulationen aus

dem MODTRAN-Code mit einem auf dem Beer-Lambert-Gesetz basierenden Oberflächenreflexionsmodell gekoppelt. Eine einzigartige Kopplung des 3D Hyperspectral Simulation of Canopy Reflectance (HySimCaR) Systems und des EnMAP end-to-end Simulationstools (EeteS) wird für eine Sensitivitätsanalyse des geschätzten Flüssigwassergehalts von Vegetation genutzt. Außerdem werden die ermittelten Werte mit gleichzeitigen Feldmessungen des Wassergehalts von Vegetationskronen validiert. Der zweite Algorithmus basiert auf der simultanen Ermittlung des Zustands von Atmosphäre und Oberfläche und nutzt statistische Beziehungen zwischen Reflexionsspektren und zusätzlichen Oberflächenparametern, um deren wahrscheinlichste Größen zu schätzen. Die ermittelten Schnee- und Eiseigenschaften werden auf der Grundlage einer Sensitivitätsanalyse untersucht und mit Labor- und Feldmessungen vom grönländischen Eisschild validiert. Abschließend wird die Anwendbarkeit der vorgeschlagenen Methoden auf die kommenden weltraumgestützten abbildenden Spektrometer am Beispiel von PRISMA Aufnahmen von Schnee- und Eisflächen demonstriert, indem Karten von Flüssigwasser und Eiskorngröße sowie die damit verbundenen Unsicherheiten dargestellt werden. Die Ergebnisse dieser Arbeit zeigen, dass die weltraumgestützte abbildende Spektroskopie verbesserte Abschätzungen des atmosphärischen Wasserdampfs ermöglicht, die Vorhersage von Pflanzenstress und Waldbrandgefahr erleichtert und zum Verständnis der biophysikalischen Prozesse auf den Eisschilden der Erde im Zusammenhang mit dem Klimawandel beiträgt. Gleichzeitig werden drei Schlüsselaspekte identifiziert, die für global anwendbare Kartierungsalgorithmen von besonderer Bedeutung sind: (i) die Berücksichtigung topographischer Merkmale, wie z.B. Oberflächenneigung und -aspekt sowie Himmelslichtquotient und Schattenanteil, (ii) die Integration von Richtungseffekten in Abhängigkeit von Beleuchtungs- und Beobachtungsbedingungen, (iii) die Berücksichtigung von Mischpixeln durch die Bestimmung von Einflüssen der Hintergrundreflexion und des Bedeckungsgrades. Insgesamt zeigt diese Arbeit, dass die bevorstehenden Starts mehrerer abbildender Spektroskopiemissionen neue Perspektiven für die regelmäßige Überwachung und Kartierung von Atmosphären- und Oberflächeneigenschaften, einschließlich der drei Phasen des Wassers, auf globaler Ebene eröffnen. Diese Karten werden einen wertvollen Beitrag zur Modellierung biologischer und physikalischer Prozesse leisten, die zu einem besseren Verständnis des Klimawandels und zur Vorhersage und Anpassung an seine sozioökonomischen Folgen beiträgt.

# Contents

# Chapter 1

# Introduction

## 1.1 Rationale and structure

Water is one of the most essential substances on Earth and controls large amounts of the environmental energy cycle (Green et al., 2006). It occurs in all three phases both in Earth's atmosphere and on its surface: solid water in terms of snow and ice grains, liquid water enclosed in-between ice crystals and leaves of vegetation, and gaseous water forming the water vapor in the atmosphere. Water in its different states is of significant importance in a diverse field of scientific disciplines. Atmospheric water vapor is the main absorbing greenhouse gas in the infrared (IR) wavelength region, where most of the terrestrial radiation is emitted, and affects a multitude of climate feedback mechanisms (Kiehl and Trenberth, 1997; Trenberth, Fasullo, and Kiehl, 2009; Diedrich et al., 2013). Liquid water is a significant driver of agricultural and ecological processes on vegetated surfaces and is an important indicator for plant physiological status and health as well as for wildfire potential (Schulze and Hall, 1982; Clevers, Kooistra, and Schaepman, 2010; Liu, Stanturf, and Goodrick, 2010; Pasqualotto et al., 2018). Snow and ice properties control physical and biological processes on polar ice sheets and mountainous glaciers, which strongly affect the net solar radiation that regulates melt processes and the associated impacts on sea level rise (Flanner and Zender, 2006; Painter et al., 2012; Bamber et al., 2018; Ryan et al., 2018). Thus, a quantitative mapping of water in its three states on a global scale is of particular importance as it provides a valuable input to climate models and helps to understand underlying processes.

In this context, the objective of this thesis is to assess the potential of advanced spaceborne imaging spectroscopy to improve the detection and quantification of the three phases of water on Earth's surface. So far, this technique has been almost entirely based on airborne spectrometers, but a new era of orbital missions will deliver high-resolution data both on a global scale and daily basis, which requests for independently applicable retrieval algorithms (Cawse-Nicholson et al., 2021).

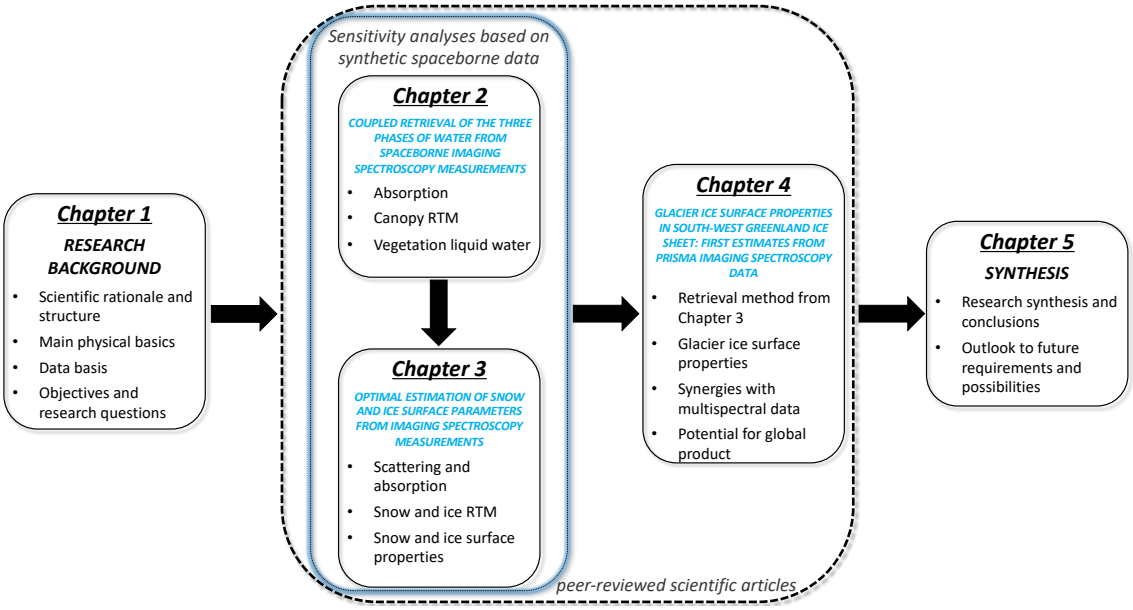


FIGURE 1.1: Schematic overview of thesis structure (for more detail, please see Sections 1.3 and 1.5).

Thus, the inauguration of new methods aligned with future instrument characteristics, adapted to an increased atmospheric path as well as to a different ground sampling distance is an important task for the upcoming decade and is pursued in this work. The desired outcome of such algorithms is a robust global product that maps atmospheric water vapor, vegetation liquid water content as well as snow and ice surface properties corrected for latitudinal and topographic biases including a rigorous quantification of uncertainties.

The thesis is divided into five main chapters. Chapter 1 introduces the general research background by providing the scientific rationale, presenting the main physical basics, and formulating the objectives and research questions pursued in this work. Chapters 2 - 4 include consecutive self-contained manuscripts, whose ancillary objectives contribute to answering the main research questions of the overall thesis. Chapter 2 presents a new coupled retrieval algorithm for the three phases of water with a detailed assessment of quantifying vegetation liquid water content, Chapter 3 introduces an extension to a novel joint atmosphere and surface retrieval focusing on the estimation of snow and ice properties, and Chapter 4 presents an application of the new methods to already existing spaceborne imaging spectroscopy acquisitions. Chapter 5 summarizes and discusses the main findings from Chapters 2 - 4, and suggests future research perspectives. Figure 1.1 illustrates the outline of the thesis and shows the main contributions of each chapter, whereas specific contributions and objectives of the individual manuscripts are presented in more detail in Sections 1.3 and 1.5.

## 1.2 Background

This section provides an overview about the radiative and optical properties of water in its different states (Section 1.2.1) and state-of-the-art spaceborne optical remote sensing of the three phases of water in general (Section 1.2.2). Finally, Section 1.2.3 outlines the potential of imaging spectroscopy in the face of novel opportunities provided by present and upcoming spaceborne missions to simultaneously estimate water in its different states.

### 1.2.1 Radiative and optical properties of water

The interactions of electromagnetic radiation with water in its different states are controlled by both the radiative and optical properties of the three phases. The radiative properties are also called 'optical constants' and comprise the wavelength dependent refractive index and absorption coefficient. They form the complex index of refraction $N_\lambda$ (Petty, 2004):

$$N_\lambda = n_\lambda + ik_\lambda, \tag{1.1}$$

where $n_\lambda$ is the real part determining the effective phase speed of electromagnetic waves that propagate through the medium, and $k_\lambda$ is the imaginary part that expresses the absorption of photons and is directly related to the absorption coefficient $\alpha_\lambda$ by:

$$\alpha_\lambda = \frac{4\pi k_\lambda}{\lambda}. \tag{1.2}$$

While $n_\lambda$ only marginally varies in the visible (VIS) and near-infrared (NIR) spectral region, $k_\lambda$ and consequentially, $\alpha_\lambda$, change by up to seven orders of magnitude (Green et al., 2006) (Figure 1.2). In this wavelength range, water absorption is mainly caused by molecular vibration that is composed of the fundamental modes of bending and both symmetric and asymmetric stretch as well as overlapping overtones that can be found in the mediumwave infrared between 3000 and 6000 $nm$ (Green et al., 2006; Warren, 2019). Although these intramolecular vibrational modes also influence the water vapor absorption, Figure 1.2 illustrates that $\alpha_\lambda$ of the gaseous phase clearly differs from those of the liquid and solid phases. We observe comparatively moderate absorption energies of liquid water and ice in contrast to the much stronger attenuation of photons by water vapor (Green et al., 2006). This weaker absorption of both liquid and solid phases is caused by an increased formation of hydrogen bonds between the molecules and a resulting weaker O-H bonding strength of liquid water and ice (Gao, 1996; Green et al., 2006). It has to be noted that water features no distinct absorption mechanism in the VIS spectral range, but noticeable

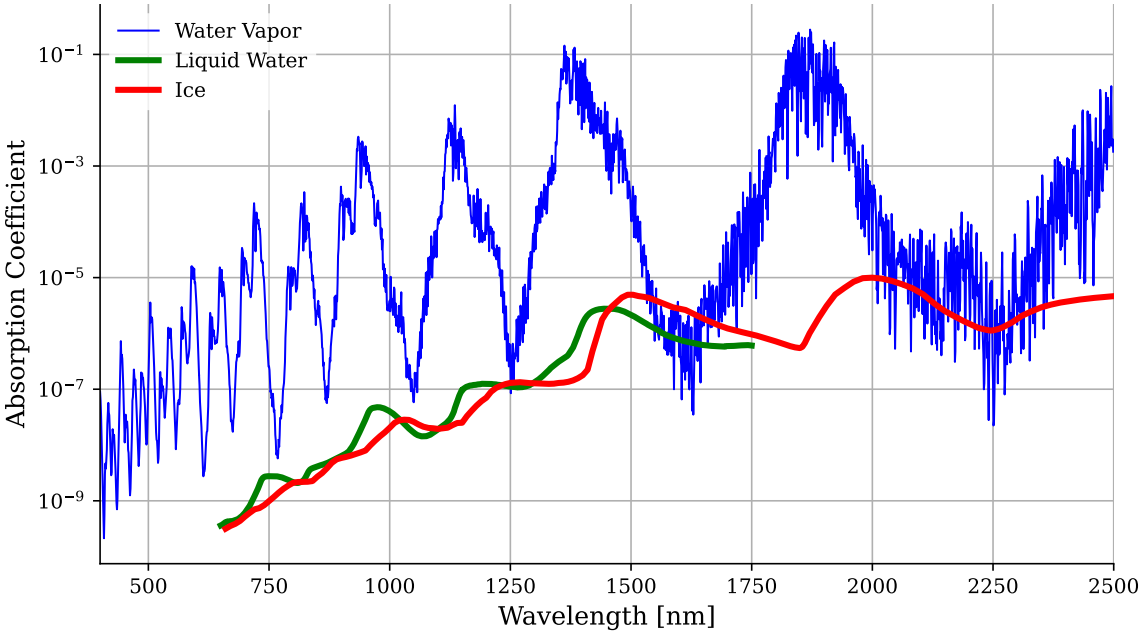


FIGURE 1.2: Absorption coefficients of different water phases in the VIS, NIR, and shortwave-infrared (SWIR) solar spectrum, calculated from the HITRAN database on a 1 *nm* grid in case of water vapor (Kochanov et al., 2016), and taken from Kedenburg et al. (2012) and Warren and Brandt (2008), respectively, in case of liquid water and ice. The spectral sampling interval is 1 *nm* for liquid water and 10 *nm* for ice. The lines of liquid water and ice are not plotted over the whole optical wavelength range due to limited data availability in the mentioned references. Note the logarithmic scale of the y-axis.

weakening of electromagnetic waves is induced by emanating molecular vibration from the NIR. $\alpha_\lambda$ even reaches a value close to zero in the VIS blue wavelengths below 500 *nm* (Warren, 2019). Figure 1.2 likewise highlights the difference between the absorption lines of liquid water and ice in terms of a slight shift of the solid water absorption coefficients towards longer wavelengths (Green et al., 2006). However, the spectral shapes are very similar and exhibit characteristically smooth gradients, which facilitates accurate calculations even based on a coarse spectral resolution. Such smoothness is provoked by a high frequency of intermolecular collisions leading to a significant line broadening (Warren, 2019). In contrast, a smaller spectral sampling interval is needed for simulations of water vapor absorption due to the finer spectral line structures. They arise from different rotational states of gaseous water (Green et al., 2006; Warren, 2019).

The optical properties of water generally include absorptance, transmittance, reflectance, and emissivity of the different phases (Warren, 2019). These optical functions depend on how solar radiation interacts with a medium. Contingent on the spatial extent of sub-scale matter particles, the electromagnetic waves remain either nearly unaffected in case of particles being much smaller than the wavelength,

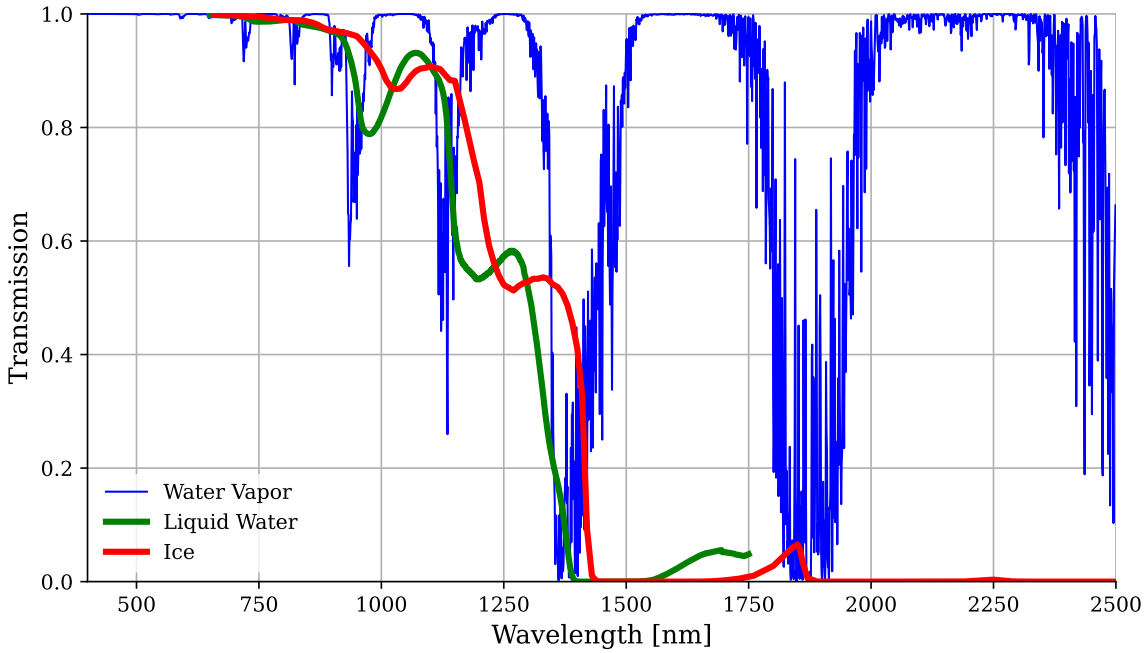


FIGURE 1.3: Transmission spectra of the three phases of water based on the absorption coefficients displayed in Figure 1.2. The spectrum of water vapor is calculated for 25 $mm$ columnar water vapor. The spectra of liquid water and ice are calculated assuming optical path lengths of 5 $mm$.

or experience varying magnitudes of attenuation at particles of much larger size relative to the wavelength (Warren, 1982). Figure 1.3 shows characteristic transmission spectra of the three phases of water calculated for 25 $mm$ atmospheric columnar water vapor (CWV) and 5 $mm$ of liquid water and ice optical path lengths, respectively. Again, the displacement of the absorption coefficients as well as the different magnitudes of absorption energies are clearly observable. Both properties therefore form the basic principles of a spectroscopic separation of the three phases (Green et al., 2006).

Transmission not only depends on the absorption coefficients but also on the amount of water the photons are passing through. Several different units exist to quantify water in its three states. Amongst others, water vapor can be classified in $mm$ being the integral of specific humidity over the vertical column (Diedrich, 2016), or as the amount of precipitable water in $g\ cm^{-2}$ available in the atmosphere (Guanter, Gomez-Chova, and Moreno, 2008a). Liquid water in vegetation is either indicated as liquid water content in $g\ cm^{-2}$ or as equivalent water thickness in $mm$, which is the leaf or canopy water optical path length (Hunt, Ustin, and Riano, 2013). In addition to the expression as optical path length, liquid water in snow may also be quantified as fraction of snow grain radius (Green et al., 2002; Green et al., 2006). Finally, snow and ice surfaces are commonly characterized by the effective grain radius in $\mu m$ or the specific surface area (Warren, 1982). Alternatively, the

solid water phase can also be parameterized as optical path length in *mm* (Green et al., 2006). Throughout this work, the use of different units for parameterizing water in its different states is assessed depending on the applied retrieval methods.

### 1.2.2 Optical remote sensing of the three phases of water

Optical remote sensing is based on measurements of the solar radiation reflected by atmosphere and surface components and covers the VIS, NIR, and SWIR part of the solar spectrum featuring a wavelength range from 400 to 2500 *nm* (Goetz et al., 1985). Numerous multispectral or medium resolution satellite instruments operate on this technique, which is a valuable tool to obtain spatial distribution of the three phases of water on a global scale with a high temporal resolution. For instance, the retrieval of columnar water vapor is a standard routine included in atmospheric correction algorithms for remote sensing data and a multitude of various methods exist to detect vegetation liquid water content as well as snow and ice on the surface. The basic contributions of the three phases of water to an optical remote sensing measurement from space are presented on the example of imaging spectroscopy in Section 1.2.3 (see Figure 1.4).

Initially, atmospheric water vapor has been commonly retrieved from satellites using the thermal infrared (TIR) region of the electromagnetic spectrum, until Gao et al. (1993) presented the idea to use instrument channels around the 940 *nm* NIR absorption feature for remotely sensing precipitable water. This method has been established for retrievals from the MEdium Resolution Imaging Spectrometer (MERIS), the moderate resolution imaging spectroradiometer (MODIS), or the Sentinel-3 Ocean and Land Colour Instrument (S3 OLCI) (Bennartz and Fischer, 2001; Albert et al., 2005; Guanter, Gomez-Chova, and Moreno, 2008a; Lindstrot et al., 2012; Diedrich et al., 2015; Preusker, Carbajal Henken, and Fischer, 2021). But also multispectral sensors such as Sentinel-2 can be used for retrieving atmospheric water vapor using only two spectral instrument channels (Makarau et al., 2017). Prominent NIR retrieval algorithms include the Continuum Interpolated Band Ratio (CIBR) and the Atmospheric Precorrected Differential Absorption technique (APDA) (Carrere and Conel, 1993; Schlaepfer et al., 1998). Other approaches are based on measurements in the VIS spectral range by using observations from sensors such as the Ozone Monitoring Instrument (OMI) or the Global Ozone Monitoring Experiment 2 (GOME-2) (Noël et al., 2002; Wagner et al., 2006; Wagner et al., 2013). Ultimately, Frankenberg et al. (2013) introduced a method of using the SWIR spectral range to estimate the isotopic composition of water vapor from the GOSAT instrument.

Likewise, a couple of different methods exist to retrieve liquid water from spaceborne optical remote sensing data. They mainly concentrate on vegetated surfaces by presenting approaches to quantify leaf or canopy water content. However, the most common way is to use empirical band indices that relate surface reflectance to vegetation water content and can only be used as a proxy for physical quantities. The first suggestion for such an index was published by Hardisky, Klemas, and Smart (1983). They presented the Infrared Index that compares the SWIR with the NIR reflectance and was developed based on multispectral data from the Landsat 4 and 5 Thematic Mappers (TM). Using the same Landsat bands, also the Leaf Water Stress Index was introduced (Hunt, Rock, and Nobel, 1987; Hunt and Rock, 1989). Gao (1996) developed the Normalized Difference Water Index (NDWI) that compares the high reflectance plateau of vegetation at 860 $nm$ and the water absorption feature at 1240 $nm$ using MODIS data. This index was also applied to Landsat and Sentinel-2 data analyzing the water content of agricultural crops (Jackson et al., 2004; Zhang et al., 2017). Instead of empirical band indices, an alternative method to estimate vegetation liquid water content is a physically-based inversion of radiative transfer models such as the widely used PROSAIL model (Jacquemoud et al., 2009). Several studies presented inversion techniques based on deep learning algorithms such as neural networks and applied these approaches to MODIS data or assessed the potential of observations from the high-resolution CHRIS-PROBA satellite (Trombetti et al., 2008; Cernicharo, Verger, and Camacho, 2013).

Finally, the mapping of snow properties was among the earliest geophysical retrieval methods from spaceborne optical remote sensing data (Rango and Itten, 1976). The potential of the NIR wavelength region to estimate grain size was already demonstrated in the early 80's based on measurements from the NOAA Advanced Very High Resolution Radiometer (AVHRR) (Dozier, Schneider, and Jr., 1981). In particular, data from the Landsat TM satellite were then used to map snow cover and grain size (Dozier and Marks, 1987; Dozier, 1989). Dozier (1989) also introduced the Normalized Difference Snow Index (NDSI) that was later on used for generating the standard snow product from MODIS acquisitions (Hall, Riggs, and Salomonson, 1995). Prominent subsequent algorithms used for retrieving snow cover and grain size include algorithms based on observations from MODIS and S3 OLCI (Zege et al., 2008; Sirguey, Mathieu, and Arnaud, 2009; Zege et al., 2011; Carlsen et al., 2017; Kokhanovsky et al., 2019).

In general, previously developed retrieval methods for the three phases of water based on optical remote sensing from space are limited both in accuracy and spatial scale due to the characteristics of existing instruments (for exemplary specifications, see Table 1.1). Despite featuring a very high spectral resolution, OMI and

GOME-2 only cover the VIS and have large footprints with magnitudes of several kilometers. MERIS, MODIS, and S3 OLCI provide ground sampling distances of $250 - 1000\ m$, but feature only 16, 36, and 21 spectral channels, respectively. On the other hand, CHRIS-PROBA is limited to the range of 400 to 1000 $nm$ and has less quality in radiometric calibration. Multispectral sensors such as Landsat and Sentinel-2 provide an even smaller number of bands than MERIS, MODIS, or S3 OLCI. As a consequence, the majority of retrieval algorithms is just empirical, cannot provide numbers in physical units, and is potentially confounded by other factors similarly impacting the multispectral spectrum. Inferring local variations of atmospheric water vapor on small spatial scales and determining the exact amounts of surface liquid water and snow and ice is therefore challenging using existing optical spaceborne technology. Moreover, all the above-mentioned retrieval methods are designed for quantifying water in only one of its three states since existing spaceborne sensors do not come with the technical prerequisites to spectroscopically separate and quantify the three phases of water simultaneously, which would significantly improve the accuracy of estimated quantities. For instance, decoupling liquid and solid water absorption from the gaseous phase leads to less uncertainty in atmospheric water vapor maps over vegetated and snow-covered terrain (Thompson et al., 2015). Furthermore, a coupled retrieval increases the accuracy of liquid water estimates on snow and ice surfaces leading to improved prediction of melt rates and processes (Green et al., 2006). Finally, retrieval uncertainties and error correlation between all three phases could precisely be quantified using a simultaneous approach facilitating a better evaluation of the estimated values. Advanced high-resolution imaging spectroscopy helps toward facing these challenges and achieving these objectives as exemplified in the following section.

### 1.2.3 Imaging spectroscopy

In contrast to multispectral or medium resolution technologies, the new generation of spaceborne imaging spectrometers features both contiguous channels with a high spectral sampling interval along the complete optical range from even 380 to 2500 $nm$ and a high-resolution footprint of around 30 $m$ (Cawse-Nicholson et al., 2021) (Table 1.1). Due to these specifications, spectroscopic measurements can be used to accurately quantify land, water, and atmosphere constituents using physically-based retrievals by modeling characteristic atmosphere and surface absorption features. Imaging spectroscopy can be applied to a wide range of different scientific disciplines in Earth Observation (EO) such as quantification of atmospheric greenhouse gases and aerosols, monitoring vegetation phenology, soil and mineral mapping, estimating snow and ice surface properties, as well as retrieval of water constituents

TABLE 1.1: Relevant characteristics of exemplary operating satellite instruments in comparison to the new generation of imaging spectrometers. The specifications are collected from Masek et al. (2020), Justice et al. (2002), Munro et al. (2006), Barducci et al. (2005), and Cawse-Nicholson et al. (2021).

| | **Multispectral** (e.g., Landsat) | **Medium resolution** (e.g., MODIS) | **High resolution VIS** (e.g., GOME-2) | **High resolution VNIR** (e.g., CHRIS-PROBA) | **New generation of imaging spectroscopy** |
|---|---|---|---|---|---|
| Data availability | 1972-present | 1999-present | 2006-present | 2001-present | 2018-present |
| Nadir pixel size [km] | 0.015-0.03 | 0.25-1 | 40 | 0.017-0.034 | 0.03 |
| Swath width [km] | 185 | 2330 | 960 | 14 | 30 |
| Revisit time [days] | 8 | 1-2 | 1.5-3 | 7 | 16 |
| Spectral coverage [nm] | 430-2290 | 405-2155 | 240-790 | 400-1050 | 380-2500 |
| Spectral resolution [nm] | 207 | 92 | 0.2-0.4 | 1.25-11 | $< 10$ |
| Signal-to-noise ratio (SNR) | $< 540$ | $< 1087$ | $< 1000$ | $< 140$ | $< 500$ |

over inland water bodies, coastal areas and open ocean (Schaepman et al., 2009). In particular, high-resolution imaging spectroscopy measurements enable a separation and quantification of water in its three states (Green et al., 2006; Painter et al., 2013). In a simplified way, Figure 1.4 illustrates the contributions of the three phases of water to such measurements from space over vegetated and snow-covered surfaces. Thereby, the spectral top-of-atmosphere (TOA) radiance received by the instrument is a particular portion of the incoming TOA solar irradiance that is reflected by atmosphere and surface components. On the path from the sun to the sensor, the atmospheric transmission of solar photons is mainly determined by water vapor, whereas liquid water and ice form characteristic absorption features of the surface reflectance. Additional contributors to the TOA radiance signal such as atmospheric path radiance, spherical albedo, or topographic and adjacency effects are not included in the sketch, but ideally have to be considered in an accurate retrieval scheme as well. Using a simplified solution of the radiative transfer equation, the wavelength-dependent TOA radiance can be formulated as (Chandrasekhar, 1960):

$$L_{\mathrm{TOA}}(\lambda) = L_0(\lambda) + \frac{1}{\pi}\frac{\rho_{\mathrm{s}}(\lambda)(E_{\mathrm{dir}}(\lambda)\mu_{\mathrm{sun}} + E_{\mathrm{dif}}(\lambda))T_{\uparrow}(\lambda)}{1 - S(\lambda)\rho_{\mathrm{s}}(\lambda)}, \tag{1.3}$$

where $L_0$ is the atmospheric path radiance; $E_{\mathrm{dir}}$ and $E_{\mathrm{dif}}$ are the direct and diffuse components of $I_{\mathrm{sol}}$ arriving at the surface; $\mu_{\mathrm{sun}}$ is the cosine of the solar zenith angle; and $S$ is the spherical albedo of the atmosphere.

So far, imaging spectroscopy of the three phases of water has been almost entirely based on field and airborne spectrometers. For instance, Carrere and Conel (1993) applied the method from Gao et al. (1993) to measurements from NASA's Airborne Visible Infrared Imaging Spectrometer (AVIRIS) to retrieve atmospheric water vapor. Based on least squares spectrum-matching techniques, canopy equivalent water thickness was also estimated using spectroscopic AVIRIS data (Gao and Goetz, 1995). Additionally, several studies focused on indices exploiting the 970 $nm$ liquid water absorption feature in the NIR using measurements from field spectrometers or

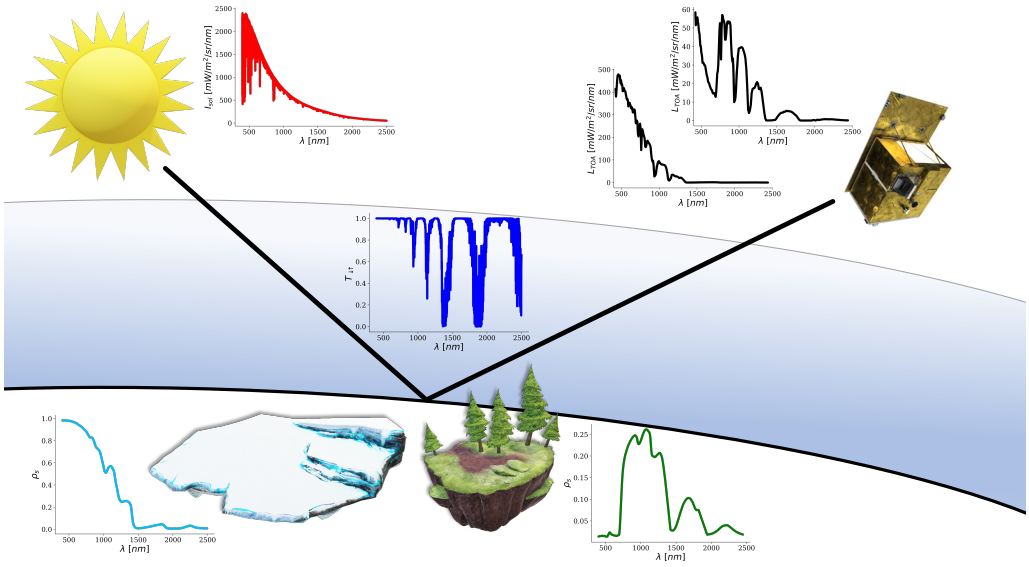

FIGURE 1.4: Contributions of the three phases of water to a high-resolution optical remote sensing measurement from a spaceborne imaging spectrometer over vegetated and snow-covered surfaces under cloud free conditions. Depicted are TOA solar irradiance ($I_{\mathrm{sol}}$), total atmospheric transmission with main contribution from water vapor ($T_{\downarrow\uparrow}$), surface reflectance of both snow and vegetation with characteristic liquid water and ice absorption features ($\rho_{\mathrm{s}}$), and respective TOA radiance received by the satellite sensor ($L_{\mathrm{TOA}}$). Additional contributors to the TOA radiance signal such as atmospheric path radiance, spherical albedo, or topographic and adjacency effects are neglected for simplicity.

the airborne Hyperspectral Mapper (HyMap) to estimate leaf or canopy water content (Peñuelas et al., 1993; Peñuelas et al., 1997; Vohland, 2008; Clevers, Kooistra, and Schaepman, 2008). With the Water Absorption Area Index (WAAI) and the Depth Water Index (DWI), more generally applicable indices were recently developed to assess the liquid water content of agricultural crops based on HyMap observations (Pasqualotto et al., 2018), and Champagne et al. (2003) inverted PROSAIL for retrieving canopy water content based on precalculated look-up-tables (LUT) using the Probe-1 airborne imaging spectrometer. Likewise, spectroscopic retrievals for the cryosphere were mainly developed based on AVIRIS data. One of the first methods for estimating snow grain size exploited the nonlinear relationship between modeled directional reflectance at 1030 *nm* and grain radius (Nolin and Dozier, 1993). This approach was then extended to the full 1030 *nm* ice absorption feature by relating the absorption band area to snow grain radius leading to more robust retrieval results (Nolin and Dozier, 2000). By prior calculating snow subpixel cover, this method was further improved (Painter et al., 2003). To reduce biases from the overlapping water vapor and liquid water absorption, Painter et al. (2013) proposed a spectral fitting method for the 1030 *nm* ice feature, which optimized a modeled snow spectrum to match the reflectance observed by the instrument. Finally, Green

et al. (2002) presented reflectance models for wet snow to retrieve liquid water fraction and tested the approach with measurements from a field spectrometer. To date, this method was never extended to airborne or spaceborne instruments though.

Attempts to simultaneously quantify water in its different states using spectroscopy reach back to the 90's as a few studies introduced a combined water vapor and liquid water retrieval from AVIRIS data (Gao and Goetz, 1990; Green et al., 1991; Gao, 1996). Initially, this approach aimed at improving the performance of atmospheric correction algorithms by decoupling the overlapping absorption of the liquid phase from the stronger vapor line to enhance the accuracy of the derived water vapor maps. The method applies a nonlinear least squares inversion of the MODTRAN radiative transfer model (RTM) (Berk, Bernstein, and Robertson, 1989), linked with a well-parameterized surface reflectance model based on the Beer-Lambert law. It expresses the absorption of incident radiation as a function of the optical path length of liquid water (Born and Wolf, 1959). Later on, this method appeared to be reliable for analyzing vegetation liquid water content (Roberts, Green, and Adams, 1997; Roberts et al., 1998a). However, the first assessment to concurrently infer the amounts of water in all three states was introduced by Green et al. (2006) more than ten years later by accounting for the absorption line of the solid phase in the Beer-Lambert surface model. This approach was further improved by a linear approximation of the inversion technique (Thompson et al., 2015), and applied to measure the thermodynamic phase of clouds (Thompson et al., 2016). Ultimately, Thompson et al. (2018) recently presented a simultaneous retrieval of water vapor, aerosol optical thickness (AOT), and surface reflectance by exploiting all AVIRIS instrument channels covering the whole optical range from the VIS to the SWIR wavelengths. This approach offers promising potential to add further surface parameters such as liquid water as well as snow and ice properties to the state vector.

Imaging spectroscopy of the three phases of water is still limited in spatial and temporal coverage. However, the comprehensive research based on airborne techniques over the past decades laid the bedrock for advancing retrieval methods from airborne sensors to spaceborne instruments. With the launch of the German Aerospace Center's (DLR) Earth Sensing Imaging Spectrometer (DESIS) (Mueller et al., 2016) and the Italian Hyperspectral Precursor of the Application Mission (PRISMA) (Cogliati et al., 2021), a new era of orbital imaging spectrometers was heralded in the years 2018 and 2019, respectively. Both sensors already deliver promising data products and several forthcoming missions are expected to further extend spatial and temporal coverage with daily acquisitions and high-resolution footprints of 30 $m$. Prominent future instruments include NASA's Earth Surface

Mineral Dust Source Investigation (EMIT) (Green et al., 2018), the German Environmental Mapping and Analysis Program (EnMAP) (Guanter et al., 2015), the Copernicus Hyperspectral Imaging Mission (CHIME) led by the European Space Agency (ESA) (Rast et al., 2019), and NASA's Surface Biology and Geology (SBG) designated observable (National Academies of Sciences, Engineering, and Medicine, 2018). The expected unprecedented availability of EO data acquired by these spaceborne imaging spectrometers will raise new possibilities in simultaneously mapping water vapor, liquid water as well as snow and ice properties both on local and on global scale.

## 1.3 Aims and objectives

The general objective of this thesis is to evaluate the potential of a new generation of spaceborne imaging spectroscopy missions to further the detection and quantification of the three phases of water on Earth's surface by introducing novel joint retrieval methods from satellite instruments. In particular, 1) the ongoing climate change demands more frequent high-resolution observations of both vegetated and snow-covered surfaces to assess the role of water in analyses of plant health and the associated potential as a carbon sink as well as in investigations of melting dynamics on glacier ice sheets, and 2) present and forthcoming orbital imaging spectrometers will deliver high-resolution data both on a global scale and daily basis, which requests for an independently applicable precise mapping of the three phases of water. These objectives are addressed by presenting two novel joint retrieval algorithms designed for the application to spaceborne instruments: a coupled retrieval of the three phases of water modeling the absorption of surface liquid water and ice, and the extension to a simultaneous atmosphere and surface inversion relying on accurate simulations of both scattering and absorptive properties of water in its three states. Specifically, the objective of this work aims at a rigorous quantification of retrieval uncertainties by utilizing optimal estimation as inversion technique. For this purpose, the performance of the algorithms is evaluated through sensitivity analyses based on synthetic EnMAP data, and is tested on already existing PRISMA measurements. Furthermore, the potential of new spectroscopic retrievals in concert with multiband data in a comprehensive observation system as well as the capability of the presented algorithms to be scaled to a global product are shown. Methodologically, this research focuses on joint retrieval approaches that exploit 1) the spectral information provided by imaging spectroscopy to differentiate between the three phases of water, and 2) prior knowledge obtained from simulations by vegetation, snow, and ice radiative transfer models. A major step in this work is the quantitative

validation of retrieved canopy water content and snow and ice properties and the assessment of the correlation between atmosphere and surface state and its effect on retrieval uncertainties, as well as an evaluation of the limitations of present and future imaging spectroscopy missions and the applied approaches.

Based on the objectives, the following main research questions will be addressed in this thesis:

(1) Are present and forthcoming orbital imaging spectroscopy missions applicable to robustly map and quantify the three phases of water?

(2) How can spaceborne imaging spectroscopy contribute to the analyses of vegetation dynamics and ice melt processes and their link to climate change?

(3) What are the synergies between imaging spectroscopy from space and observations from existing multiband orbital instruments?

## 1.4 Data basis

This section provides an overview about the remote sensing data and field measurements used to address the objectives and research questions. The sensitivity analyses of Chapters 2 and 3 are based on synthetic EnMAP data. Additionally, the applicability of the modified retrieval algorithms is demonstrated on airborne AVIRIS acquisitions. Both chapters also use selected datasets for validation: Chapter 2 compares field measurements of canopy water content with the results from a concurrent CHRIS-PROBA observation, Chapter 3 validates glacier algae concentration retrieved from field spectrometer based simulated EnMAP data with laboratory measurements. Finally, Chapter 4 applies the method from Chapter 3 to PRISMA data and uses a Sentinel-3 OLCI acquisition for comparison.

**Synthetic spaceborne EnMAP imaging spectroscopy data**
The Environmental Mapping and Analysis Program (EnMAP) is a German high performance EO mission leading to Level 2 products including an open data policy (Guanter et al., 2015). The instrument is a push-broom imaging spectrometer scheduled for launch in 2022. EnMAP will be in sun-synchronous orbit carrying two cameras: a VNIR camera covering $420-1000\ nm$ with a mean spectral sampling interval (SSI) of $6.5\ nm$ and a SWIR camera covering $900-2450\ nm$ with a mean SSI of $10\ nm$. The instrument has a swath width of $30\ km$ and a ground sampling distance

(GSD) of 30 $m$. The mission lifetime is scheduled for 5 years. EnMAP TOA radiances were simulated using the EnMAP end-to-end Simulation tool (EeteS) (Segl et al., 2012) based on two different types of input reflectance spectra. For the vegetation analysis, simulations of canopy reflectance from the 3D Hyperspectral Simulation of Canopy Reflectance system (HySimCaR) (Kuester et al., 2014) are used. For studying snow and ice properties, input spectra were generated with the snow and ice RTM BioSNICAR-GO (Cook et al., 2020). Based on the provided reflectance, EeteS was used to simulate the entire image data acquisition, calibration and processing chain from spatially and spectrally oversampled data to intermediate Level-1A (systematically-corrected) raw data and to the final EnMAP Level-1B products (radiometrically-corrected, spectrally- and geometrically-characterized radiance).

**Spaceborne PRISMA imaging spectroscopy data**

The Hyperspectral Precursor of the Application Mission (PRISMA) is an imaging spectroscopy satellite mission led by the Italian Space Agency (ASI) (Cogliati et al., 2021). The push-broom instrument was launched in March 2019 and provides on-demand data for most of the Earth. It features 239 spectral bands covering the wavelength region from 400 to 2500 $nm$ with an SSI less than 12 $nm$. The GSD is 30 $m$, while the swath is 30 $km$. For the cryosphere study in Chapter 4, an acquisition from August 30, 2020, covering a part of the k-transect on the Greenland Ice Sheet was selected. The official PRISMA L1 TOA radiance product was refined by applying a suite of preprocessing tools, including a spectral smile correction and a radiometric radiance correction (Chlus, Townsend, and Gierach, 2021).

**Spaceborne CHRIS-PROBA imaging spectroscopy data**

The Compact High Resolution Imaging Spectrometer (CHRIS) on the Project for On-Board Autonomy-1 (PROBA-1) satellite is a push-broom imaging spectrometer that still delivers EO data since launch in 2001. The instrument features a swath width of 13.5 $km$ and a GSD of 36 $m$. It has a spectral range covering 410 $nm$ to 1050 $nm$ and an SSI of 1.25 $nm$ (at 400 $nm$) and 11 $nm$ (at 1050 $nm$) (Barducci et al., 2005). The dataset used in Chapter 2 was acquired during the ESA Spectra Barrax Campaign (SPARC'03) in Barrax, Spain, on July 14, 2003. The image covers a mixture of agricultural areas and open soil and extends over $38.97 - 39.13°$N and $2.00 - 2.19°$W.

**Spaceborne medium resolution Sentinel-3 OLCI data**

The Ocean and Land Colour Instrument (OLCI) is a moderate resolution imaging

spectrometer installed on the Sentinel-3 satellite that was launched in 2016. The instrument provides 21 spectral bands spanning 400 to 1020 $nm$ with an SSI between 2.5 and 40 $nm$. With $1,270$ $km$ and 300 $m$, it features relatively large swath and GSD, respectively. OLCI was specifically designed for retrieving chlorophyll content, primarily over ocean surfaces, which is highly facilitated by its large footprint (Malenovský et al., 2012). Chapter 4 utilizes an acquisition from August 30, 2020, 15:00 GMT-2. The scene covers large parts of the western shore of the Greenland Ice Sheet including the k-transect. For the comparison with PRISMA data, the OLCI L1B product providing radiometrically calibrated TOA radiances is used.

**Airborne AVIRIS imaging spectroscopy data**

Both data from the AVIRIS-Classic (AVIRIS-C) and the AVIRIS-Next Generation (AVIRIS-NG) instrument are used in Chapters 2 and 3. AVIRIS-C covers the wavelength range from 380 to 2500 $nm$ with an SSI of 10 $nm$. It features varying GSD due to different flying altitudes (Green et al., 1998). It can be installed on the NASA ER-2 research aircraft so that it is able to acquire data from a height of up to 20 $km$ resulting in a GSD of 20 $m$. The channels of AVIRIS-NG cover the same wavelengths as AVIRIS-C, but with a denser SSI of 5 $nm$. The GSD can vary in the same range as for AVIRIS-C (Hamlin et al., 2011). For studying vegetated surfaces, an AVIRIS-C dataset acquired over a mountainous area in the Sierra Nevada, California, on February 02, 2015 was selected. Two subsets were generated: one containing vegetated agricultural areas and rock surfaces in equal parts covering $35.70-35.76°$N and $118.07-118.13°$W, and another one consisting of partly snow- and forest-covered mountain ranges extending over $35.57-35.65°$N and $118.04-118.13°$W. For assessing the retrieval of snow and ice surface properties in Chapter 3, an AVIRIS-NG image acquired over the Greenland Ice Sheet on August 31, 2019 was selected. Again, two subsets were generated: one capturing a dark ice surface at 66.97°N and 49.12°W, and another one covering a clean snow surface with center coordinates 66.96°N and 46.86°W.

**Field measurements**

Two collections of field data were used in Chapters 2 and 3. For the vegetation analysis, measurements of leaf water content and leaf area index (LAI) were taken from a dataset created during the SPARC03 campaign (Delegido et al., 2013). The data were sampled between July 12 and 14, 2003, at 39.3°N and 2.6°W in Barrax, La Mancha, Spain, and cover multiple crop types, growth phases, canopy geometries and soil conditions. Canopy water content was then obtained by multiplying measured leaf water content with LAI (Clevers, Kooistra, and Schaepman, 2010).

Additionally, field observations from the Greenland Ice Sheet are used to validate remotely retrieved snow and ice properties. The dataset includes reflectance measurements conducted with an Analytical Spectral Device (ASD) FieldSpec Pro 3, and laboratory measurements of glacier algae mass mixing ratios obtained from ice samples taken from within the viewing area of the ASD. The data were collected and provided by Cook et al. (2020) in the frame of the Black and Bloom Project and were sampled from a Greenland field site at 67.04° N and 49.07° W between July 10 and 17, 2017.

## 1.5 Thesis structure and author contribution

This thesis contains an introduction (Chapter 1), three main chapters representing three manuscripts (Chapters 2 - 4), and an overall synthesis and discussion (Chapter 5). Chapters 2 and 3 are original publications that have been published in peer-reviewed scientific journals and Chapter 4 has been submitted to a peer-reviewed scientific journal and is currently under review. All main chapters represent stand-alone independent research. Therefore, some overlapping general information appears between publications, particularly in the description of methods and materials as well as in the introductory sections.

**Chapter 2 - Coupled retrieval of the three phases of water from spaceborne imaging spectroscopy measurements**

*Niklas Bohn, Luis Guanter, Theres Kuester, René Preusker, and Karl Segl.*
*Remote Sensing of Environment, 2020, 242, 111708,*
*https://doi.org/10.1016/j.rse.2020.111708.*

The first published manuscript presents a new coupled retrieval of the three phases of water that builds upon a method from Green et al. (2006). The study focuses on a sensitivity analysis of liquid water retrievals over vegetated surfaces based on synthetic EnMAP data. The algorithm adopts optimal estimation as inverse method in order to enable a rigorous quantification of uncertainties. Additionally, a validation of remotely retrieved canopy water content with field measurements is included to assess the potential of spaceborne imaging spectroscopy to support analyses of plant phenological status and health. N. Bohn developed the overall idea and approach supported by L. Guanter. N. Bohn conducted data processing and statistical analysis, generation of figures and tables, and wrote the manuscript. T. Kuester contributed to the simulation of EnMAP data, particularly, to the generation of 3D canopy reflectance simulations, and wrote the subsections about modeling

at leaf and canopy level. R. Preusker contributed to the methodological programming by providing Python scripts on optimal estimation. K. Segl contributed to the simulation of EnMAP data by providing the end-to-end software. L. Guanter contributed to data interpretation and manuscript review.

**Chapter 3 - Optimal estimation of snow and ice surface parameters from imaging spectroscopy measurements**

*Niklas Bohn, Thomas H. Painter, David R. Thompson, Nimrod Carmon, Jouni Susiluoto, Michael J. Turmon, Mark C. Helmlinger, Robert O. Green, Joseph M. Cook, Luis Guanter. Remote Sensing of Environment, 2021, 264, 112613,* https://doi.org/10.1016/j.rse.2021.112613.

The second published manuscript introduces a novel joint atmosphere and surface inversion advancing a method from Thompson et al. (2018). The study concentrates on a sensitivity analysis of snow and ice property retrievals based on synthetic EnMAP data. The algorithm adds selected surface parameters such as grain size, liquid water content, and algae concentration to the state vector in order to quantify posterior uncertainties and correlation errors. Additionally, a validation of remotely retrieved glacier algae concentration with field measurements is included to assess the potential of spaceborne imaging spectroscopy to support research of darkening and melting ice sheets. N. Bohn developed the overall idea and approach supported by D. Thompson and N. Carmon. N. Bohn conducted data processing and statistical analysis, generation of figures and tables, and wrote the manuscript. T. Painter contributed to data interpretation and manuscript review and provided simulations of directional reflectance. D. Thompson, N. Carmon, J. Susiluoto, M. Turmon, and L. Guanter contributed to data interpretation and manuscript review. M. Helmlinger effected scientific contacts and supported acquisition of AVIRIS data. R. Green provided the overall research frame by allocating both hardware and software. J. Cook contributed to data interpretation and manuscript review and provided glacier algae field measurements as well as the snow and ice radiative transfer model.

**Chapter 4 - Glacier ice surface properties in South-West Greenland Ice Sheet: first estimates from PRISMA imaging spectroscopy data**

*Niklas Bohn, Biagio Di Mauro, Roberto Colombo, David R. Thompson, Jouni Susiluoto, Nimrod Carmon, Michael J. Turmon, Luis Guanter. Journal of Geophysical Research: Biogeosciences, Special Issue "The Earth in living color: spectroscopic and thermal imaging of the Earth: NASA's Decadal Survey Surface Biology and Geology Designated Observable", submitted on November 17, 2021.*

The third manuscript presents an application of the retrieval method from Chapter 3 to measurements from the spaceborne PRISMA sensor over the Greenland Ice Sheet. The study examines the capabilities of an existing satellite imaging spectrometer to map snow and ice surface properties and provides an assessment of potential synergies between imaging spectroscopy and multiband data in a comprehensive cryosphere observation system. Additionally, a potential pathway to a global product from a virtual constellation of orbital imaging spectrometers is analyzed. N. Bohn developed the overall idea and approach supported by B. Di Mauro and R. Colombo. N. Bohn conducted data processing and statistical analysis, generation of figures and tables, and wrote the manuscript. B. Di Mauro and R. Colombo contributed to data interpretation and manuscript review and provided PRISMA data products. D. Thompson, J. Susiluoto, N. Carmon, M. Turmon, and L. Guanter contributed to data interpretation and manuscript review.

# Chapter 2

# Coupled retrieval of the three phases of water

Niklas Bohn[1], Luis Guanter[1,2], Theres Kuester[1], René Preusker[3], and Karl Segl[1].

**Publisher title:** Coupled retrieval of the three phases of water from spaceborne imaging spectroscopy measurements.
**Journal:** Remote Sensing of Environment, 242, 111708.
**Status:** Available online 28 March 2020.
**Publisher version:** https://doi.org/10.1016/j.rse.2020.111708.



[1]GFZ German Research Centre for Geosciences, Remote Sensing and Geoinformatics, Potsdam, Germany.
[2]Centro de Tecnologías Físicas, Universitat Politècnica de València, Valencia, Spain.
[3]Freie Universitaet Berlin, Department of Earth Sciences, Institute for Space Sciences, Berlin, Germany.

## Abstract

Measurements of reflected solar radiation by imaging spectrometers can quantify water in different states (solid, liquid, gas) thanks to the discriminative absorption shapes. We developed a retrieval method to quantify the amount of water in each of the three states from spaceborne imaging spectroscopy data, such as those from the German EnMAP mission. The retrieval couples atmospheric radiative transfer simulations from the MODTRAN5 radiative transfer code to a surface reflectance model based on the Beer-Lambert law. The model is inverted on a per-pixel basis using a maximum likelihood estimation formalism. Based on a unique coupling of the canopy reflectance model HySimCaR and the EnMAP end-to-end simulation tool EeteS, we performed a sensitivity analysis by comparing the retrieved values with the simulation input leading to an $R^2$ of 0.991 for water vapor and 0.965 for liquid water. Furthermore, we applied the algorithm to airborne AVIRIS-C data to demonstrate the ability to map snow/ice extent as well as to a CHRIS-PROBA dataset for which concurrent field measurements of canopy water content were available. The comparison between the retrievals and the ground measurements showed an overall $R^2$ of 0.80 for multiple crop types and a remarkable clustering in the regression analysis indicating a dependency of the retrieved water content from the physical structure of the vegetation. In addition, the algorithm is able to produce smoother and more physically-plausible water vapor maps than the ones from the band ratio approaches used for multispectral data, since biases due to background reflectance are reduced. The demonstrated potential of imaging spectroscopy to provide accurate quantitative measures of water from space will be further exploited using upcoming spaceborne imaging spectroscopy missions like PRISMA or EnMAP.


## 2.1 Introduction

Imaging spectroscopy or hyperspectral remote sensing of the Earth's system is based on spectroscopic measurements of the solar radiation reflected by atmospheric and surface components in contiguous spectral channels (Goetz et al., 1985; Vane and Goetz, 1988). They cover the visible (VIS), near-infrared (NIR) and shortwave-infrared (SWIR) part of the solar spectrum featuring a wavelength range from 400 nm to 2500 nm (Goetz et al., 1985). Since land, water and atmosphere constituents show characteristic spectral signatures, spectroscopic measurements enable their identification and quantification using physically-based retrievals by modeling atmospheric and surface absorption features. Based on this technique, imaging spectroscopy can be applied to a wide range of different scientific disciplines in

Earth Observation (EO) such as quantification of atmospheric greenhouse gases and aerosols, monitoring vegetation phenology, soil and mineral mapping, as well as retrieval of water constituents over inland water bodies, coastal areas and open ocean (Schaepman et al., 2009). Imaging spectroscopy can therefore substantially contribute to a better understanding of Earth's ecosystems and support studies of climate change (Thompson et al., 2015).

So far, research in imaging spectroscopy has been mostly based on airborne spectrometers and simulations of spaceborne technology, but a number of satellite missions were recently launched, or are to be launched soon. The German DLR Earth Sensing Imaging Spectrometer (DESIS) (Mueller et al., 2016) and the Italian Hyperspectral Precursor of the Application Mission (PRISMA) (Loizzo et al., 2018) came into operation in June, 2018 and March, 2019, respectively. The German Environmental Mapping and Analysis Program (EnMAP) (Guanter et al., 2015) is scheduled for launch in 2021 and further missions like the NASA Surface Biology and Geology (SBG) (Lee et al., 2015) and the Copernicus Hyperspectral Imaging Mission (CHIME) (Bach, Rast, and Nieke, 2018) led by ESA are in the planning phase.

The remote sensing of the three phases of water is an ideal example of the potential of imaging spectroscopy for environmental sciences, since it makes it possible to identify and quantify water in different states due to the presence of sufficient narrow bands in the NIR (Green et al., 2006). In this connection, the use of spaceborne imaging spectroscopy measurements presented in our study enables new possibilities in mapping local and global trends of water vapor, liquid water and ice. On one hand, it significantly contributes to climate research (Diedrich et al., 2013). On the other, it is essential for evaluating the water use efficiency of plants and their physiological status and health (see Clevers, Kooistra, and Schaepman (2010), Wocher et al. (2018)). Finally, it helps to assess the distribution and availability of fresh water through predicting snow melt rates and processes (Green et al., 2006).

Green et al. (2006) introduced a method to simultaneously estimate the path lengths of water vapor, liquid water and ice from airborne imaging spectroscopy data by applying a physically-based nonlinear least squares inversion of the MODTRAN Radiative Transfer Model (RTM) (Berk, Bernstein, and Robertson, 1989) linked to a surface reflectance model. The latter incorporates the Beer-Lambert law, which expresses the radiation absorption as a function of the path length of pure liquid water and ice (Born and Wolf, 1959). While water vapor can be inferred from the MODTRAN simulations, the surface reflectance model enables the retrieval of the other two phases. The approach is based on the decoupling of the overlapping absorption lines of water vapor, liquid water and ice (Green et al., 2006; Thompson

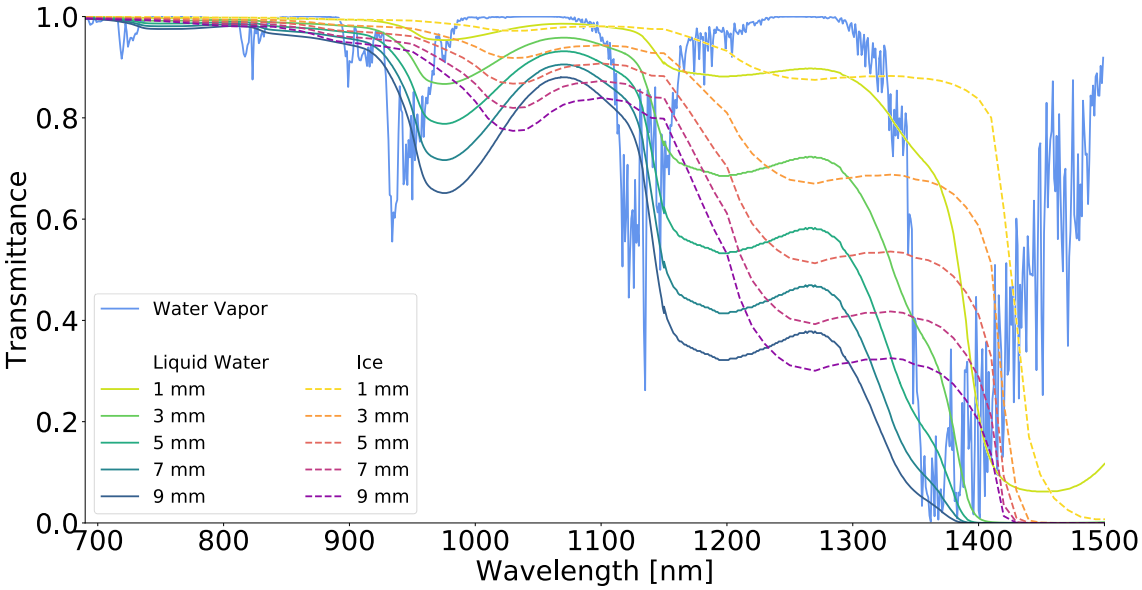


FIGURE 2.1: Overlapping transmittance spectra of the three phases of water. The line of water vapor is calculated for an absorption of 5 mm precipitable water. The lines of liquid water and ice are shown for five different absorption path lengths between 1 mm and 9 mm.

et al., 2015) (Figure 2.1). The lines of liquid water and ice are shifted towards longer wavelengths. This displacement, in combination with moderate absorption energies enables a spectroscopic separation of the three phases (Green et al., 2006). The study of Green et al. (2006) can be seen as the first assessment to infer the amounts of all three phases of water in a coupled way. Earlier studies only present combined vapor and liquid retrievals (Gao and Goetz, 1990; Green et al., 1991; Gao, 1996). Thompson et al. (2015) modified the method of Green et al. (2006) by a linear approximation of the inversion procedure, and additionally present an application on measuring cloud thermodynamic phase (Thompson et al., 2016). Each of the aforementioned retrieval studies used data from the airborne AVIRIS-C instrument (see Green et al. (1998), Vane et al. (1993)).

In view of the upcoming satellite missions, this work presents a novel application of the existing coupled retrieval of the three phases of water by extending the approach to spaceborne imaging spectroscopy measurements. We evaluate the performance of the algorithm through a sensitivity analysis based on simulated EnMAP data, which is new compared with previous applications, and show retrieval uncertainties, and discuss potential issues. Additionally, we test the algorithm on AVIRIS-C data to demonstrate the ability to map snow and ice extents, and use CHRIS-PROBA data as a proxy for future satellite measurements to illustrate the accuracy improvements using the three phases approach compared with band ratio water vapor retrievals. Finally, we focus on canopy water content (CWC) as a sort

of liquid water because of its especial relevance to vegetation studies, and show the potential of the algorithm to quantitatively map CWC from space. This is done by comparing the retrievals with ground-based measurements and by discussing the interpretation of the derived top-of-canopy (TOC) values as a function of canopy structural parameters.

## 2.2 Methods

The coupled retrieval of the three phases of water is based on the inversion of a forward model, which models the top-of-atmosphere (TOA) radiance spectra. Applying this technique, the values of columnar water vapor (CWV), liquid water and ice can be inferred by minimizing the difference between modeled and measured spectra. The minimization uses a predefined cost function in an iterative optimization procedure.

### 2.2.1 Forward model

Many algorithms in the field of remote sensing aim to infer specified quantities from a set of measurements, generally TOA radiance, by the inversion of a well-parameterized forward model. In a general form, the TOA radiance $\mathbf{y}$ is modeled by:

$$\mathbf{y} = \mathbf{F}(\mathbf{x}, \mathbf{b}) + \epsilon, \tag{2.1}$$

where $\mathbf{F}$ is the forward model, in this work composed of an atmospheric RTM and a surface reflectance model; $\mathbf{x}$ is the state vector, here containing CWV, liquid water and ice path lengths as well as slope and offset of the linear surface reflectance continuum of the chosen water absorption feature; $\mathbf{b}$ is the model parameter vector containing known parameters required by the forward model; and $\epsilon$ is an error vector containing different uncertainty components. In our case, the forward model input on one hand requires the observation geometry, i.e., the viewing zenith angle (VZA), the solar zenith angle (SZA), the relative azimuth angle (RAA) and the sensor altitude, and on the other hand, two physical parameters, namely the surface elevation (HSF) and aerosol optical thickness (AOT). $\epsilon$ consists of measurement errors caused by instrument calibration and noise, forward model errors, and errors in the state vector variables as well as the known model parameters.

#### 2.2.1.1 Atmospheric model

For the atmospheric radiative transfer simulations we use the MODTRAN code (Berk, Bernstein, and Robertson, 1989; Berk et al., 2003; Bernstein, Berk, and Sundberg,

TABLE 2.1: Gridding of LUT parameters for MODTRAN radiative transfer simulations (according to Guanter, Richter, and Kaufmann (2009)).

| | 1 | 2 | 3 | 4 | 5 | 6 | 7 |
|---|---|---|---|---|---|---|---|
| VZA (°) | 0 | 10 | 20 | 30 | 40 | - | - |
| SZA (°) | 0 | 10 | 20 | 35 | 50 | 70 | - |
| RAA (°) | 0 | 25 | 50 | 85 | 120 | 155 | 180 |
| HSF (km) | 0 | 0.7 | 2.5 | 8 | - | - | - |
| AOT | 0.05 | 0.12 | 0.2 | 0.3 | 0.4 | 0.8 | - |
| CWV ($gcm^{-2}$) | 0 | 1 | 1.5 | 2 | 2.7 | 3.5 | 5 |

2007). It is a 1D scalar RTM to calculate transmittance, radiance and fluxes for the ultraviolet (UV), VIS, NIR, SWIR and thermal infrared (TIR) spectrum covering a wavelength range of 0.2 - $10^4$ $\mu$m. We simulated wavelengths from 400 nm to 2500 nm to match the spectral coverage of EnMAP, AVIRIS-C and CHRIS-PROBA and executed MODTRAN in band model mode with a spectral sampling interval (SSI) of 1.0 $cm^{-1}$. The molecular absorption lines were obtained from the HITRAN database (Rothman et al., 2009), and multiple scattering was calculated using the DISORT N-stream (Stamnes et al., 1988).

Assuming clear sky and a plane-parallel atmosphere as well as a Lambertian surface, the TOA radiance $L_{TOA}$ can be modeled by a simplified solution of the radiative transfer equation following the approach of Chandrasekhar (1960):

$$L_{TOA} = L_0 + \frac{1}{\pi} * \frac{\rho_s(E_{dir}\mu_{sun} + E_{dif})T\uparrow}{1 - S\rho_s}, \tag{2.2}$$

where $L_0$ is the atmospheric path radiance; $\rho_s$ is the surface reflectance; $E_{dir}$ and $E_{dif}$ are the direct and diffuse solar irradiance, respectively, arriving at the surface; $\mu_{sun}$ is the cosine of the solar zenith angle; $T\uparrow$ is the total upward atmospheric transmittance; and $S$ is the spherical albedo of the atmosphere. All components except $\rho_s$ are functions of the state vector $\mathbf{x}$ and the model parameter vector $\mathbf{b}$ and are derived from the MODTRAN output by applying specific conversions following Guanter, Richter, and Kaufmann (2009). To decrease the computational burden and to increase the processing speed, the atmospheric components were previously calculated for different atmospheric cases and stored in a multidimensional Look-Up-Table (LUT) (Table 2.1). The simulations sum up to 35,380 cases and are assumed to cover most of the acquisition conditions of the data used in this study.

#### 2.2.1.2 Surface reflectance model

Since water vapor is the only water phase appearing directly within the MODTRAN code, the atmospheric RTM has to be linked with a well-parameterized surface

reflectance model to account for the path lengths of liquid water and ice. Whereas vapor is most dominant in the atmosphere, liquid and solid water can be classified as surface parameters. We use the method of Green et al. (2006) and model the surface reflectance as a linear change in reflectance with wavelength attenuated by the spectrally dependent absorption for liquid water and ice based on the Beer-Lambert law (Born and Wolf, 1959). Consequentially, the wavelength dependent surface reflectance $\rho_{s,\lambda}$ is expressed by:

$$\rho_{s,\lambda} = (a + b\lambda)e^{(-d_w\alpha_{w,\lambda} - d_i\alpha_{i,\lambda})}, \tag{2.3}$$

where $a$ and $b$ are offset and slope of the linear reflectance continuum; $\alpha_w$ and $\alpha_i$ are the wavelength dependent absorption coefficients of liquid water and ice, respectively; and $d_w$ and $d_i$ are the liquid water and ice path lengths, respectively, expressed in the same unit as wavelength. $\alpha_w$ and $\alpha_i$ are calculated by using the imaginary part of the complex index of refraction $k$, which is also wavelength dependent (Petty, 2004):

$$\alpha_\lambda = \frac{4\pi k_\lambda}{\lambda}. \tag{2.4}$$

To obtain $k$, we use the table of Kedenburg et al. (2012) for liquid water and the values from Warren (1984) for ice.

### 2.2.2 Inverse method

During the inversion of the forward model $\mathbf{F}$, water vapor, liquid water, and ice path lengths are iteratively adjusted to match modeled and measured spectra within the water absorption feature around 1140 nm. We chose the 1140 nm window since EnMAP features two overlapping detectors around the 940 nm water absorption band so that a complete coverage of the window using only one detector is not possible. Furthermore, both water bands can be used in a uniform manner to retrieve the amounts of the three phases (Thompson et al., 2015). The matching of the spectra is evaluated by a predefined cost function and the needed atmospheric parameters are obtained by a multidimensional linear interpolation within the LUT. Since we do not revert to prior or background knowledge about the uncertainties of the retrieval quantities, we apply a maximum likelihood estimation instead of optimal estimation to the iteration procedure with a focus on retrieval accuracy and processing speed. The mathematical expressions presented in the following section can be found in Rodgers (2000) as well as in applications by Diedrich et al. (2013) and Diedrich (2016).

#### 2.2.2.1 Maximum likelihood estimation

The maximum likelihood estimation enables the possibility to incorporate the error vector $\epsilon$ from Eq. 2.1 in terms of a measurement error covariance matrix $\mathbf{S}_e$ and to calculate the retrieval uncertainty for each state vector parameter as a by-product. The method is based on Bayes' theorem about probability density and takes Gaussian distribution of the errors as a basis. We invert the forward model by iteratively minimizing the cost function $f(\mathbf{x})$, which is commonly used for maximum likelihood and optimal estimation procedures:

$$f(\mathbf{x}) = (\mathbf{x} - \mathbf{x_a})^T \mathbf{S}_a^{-1} (\mathbf{x} - \mathbf{x_a}) \ + (\mathbf{y} - \mathbf{F}(\mathbf{x}))^T \mathbf{S}_e^{-1} (\mathbf{y} - \mathbf{F}(\mathbf{x})), \tag{2.5}$$

where $\mathbf{x_a}$ is the a priori state vector; and $\mathbf{S}_a$ is its error covariance matrix. Here, the difference between modeled spectra $\mathbf{F}(\mathbf{x})$ and measured spectra $\mathbf{y}$ is evaluated by taking into account the residuals between state vector and a priori state vector. Both quantities are weighted by their uncertainties and the state vector is changed at each iteration step to find the solution with the highest probability based on a given measurement and a priori information about the state. Since we apply the maximum likelihood estimation without considering information about the uncertainties of the entries of $\mathbf{x_a}$, we fill the matrix $\mathbf{S}_a$ with sufficient high values (see Section 2.2.2.2). For convergence, we use the criterion:

$$(\mathbf{x}_i - \mathbf{x}_{i+1})^T \mathbf{S}_x^{-1} (\mathbf{x}_i - \mathbf{x}_{i+1}) < \epsilon_x n, \tag{2.6}$$

where $\mathbf{S}_x$ is the a posteriori or retrieval error covariance matrix; $\epsilon_x$ is a threshold in fraction of variance (here: $\epsilon_x = 0.01$); and $n$ is the number of dimensions of the state vector. The retrieval error covariance matrix gives a direct measure of the uncertainty of each parameter and is calculated by propagating the measurement uncertainty into the state vector space:

$$\mathbf{S}_x = (\mathbf{S}_a^{-1} + \mathbf{K}_i^T \mathbf{S}_e^{-1} \mathbf{K}_i)^{-1}, \tag{2.7}$$

where $\mathbf{K}$ is the Jacobian of the forward model and expresses the change in modeled TOA radiance in the $j$-th instrument channel for a small change in the $k$-th parameter of the solution state vector $\mathbf{x}$ at iteration step $i$:

$$\mathbf{K}_{j,k} = \{\frac{\delta y_j}{\delta x_k}\}. \tag{2.8}$$

$\mathbf{S}_e$ is decomposed into a matrix $\mathbf{S}_y$ describing the uncertainties due to physical instrument noise and a matrix $\mathbf{S}_b$ accounting for errors caused by unknown forward

model parameters. $\mathbf{S}_y$ is calculated by:

$$\mathbf{S}^y_{j,k} = \{c_{j,k}\sigma_{y,j}\sigma_{y,k}\}, \tag{2.9}$$

where $\sigma_{y,j}$ is the measurement error in units of standard deviation for the $j$-th band of the imaging spectrometer; and $c_{j,k}$ is the correlation between the errors in the $j$-th and $k$-th band. For standard imaging spectrometers it can be assumed that $c_{j,k} = 0$. Consequentially, $\mathbf{S}_e$ has only diagonal elements:

$$(\delta^y_{j,j})^2 = (\frac{L_j}{SNR_j})^2 + \Delta^2_j, \tag{2.10}$$

where $L_j$ is the radiance measured in band $j$; $SNR_j$ is the signal-to-noise ratio $(y/\sigma_y)$; and $\Delta_j$ is the uncertainty of the calibration of band $j$.

We treat the uncertainties due to unknown forward model parameters as independent error sources by adding their contributions to $\mathbf{S}_y$, which is equivalent to standard error propagation:

$$\mathbf{S}_e = \mathbf{S}_y + \mathbf{K}_b\mathbf{S}_b\mathbf{K}^T_b, \tag{2.11}$$

where $\mathbf{K}_b$ is the Jacobian of the model unknowns, which expresses the change in modeled TOA radiance in the $j$-th instrument channel for a small change in the $k$-th unknown model parameter. It is expressed by:

$$\mathbf{K}^b_{j,k} = \{\frac{\delta y_j}{\delta b_k}\}. \tag{2.12}$$

$\mathbf{S}_b$ comprises uncertainties due to unknown, not retrieved parameters of the forward model. Following Thompson et al. (2018), they can be attributed to the surface, the instrument and the atmosphere. Their classification accounts for sky view effects, intrinsic error in absorption line intensities of water vapor, systematic calibration and radiative transfer uncertainty, and non-systematic radiometric uncertainty. We adopt their values for sky view effects and the water vapor absorption intensity and cover errors in liquid and solid water absorption line intensity by incorporating uncertainties of the imaginary part of the complex index of refraction $k$ presented by Kou, Labrie, and Chylek (1993). Since our sensitivity analysis is based on simulated data, we resign systematic and non-systematic errors. Table 2.2 gives an overview of the different error sources and their associated uncertainty values.

TABLE 2.2: Uncertainties due to unknown, not retrieved forward model parameters.

| Source | Elements | Value |
|---|---|---|
| Sky view factor | 1 | 10 % |
| Water vapor absorption intensity | 1 | 1 % |
| Liquid water absorption intensity | 1 | 2 % |
| Solid water absorption intensity | 1 | 2 % |

#### 2.2.2.2 A priori knowledge and first guess

We assume no mentionable correlation between the different water phases so that a priori knowledge about their uncertainties is not taken into account. Hence, the diagonal entries of the a priori covariance matrix $S_a$ are set to relatively high values. This leads to an infinitesimally small weight of the first part of Eq. 2.5, and consequentially, the cost function only evaluates the measurement uncertainty and errors in the forward model parameters.

The inversion method generally requires a first guess solution for the state vector parameters. We use the a priori state vector $\mathbf{x_a}$ as first guess and start each iteration with the result from a band ratio retrieval for CWV (after Guanter, Gomez-Chova, and Moreno (2008a)). For the a priori state of liquid water, we calculate the normalized difference water index (NDWI) (Gao, 1996) and use its relationship to the liquid water path length presented by Gao (1996) to come up with a scaled value. A similar approach is taken into account for the a priori value of the ice path length. Here, we calculate the normalized difference snow index (NDSI) (Hall, Riggs, and Salomonson, 1995) and apply the thresholds proposed by the MODIS snow products user guide to start the iteration either with 0.1 or 0 (Riggs and Hall, 2015). Additionally, the offset $a$ and slope $b$ from Eq. 2.3 have to be optimized and are initialized by approximating the surface reflectance. For this purpose, we use the TOA reflectance $\rho_{TOA}$ at both absorption feature shoulders ($\lambda_1$ and $\lambda_2$):

$$\rho_{TOA,\lambda} = \frac{\pi * L_{TOA,\lambda}}{S_{0,\lambda} * \mu_{sun}}, \tag{2.13}$$

where $S_{0,\lambda}$ is the wavelength dependent exoatmospheric solar irradiance. Now, $a$ and $b$ can be estimated by:

$$a = \rho_{TOA,\lambda_2} - \frac{(\rho_{TOA,\lambda_1} - \rho_{TOA,\lambda_2}) * \lambda_2}{\lambda_1 - \lambda_2}, \tag{2.14}$$

$$b = \frac{(\rho_{TOA,\lambda_1} - \rho_{TOA,\lambda_2})}{\lambda_1 - \lambda_2}. \tag{2.15}$$

#### 2.2.2.3 Retrieval uncertainty

The retrieval error covariance matrix $\mathbf{S}_x$ is obtained during the iteration procedure and provides information about the retrieval uncertainty and the error correlation between the retrieved state vector parameters. According to Rodgers (2000), the square root of the diagonal entries of $\mathbf{S}_x$ gives the retrieval error in the unit of the respective state vector parameter. It is equivalent to the standard deviation of the retrieved quantity. To enable an interpretation of the error correlation, we apply a normalization or rescaling leading to an error correlation matrix $\sum(i,j)$ (Govaerts et al., 2010):

$$\sum(i,j) = \frac{\mathbf{S}_x(i,j)}{\sqrt{\mathbf{S}_x(i,i) * \mathbf{S}_x(j,j)}}. \tag{2.16}$$

The equation for $\sum(i,j)$ results from the definition of the error covariance. If $\sum(i,j) \rightarrow +1$, the uncertainties of the state vector parameters are correlated, meaning an overestimation or underestimation of $i$ leads to the same for $j$. If $\sum(i,j) \rightarrow -1$, the uncertainties are anticorrelated, that is, an overestimation or underestimation of $i$ leads to the opposite for $j$. If $\sum(i,j) \rightarrow 0$, an error in the retrieval of $i$ does not effect the retrieval of $j$. The reliability of this approach including some examples can be found in Wagner, Govaerts, and Lattanzio (2010).

## 2.3 Materials

We use both simulated and measured data from imaging spectrometers for evaluating the performance of the retrieval algorithm. First, we conduct a sensitivity analysis on simulated EnMAP data since the instrument is not launched yet. The workflow of the simulation is described in the following Section 2.3.1. Subsequent, Section 2.3.2 shortly presents the characteristics and chosen datasets of both the airborne AVIRIS-C and the spaceborne CHRIS-PROBA sensors, which we additionally use to validate the retrieval.

### 2.3.1 Simulation of EnMAP spectra

For the sensitivity analysis, we used a unique coupling of the leaf reflectance model PROSPECT (Jacquemoud and Baret, 1990), the 3D canopy reflectance model Hyperspectral Simulation of Canopy Reflectance system (HySimCaR) (Kuester et al., 2014) and the sensor model EnMAP end-to-end Simulation tool (EeteS) (Segl et al., 2012) to simulate EnMAP-like TOA radiance spectra of 3D cereal canopies with known CWV and leaf water content (LWC) (Figure 2.2). The main focus is to assess the retrieval of CWC from vegetated agricultural surfaces. Therefore, we scaled

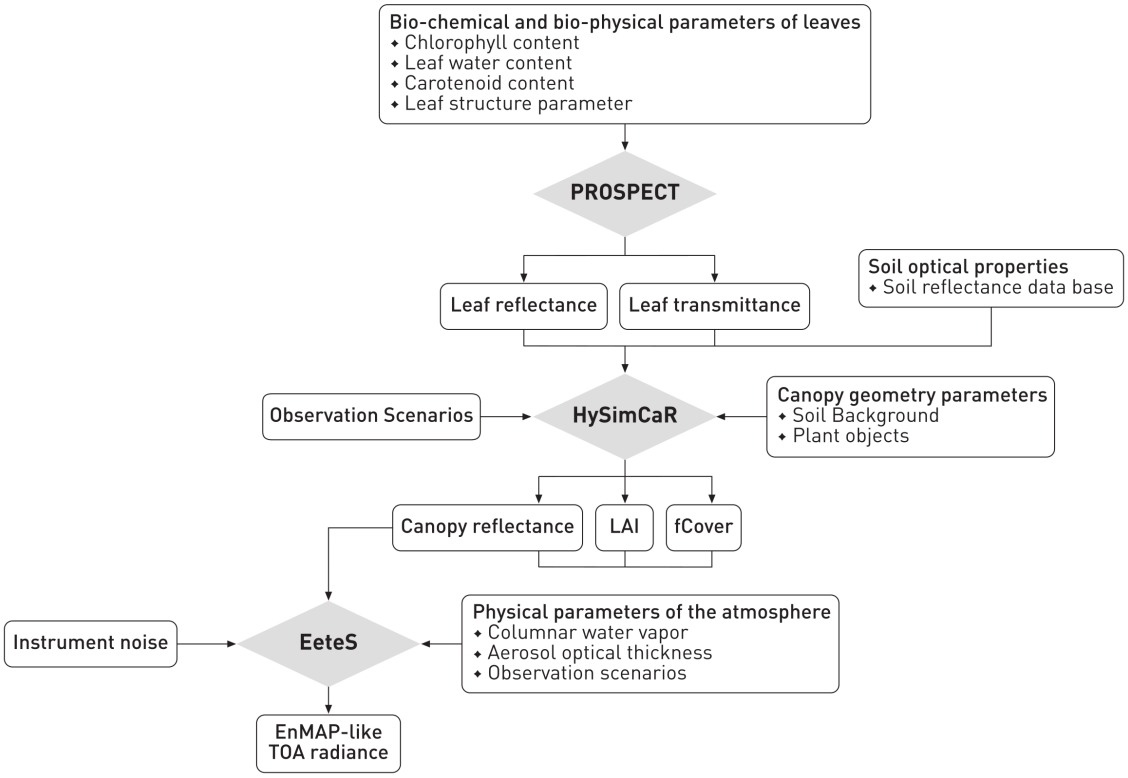


FIGURE 2.2: Structure chart of the simulation process to gain EnMAP-like vegetation canopy TOA radiance data.

up LWC to canopy level by multiplying with the leaf area index (LAI) (Clevers, Kooistra, and Schaepman, 2010), which was calculated during the HySimCaR simulations.

EnMAP is a push-broom imaging spectrometer, which is scheduled for launch in 2021 and scientifically led by the GFZ German Research Centre for Geosciences (Guanter et al., 2015). It is a high performance scientific mission leading to Level 2A products including an open data policy. EnMAP will be in sun-synchronous orbit carrying two cameras: a VIS/NIR camera covering 420-1000 nm with a mean SSI of 6.5 nm and a SWIR camera covering 900-2450 nm with a mean SSI of 10 nm. The instrument has a swath width of 30 km and a spatial sampling distance (SSD) of 30 m. The mission lifetime is scheduled for 5 years.

#### 2.3.1.1 Modeling at leaf level - PROSPECT simulations

PROSPECT is a leaf RTM, which simulates reflectance as a function of leaf bio-physical and -chemical parameters (Jacquemoud and Baret, 1990). It is coupled to canopy RTM's such as SAIL, like in PROSAIL, which also includes canopy structural elements (Jacquemoud et al., 2009), or SCOPE, which is a variation of PROSAIL

TABLE 2.3: Parameter values used for PROSPECT simulations with all possible permutations resulting in 360 simulated reflectance signatures.

| $\mathbf{C}_{ab}$ [$\mu$g/cm$^2$] | $\mathbf{C}_{ar}$ [$\mu$g/cm$^2$] | $\mathbf{C}_{brown}$ [0-1] | $\mathbf{C}_{w}$ [cm] | $\mathbf{C}_{m}$ [m$^2$/$^2$] | **N** [0-1] |
|---|---|---|---|---|---|
| 20 | 5 | 0.0 | 0.006 | 0.002 | 1.0 |
| 30 | 15 | 0.5 | 0.012 | 0.008 | |
| 40 | 25 | 1.0 | 0.018 | | |
| 50 | | | 0.024 | | |
| | | | 0.030 | | |

including photosynthesis (Tol et al., 2009). Here, we used PROSPECT to generate leaf reflectance and transmittance spectral signatures with varying leaf water content ($C_w$), chlorophyll content ($C_{ab}$), carotenoid content ($C_{ar}$), brown pigments ($C_{brown}$), dry matter content ($C_m$) and leaf mesophyll structure (N) (Table 2.3). The parameter values were varied according to experiences from several years of in-situ measurements and literature values like from Jacquemoud and Baret (1992) or Xiao et al. (2014).

#### 2.3.1.2 Modeling at canopy level - HySimCaR simulations

HySimCaR has been developed in the context of the EnMAP mission. This spectral, spatial and temporal simulation system consists of detailed virtual 3D cereal canopies for different phenological stages, whose geometries are linked to corresponding spectral information. The system enables the simulation of realistic bidirectional reflectance spectra on the basis of virtual 3D scenarios by incorporating any possible viewing position with ray tracing techniques. The sampling of the virtual 3D canopies is performed by the aDvanced Radiometric rAy Tracer (DRAT), an efficient MCRT (Monte Carlo Ray Tracing) software that was developed by Lewis (1999). DRAT calculates the canopy reflectance based on 3D descriptions with linked spectral properties, predefined camera imaging properties and illumination conditions using reverse ray tracing. The reflectance results conform to case 1 (bidirectional) of Nicodemus et al. (1977) using a planar camera model with orthographic methods and a directional illumination source. Since the third phase of RAMI (RAdiation transfer Model Intercomparison, RAMI-3 (Widlowski et al., 2007)) the DRAT model belongs to a series of credible 3D MCRT models. HySimCaR has been validated with respect to structural and spectral accuracy using three cereal types, including wheat *(Triticum aestivum)*, rye *(Secale cereale)* and barley *(Hordeum vulgare)*, and 13 different phenological stages between leaf development and senescence (after the phenological scale system of Meier (1997)). A detailed description of HySimCaR, including the entire virtual plant and canopy build up, the virtual sampling

TABLE 2.4: Parameter values used for HySimCaR simulations resulting in 72 virtual cereal canopy scenarios. (Meier, 1997)

| **Row orientation against SAA** | **Plants per meter row** | **Tillers per plant** | **Row distance** | **Phenology (Meier, 1997)** |
|---|---|---|---|---|
| 0° | 13 | 5 - 3 dev. | 13 cm - 17 cm | 24-25 late tillering |
| 30° | 15 | | 22 cm - 26 cm | 37-39 stem elongation |
| 60° | 17 | | | 41-43 late stem elongation |
| 90° | | | | |

process and its validation can be found in Kuester (2011), Kuester et al. (2014), and Spengler (2014). In addition, the model has already been used for several applications found in Kuester et al. (2017), Kuester and Spengler (2018), and Spengler et al. (2011), Spengler et al. (2013). Based on the model, the influence of plant and canopy architecture on cereal canopy reflectance, the anisotropic behaviour of cereal canopy reflectance and its inter-annual variations were investigated by Kuester and Spengler (2018). Additionally, the influence of vegetation cover on the prediction of soil spectral features was investigated and quantified by Kuester et al. (2017).

We modeled 72 structurally different virtual canopies varying in canopy phenology and architecture (see Table 2.4 for respective HySimCaR parameter values). The values of the virtual canopies were chosen to balance between natural variety, management and computational costs. Phenology, the number of plants per meter of seeding row, the number of tillers per plant and the distance between the rows are parameters determining canopy density and volume that influences the shape of the reflectance signal mainly due to leaf pigment absorption and volume scattering. The relative orientation of the seeding rows against the sun azimuth angle (SAA) influences the brightness of the whole reflectance signal due to different sunlit and shading effects. The spectral properties of the soil background were kept constant, as the focus of this study is on the vegetation parameters. As a consequence, the retrieval of liquid water content from vegetated surfaces is less violated and is assumed to report only the amounts included in the canopy. This enables a higher retrieval accuracy and a direct interpretation of the results with respect to plant conditions. Otherwise, the algorithm would likely report additional liquid water amounts in terms of soil moisture or water included in minerals. Also, overlapping absorption features of minerals could impact the liquid water retrieval. Only the 3D structure of the soil background was included to consider the typical sunlit and shading effects. LAI and fCover were calculated directly from the 3D geometry of the virtual canopies and range between 0.32 and 3.17 for LAI and between 0.18 and 0.87 for fCover. The values of both parameters are almost equally distributed. All virtual canopies were coupled with PROSPECT leaf reflectance and transmittance. This sums up to 25,920 different leaf-canopy combinations that were sampled

virtually. All resulting canopy reflectance spectra contain 467 continuous spectral bands (4 nm SSI) between 400 nm and 2448 nm with the exception of the ranges of atmospheric absorption ([1352 nm, 1416 nm] and [1824 nm, 1936 nm]).

#### 2.3.1.3 Modeling at sensor acquisition level - EeteS simulations

Based on HySimCaR model outputs, EnMAP TOA radiance spectra were simulated using EeteS (Segl et al., 2012). This tool simulates the entire image data acquisition, calibration and processing chain from spatially and spectrally oversampled data to intermediate Level-1A (systematically-corrected) raw data and to the final EnMAP products, such as Level-1B (radiometrically-corrected, spectrally- and geometrically-characterized radiance), Level-1C (orthorectified Level-1B product) and Level-2A data. Data acquisition consists of a sequential processing chain represented by four independent modules: atmospheric, spatial, spectral, and radiometric. These modules allow flexible customization of a wide range of simulation input parameters. They are coupled with a backward simulation branch consisting of calibration modules, such as non-linearity, dark current, and absolute radiometric calibration, and a series of preprocessing modules such as radiometric calibration, co-registration, orthorectification, and atmospheric correction. Since the modeled data base only consists of a collection of reflectance spectra, the simulation of the two spaceborne sensors is only performed in terms of spectral and radiometric characteristics. No spatial simulation was performed with EeteS assuming that the pixel size already is 30 m. The atmospheric simulation was performed with settings for the end of May using identical parameters for all 25,920 canopy reflectance spectra with respect to viewing geometry and physical parameters (AOT: 0.2, rural aerosol model, HSF: 0 km). Only CWV was varied between 1.9 and 2.2 $\frac{g}{cm^2}$. To calculate the measurement error covariance matrix $S_e$ within the retrieval algorithm, we obtained the EnMAP SNR from Guanter et al. (2015). EeteS provides the option to add instrument noise to the simulated TOA radiance (Figure 2.2). But since we assume no significant influences of noise effects on the three phases retrieval, we abstained from including them (see Section 2.4.1.3).

### 2.3.2 Imaging spectroscopy measurements

To extend the analysis on real data, we chose two additional datasets of imaging spectroscopy measurements for assessing the retrieval results. The first one is an airborne AVIRIS-C image acquired over a mountainous area in the Sierra Nevada, California, on 02/24/2015. The particular aim is to show the possibility of the algorithm to map snow/ice extent. We generated two subsets of the acquisition:

one containing vegetated agricultural areas and rock surfaces in equal parts covering 35.70°N - 35.76°N and 118.07°W - 118.13°W, and another consisting of partly snow- and forest-covered mountain ranges reaching from 35.57°N to 35.65°N and from 118.04°W to 118.13°W. The first subset shows a surface elevation of 400 m to 600 m for the vegetated areas and up to 1700 m for the mountainous parts. The second, more elevated region reaches up to 2300 m HSF for the highest snow-covered mountains.

AVIRIS-C has a similar wavelength range and SSI to the EnMAP sensor but varying ground sampling distance due to different flying altitudes (Green et al., 1998). It is installed on the NASA ER-2 research aircraft so that AVIRIS-C is able to acquire data from a height of up to 20 km, which results in an SSD of 20 m. The coefficients to calculate the measurement uncertainty were taken from the Python ISOFIT repository and the AVIRIS-C SNR needed for the retrieval algorithm was calculated according to Thompson et al. (2018).

To demonstrate the applicability to satellite images we also used a spaceborne CHRIS-PROBA dataset from the ESA SPARC'03 campaign in Barrax, Spain, acquired on 07/14/2003. The image covers a mixture of agricultural areas and open soil so that it is well suited for the CWC retrieval analysis. The acquisition reaches from 38.97°N to 39.13°N and from 2.00°W to 2.19°W. There are no remarkable differences in surface elevation throughout the image as the Barrax region is part of a high plateau in south-east Spain.

CHRIS-PROBA is a push-broom imaging spectrometer featuring a swath width of 13.5 km and an SSD of 36 m in the hyperspectral mode. It has a spectral range covering 410 nm to 1050 nm and an SSI of 1.25 nm (at 400 nm) and 11 nm (at 1050 nm) (Barducci et al., 2005). Barducci et al. (2005) also provided the SNR required for the retrieval algorithm. Since CHRIS-PROBA is missing channels beyond 1050 nm, we used the 940 nm water absorption feature for the retrieval.

## 2.4 Results and discussion

### 2.4.1 Retrieval from simulated EnMAP data - sensitivity analysis

#### 2.4.1.1 Water vapor

We first compare the results from the maximum likelihood estimation with the simulation input described in Section 2.3.1. We achieve a very good matching with the input values showing an $R^2$ of 0.99 and an RMSE of 0.007 $gcm^{-2}$ with an overall very slight underestimation of the CWV values (Figure 2.3a). Figure 2.3b illus-

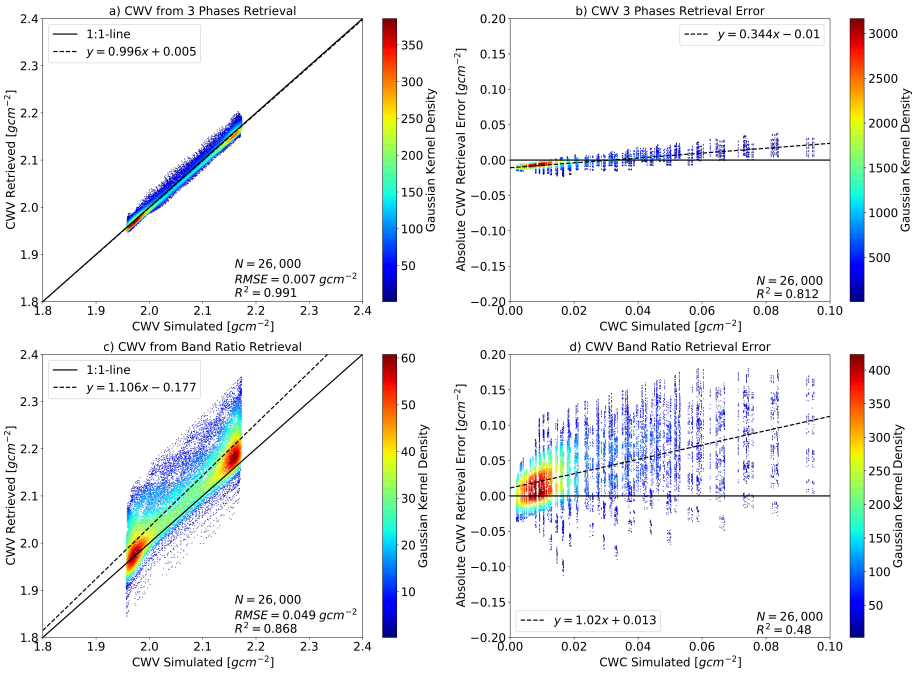


FIGURE 2.3: Comparison of derived CWV with the input of the HySimCaR + EeteS simulations. a) Results from the three phases retrieval. b) Absolute CWV retrieval error as a function of simulated CWC values for the three phases retrieval. c) Results from the band ratio retrieval. d) Absolute CWV retrieval error as a function of simulated CWC values for the band ratio retrieval.

trates the absolute CWV retrieval error as a function of simulated CWC from the three phases retrieval. For low CWC values of up to 0.02 gcm$^{-2}$, we find a negative error of around -0.01 gcm$^{-2}$ for the CWV retrieval. As it will be presented in Section 2.4.1.2, the retrieval clearly overestimates the CWC, especially for low vegetation canopy heights and small LAI. This causes the very slight underestimation of CWV for low CWC since the algorithm seems to attribute a very small fraction of CWV to nonpresent CWC. However, Figure 2.3b shows a clear linear trend of the CWV retrieval error from underestimation for low CWC values to an overestimation for higher CWC. This accords with the experience from band ratio CWV retrievals, which tend to even more overestimate CWV under the presence of high liquid water absorption (Thompson et al., 2015). To confirm this assumption, we additionally show the results from the a priori band ratio CWV retrieval (Figure 2.3c and Figure 2.3d). The values clearly more scatter around the 1:1-line with a tendency to overestimation and the absolute CWV retrieval errors are immensely higher. The retrieval is slightly biased due to the a priori state which is based on the overestimated CWV values. As a consequence, a very small overestimation of CWV for higher simulated CWC still occurs (Figure 2.3b). However, our results accord with the outcomes of previous studies that estimating CWV and liquid water amounts in a simultaneous way improves the accuracy of atmospheric correction procedures

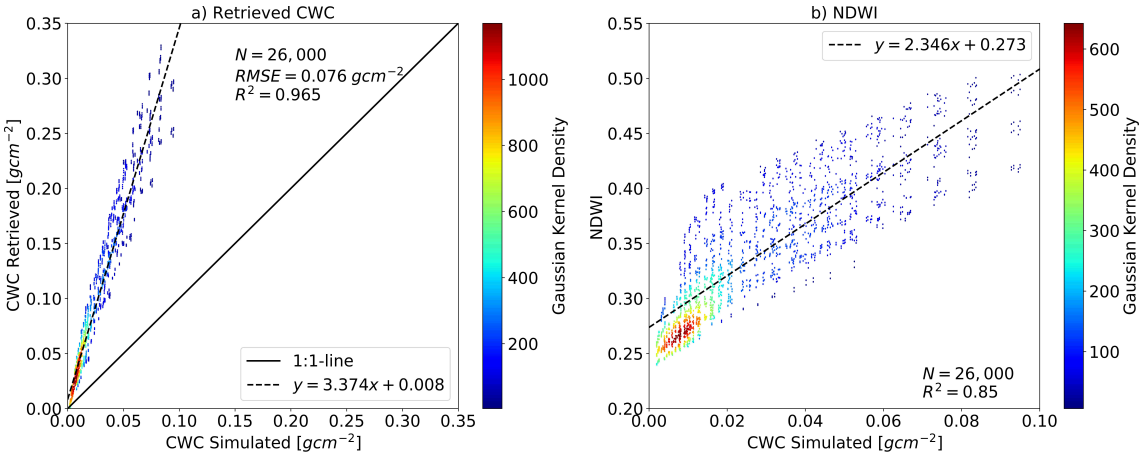


FIGURE 2.4: Comparison of derived CWC from the three phases retrieval with a) the input of the HySimCaR + EeteS simulations and b) the previously calculated NDWI, which has been used to build the a priori state of liquid water.

since biases due to background reflectance are reduced (Gao and Goetz, 1995; Green et al., 1991; Thompson et al., 2015).

#### 2.4.1.2 Canopy water content

In the same way as for CWV, we compare retrieved CWC with the simulation input. Again, a very good correlation between retrieved and simulated values can be observed depicting an $R^2$ of 0.96 (Figure 2.4a). Though, the result shows a constant mean overestimation with a slope of approximately 3.37 and virtually no offset. This induces the relatively high RMSE of 0.07 $gcm^{-2}$. Nearly the same behavior was found by Wocher et al. (2018), whose CWC retrieval from TOC spectra is likewise based on the Beer-Lambert law too, but with a constant overestimation of around 3.52. They calibrated their retrieval model with simulated PROSPECT spectra and tested the approach on ASD measured in situ data and HyMAP images. This overestimation is due to volume scattering processes within the vegetation canopies, which the Beer-Lambert law cannot take into account (Zhang, Li, and Zhang, 2011). Although Wocher et al. (2018) received accurate results, it has to be mentioned that both, their study and our simulations of EnMAP data, are based on spectra of more or less uniform canopies of low-lying cereal crops between tillering and late stem elongation and therefore, higher uncertainties might be assumed by applying such model calibration factors to more complex canopies and/or different observing conditions. Especially different observation geometries, such as those planned for EnMAP (off-nadir observations up to ±30° (Guanter et al., 2015)) lead to an increase of the uncertainties. Asner and Martin (2008) showed that LAI and viewing geometry most negatively impact the accuracy of the spectroscopic retrieval

of especially CWC. The difficulty to transfer between different observation geometries largely stems from changing fractions of sunlit or shaded vegetation (opaque or translucent) or soil. Depending on the viewing angle, the sensor observes a different composition of the reflecting surfaces due to the path of radiation through the vegetation canopy. For this, more investigations would have to be made in order to be able to evaluate the transferability of the method to different observation geometries. Kuester and Spengler (2018) have analyzed the spectral influences of different canopy architecture and observation geometries on cereal canopy reflectance and found that the larger the fraction of the radiation reflected by the vegetation canopy, the stronger is the influence of the canopy architecture on the reflectance signal. A finding that can very likely also be assumed for other vegetation canopies such as pastures or shrublands. A detailed discussion of the influence of crop canopy architecture on the CWC three phases retrieval of arable lands and a test investigating possible modifications of the Beer-Lambert law are provided in Section 2.4.4.

However, Figure 2.4b gives an impression of the advantages of imaging spectroscopy with respect to multispectral instruments. The correlation between retrieved CWC and NDWI is clearly lower with an $R^2$ of 0.85 showing a stronger scattering around the regression line. Consequentially, we assume that the three phases approach can better capture changes in CWC than multispectral indices are able to and thus, offers a high potential for accurate vegetation analysis.

#### 2.4.1.3 Surface reflectance

We additionally used the CWV and CWC retrieval results to calculate atmospherically corrected surface reflectance spectra. This enables a quantitative comparison with the input canopy reflectance spectra simulated by HySimCaR. We evaluate the wavelength range around the used water absorption feature at 1140 nm (Figure 2.5). Very good results can be observed for both the modeled TOA radiance and the surface reflectance. The residual errors range within 0.5 % for low CWC and within 1 % for high CWC, which makes the results similar to those obtained by Thompson et al. (2015).

We achieved the results based on noise free simulated TOA radiance spectra. Adding instrument noise to the simulations leads only to a marginal decrease of retrieval accuracy. Figure 2.6 shows the norm of the mean residual errors of all simulated spectra for both the modeled TOA radiance and the retrieved surface reflectance. Again, we evaluate the absorption feature around 1140 nm separated in results for spectra containing either low or high CWC. The dashed lines represent simulations with additional instrument noise while the solid lines illustrate the

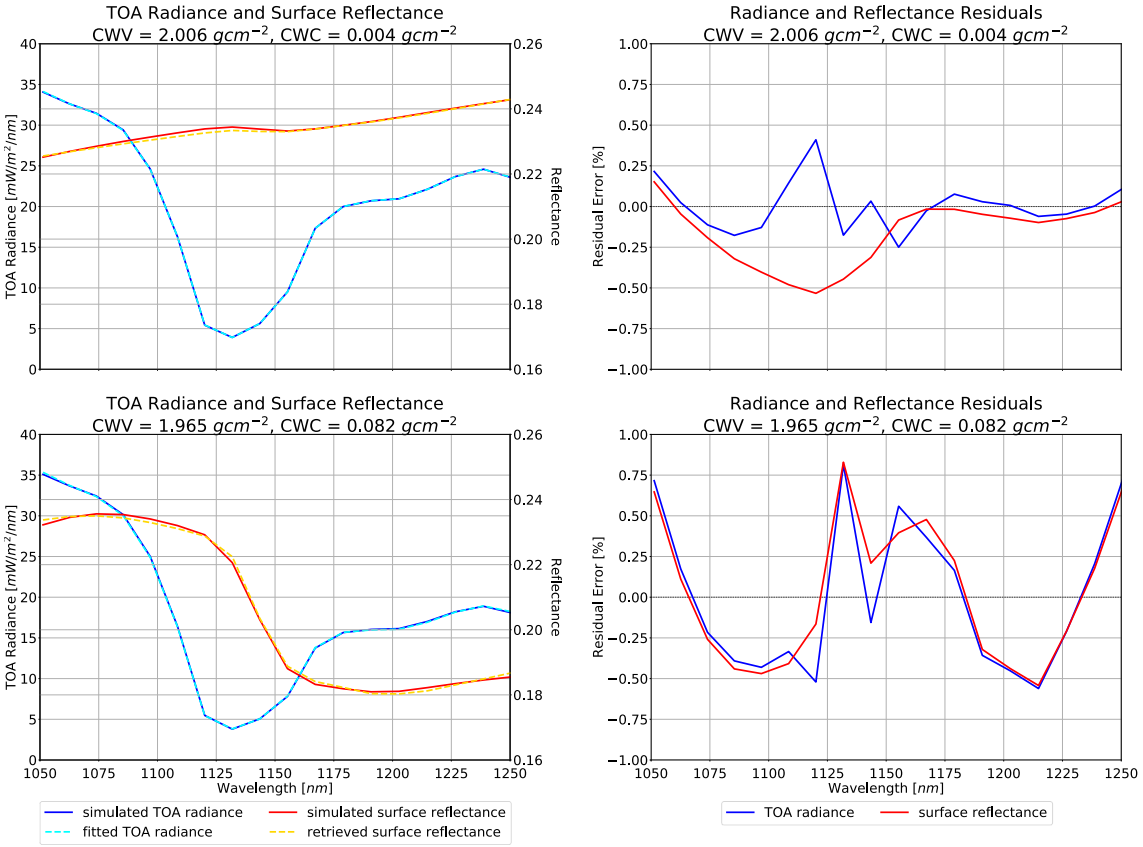


FIGURE 2.5: Results for the TOA radiance spectral fit and the surface reflectance retrieval from simulated EnMAP data for the water absorption feature at 1140 nm. Left panel: simulated and fitted TOA radiance as well as simulated and retrieved surface reflectance. Right panel: relative residual errors for both quantities. Upper panel: low CWC amount. Lower panel: high CWC amount.

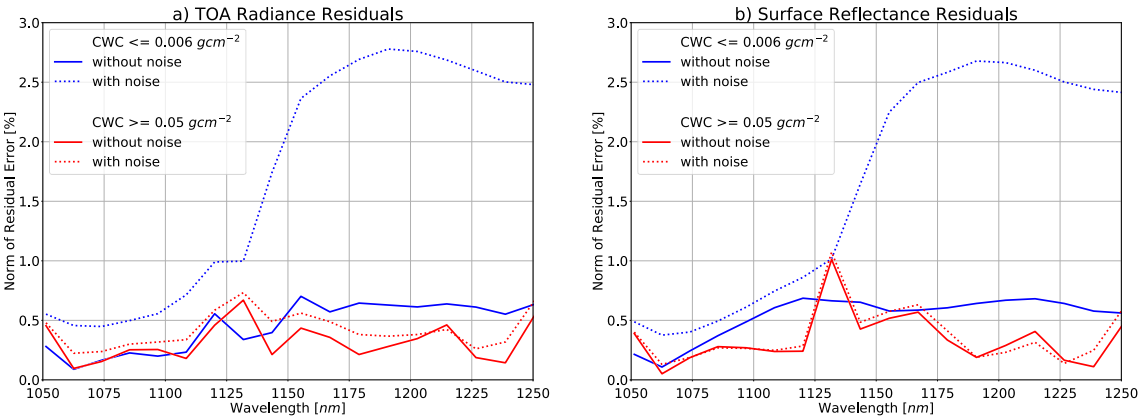


FIGURE 2.6: Norm of the mean residual errors of all simulated spectra for a) the modeled TOA radiance and b) the retrieved surface reflectance. Blue lines represent low CWC $<= 0.006 gcm^{-2}$, red lines illustrate high CWC $>= 0.05 gcm^{-2}$. Dashed lines represent simulations with additional instrument noise, solid lines illustrate simulations without noise used for the sensitivity analysis.

TABLE 2.5: Regression coefficients and correlation metrics for retrieved CWV and CWC for simulations including instrument noise and for noise free simulations used for the sensitivity analysis.

| | Slope | Offset | $R^2$ | RMSE |
|---|---|---|---|---|
| CWV | 0.9969 | 0.0053 | 0.9919 | 0.0077 |
| CWV (noise) | 0.9828 | 0.0348 | 0.9869 | 0.0095 |
| CWC | 3.3746 | 0.0082 | 0.9650 | 0.0767 |
| CWC (noise) | 3.4583 | 0.0044 | 0.9328 | 0.0784 |

simulations without noise used for our sensitivity analysis. Both modeled TOA radiance and retrieved surface reflectance show a similar behavior when noise is added to the simulations. For low CWC the residual errors increase by a factor of 2 to 4, whereas for high CWC the errors are only marginally higher. Especially the surface reflectance retrieval seems to be nearly unaffected by instrument noise under the presence of high CWC. Furthermore, the retrieval accuracy of CWV and CWC only slightly decreases when noise is added to the simulations (Table 2.5). The $R^2$ still shows values of 0.98 for CWV and 0.93 for CWC, respectively, indicating a very good correlation. Although the RMSE for CWV rises of about 23 %, the absolute retrieval error still is below 0.5 % of the mean retrieved CWV. The RMSE for CWC even rises about only 2 % under the influence of instrument noise. These results justify our previous assumption not to add instrument noise to the simulations.

#### 2.4.1.4 Correlation errors

Based on Eq. 2.16 we calculated the correlation error matrix for the synthetic EnMAP dataset. Figure 2.7 shows the correlation of the retrieval errors between the state vector parameters, which are all optimized during the iteration procedure. Errors in the estimation of slope and offset of the linear reflectance continuum clearly influence the CWC retrieval featuring coefficients of 0.93 and -0.92, respectively. Otherwise, the CWV retrieval seems to be nearly uncorrelated with the CWC derivation. This justifies the use of the maximum likelihood approach instead of the optimal estimation method at least for the CWV and CWC retrieval. However, the correlation coefficients for offset and slope indicate that a priori information about both quantities is needed to increase the accuracy of the retrieval. In general, if a priori uncertainties are known and free of biases, adding a priori knowledge, that is, applying optimal estimation, can significantly improve the retrieval results (Rodgers, 2000).

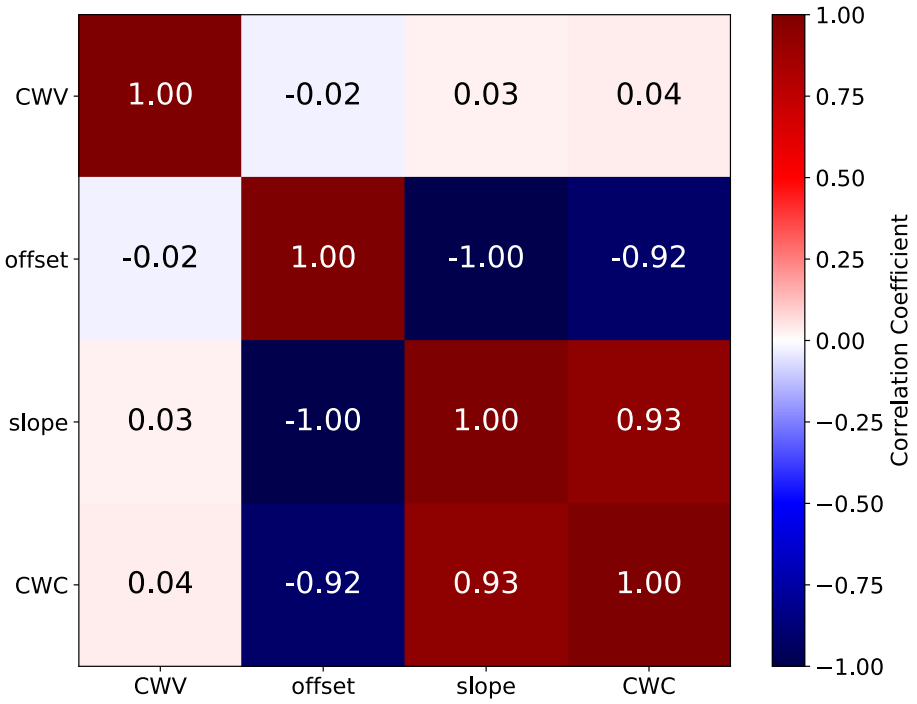


FIGURE 2.7: State vector correlation error matrix for the three phases retrieval from the simulated EnMAP data.

### 2.4.2 Retrieval from AVIRIS-C data

Figure 2.8b-c shows the retrieved CWV and CWC maps for the AVIRIS-C Sierra Nevada vegetation subset. As previously shown in Green et al. (2006), the distribution of the CWV values obviously matches the texture of the surface elevation in an anticorrelated way and CWC is clearly higher for vegetated areas compared with rock surfaces (also see Thompson et al. (2015)). The derived CWV ranges from 0.78 $gcm^{-2}$ and less for the highest elevations of up to 1700 m and 0.90 $gcm^{-2}$ and more for lower elevated areas of around 500 m. This is plausible when comparing with AERONET data. The nearest station at a distance of approx. 250 km in Fresno, CA (36.8°N, 119.8°W, 100 m surface elevation) shows a mean CWV of 0.91 $gcm^{-2}$ and a maximum value of 0.98 $gcm^{-2}$ for February 24, 2015 (AERONET, 2019). The retrieved CWC of 0-0.2 $gcm^{-2}$ is also meaningful when comparing to the results from the sensitivity analysis (Section 2.4.1.2).

We additionally produced uncertainty maps from the a posteriori covariance matrix showing the retrieval errors for CWV and CWC (Figure 2.8d-e). Overall, CWV shows lower errors than CWC due to less variance within the retrieved values, which was also shown by the sensitivity analysis on simulated data. Furthermore, the type of surface has not that much influence on the amount of vapor in the atmosphere. This influence can be seen in the CWC uncertainty map yielding the highest retrieval errors over dark surfaces, e.g., the shady sides of the mountains,

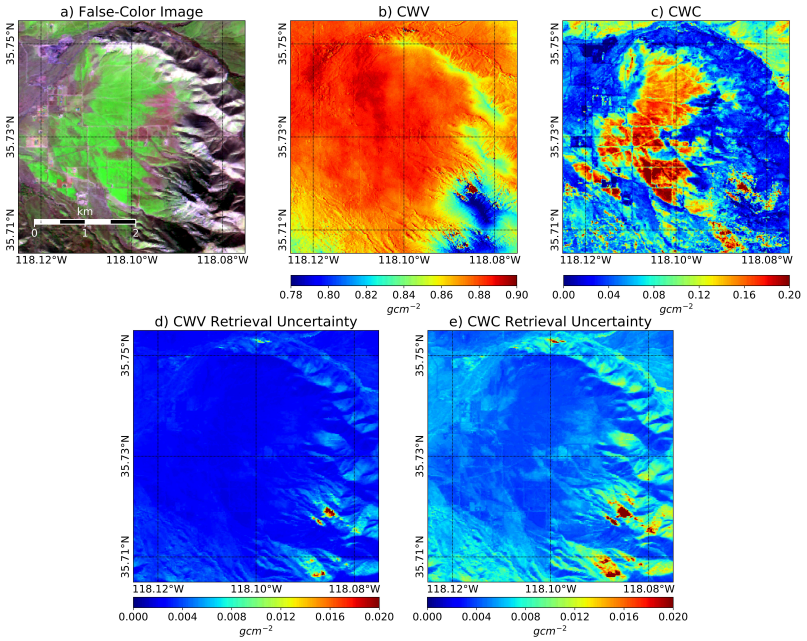


FIGURE 2.8: Results for the three phases retrieval from the AVIRIS-C Sierra Nevada vegetation subset, supplemented by the uncertainty maps from the a posteriori covariance matrix. a) False-color image (RGB: 1602/870/560 nm). b) CWV map. c) CWC map. d) CWV uncertainties. e) CWC uncertainties. The pixel values of the uncertainty maps represent the standard deviation in the unit of the retrieved parameter.

since the CWC estimation depends on the signal strength of the surface reflection. Also, a general issue of RTMs is that they are not able to realistically simulate shaded areas.

For a continuative evaluation, we compared the retrieved CWC with the NDWI, which has been previously calculated to build the a priori state of liquid water (see Section 2.2.2.2) (Figure 2.9). We achieve an $R^2$ of 0.71, which indicates a good correlation between derived CWC and NDWI and confirms the plausibility of the three phases retrieval result.

Although the solid water phase was not considered for the sensitivity analysis, we included an appropriate dataset to apply the algorithm on snow-covered surfaces. Figure 2.10b-d shows the retrieved maps for the three water phases for the AVIRIS-C snow/ice subset. To improve the interpretation of spatial trends of the three phases, we produced a combined RGB map (Figure 2.10e). CWV, CWC and ice are displayed in red, green, and blue, respectively. Consequentially, turquoise colors depict melting snow since both ice and liquid water are present. Again, the CWV values anticorrelate with surface elevation and the value range of CWV (0.72-0.88 $gcm^{-2}$) likewise fits well to the AERONET observations at Fresno mentioned before (AERONET, 2019). The derived CWC of up to 0.4 $gcm^{-2}$ increases for surfaces covered by wet snow and accords with typical value ranges for liquid water

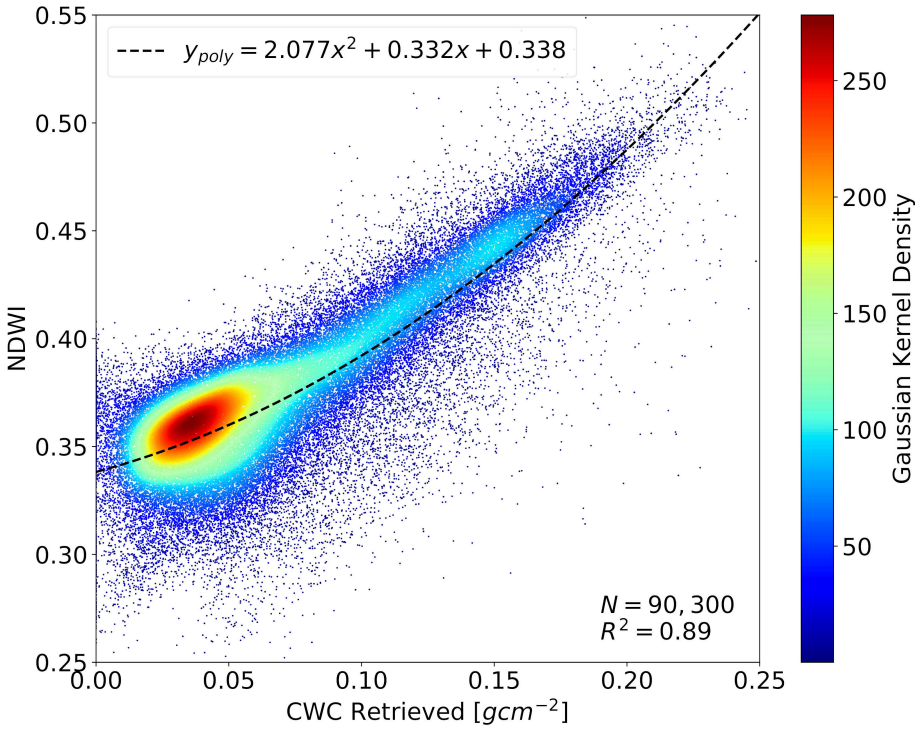


FIGURE 2.9: Comparison of NDWI with retrieved CWC from the AVIRIS-C Sierra Nevada vegetation subset.

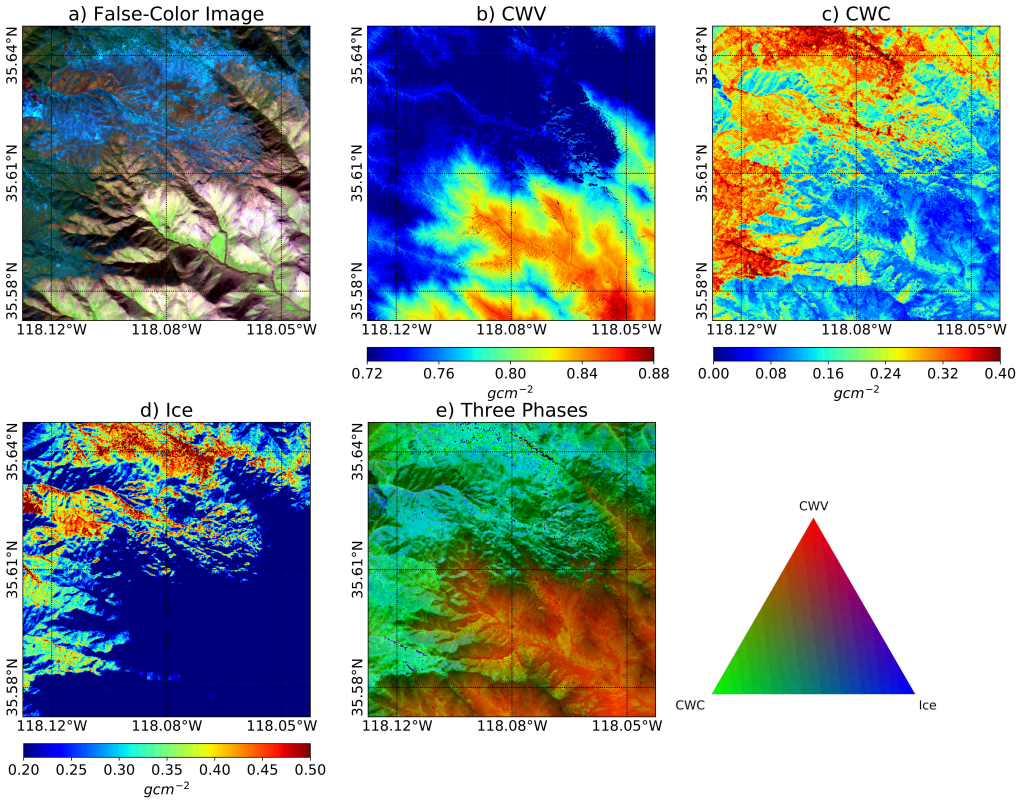


FIGURE 2.10: Results for the three phases retrieval from the AVIRIS-C Sierra Nevada snow/ice subset. a) False-color image (RGB: 1602/870/560 nm). b) CWV map. c) CWC map. d) Ice map. e) Combined three phases map (RGB: CWV/CWC/Ice).

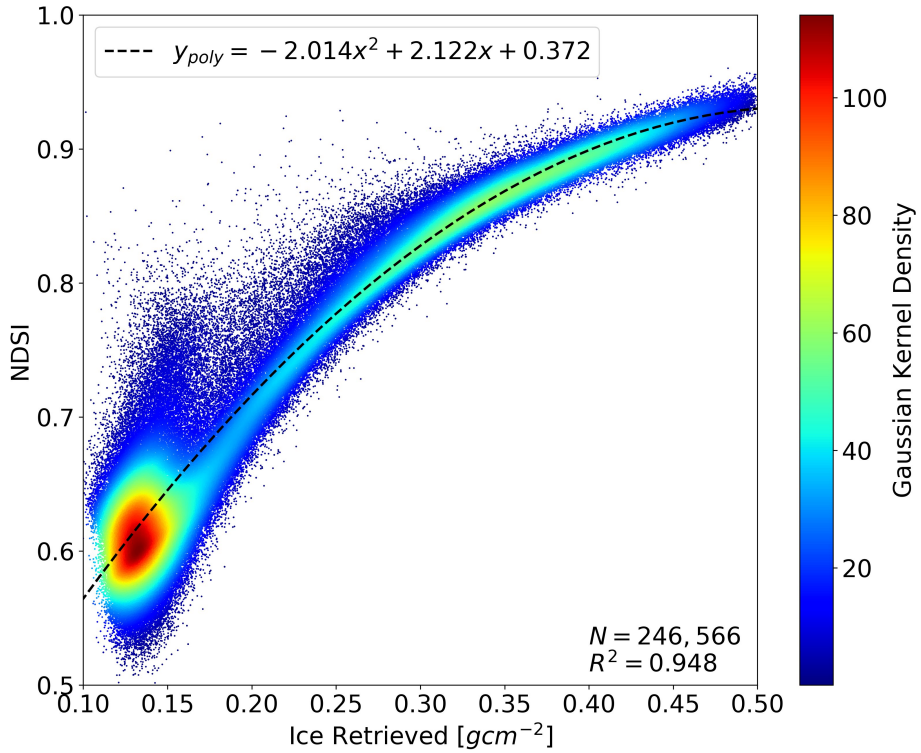


FIGURE 2.11: Comparison of NDSI with retrieved ice path lengths from the AVIRIS-C Sierra Nevada snow/ice subset.

observed by Green et al. (2006). The distribution of snow and ice-covered areas corresponds well with the false-color image and the results with many pixels showing around 0.5 $gcm^{-2}$ or enormously more are in a good compliance with typical values for dry and wet snow presented by Green et al. (2006).

We also compare the derived ice amounts with the NDSI, which results in a very good correlation with an $R^2$ of 0.94 (Figure 2.11). The fitted polynomial regression indicates that the three phases retrieval is able to better distinguish between medium and high ice amounts compared to the NDSI, which becomes saturated at a value of around 0.9.

### 2.4.3 Retrieval from CHRIS-PROBA data

Figure 2.12b-d shows the retrieval results for the CHRIS-PROBA Barrax dataset incorporating the CWV and CWC maps from the three phases retrieval. The true-color image is supplemented by the indicators of ground-truth data conducted during the ESA SPARC'03 campaign, which amongst others contain CWC measurements. Additionally, we present a CWV map derived from the a priori band ratio retrieval (see Section 2.2.2.2). As likewise shown in Thompson et al. (2015), the CWV map

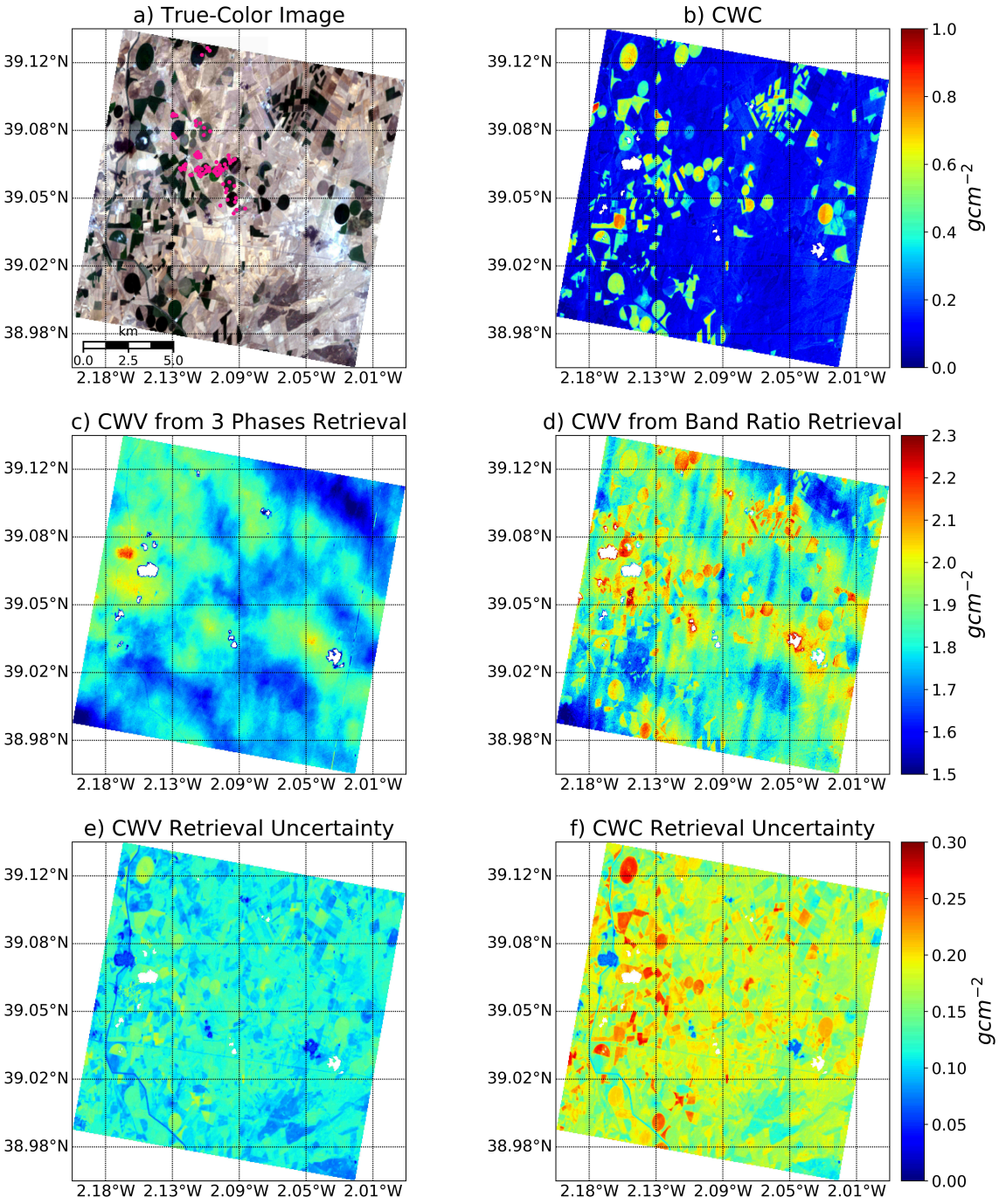


FIGURE 2.12: Retrieval results from the CHRIS-PROBA Barrax dataset, supplemented by the uncertainty maps from the a posteriori covariance matrix. a) True-color image with pink colored points representing locations of field measurements (RGB: 653/563/481 nm). b) CWC map derived from the three phases retrieval. c) CWV map derived from the three phases retrieval. d) CWV map derived from the a priori band ratio retrieval. e) CWV uncertainties. f) CWC uncertainties. White colored pixels indicate masked clouds, which have been excluded from the retrievals. Except for the upper panel, each colorbar accounts for both left and right panel. The pixel values of the uncertainty maps represent the standard deviation in the unit of the retrieved parameter.

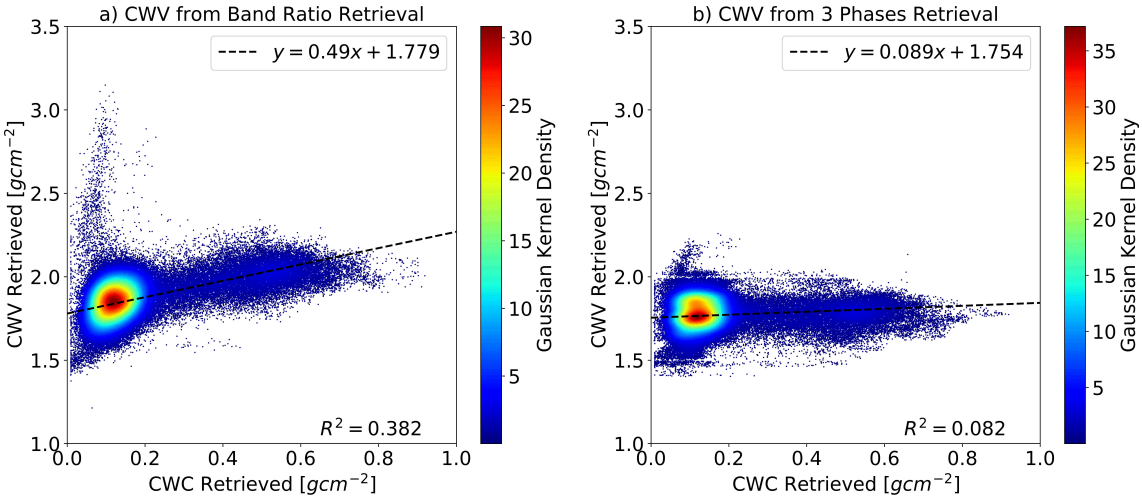


FIGURE 2.13: Comparison of retrieved CWV with retrieved CWC for different retrieval methods. a) Band ratio retrieval. b) Three phases retrieval.

from the three phases retrieval is much smoother and physically-plausible. In contrast, the CWV map from the band ratio approach has clear biases in form of textures according with vegetated areas indicating a higher sensitivity to background reflectance. Also low-frequency striping patterns are visible, which have been previously observed by Guanter et al. (2008b). The result from the algorithm presented in our study is nearly free of these influences. Cloud pixels have been excluded from the retrieval and areas of cloud shadow have to be treated carefully within the analysis since retrieved CWV generally shows a strong positive bias for these pixels (Barducci et al., 2004).

As one major result, the three phases retrieval leads to a decoupling of retrieved CWV from apparent CWC. Already recognizable in the maps of Figure 2.12, the influence of present surface liquid water on the CWV retrieval declines compared with the band ratio retrieval. This is underlined by both the decreasing slope and $R^2$ from 0.49 to 0.08 and from 0.38 to 0.08, respectively, when comparing retrieved CWV with retrieved CWC for the different methods (Figure 2.13). This trend was also observed by Thompson et al. (2015).

The derived CWC map provides a clear distinction of agricultural areas and bare soil as pixels with high water content can be distinguished well from the surroundings. Furthermore, the validation with the CWC field measurements yields a good correlation resulting in an $R^2$ of 0.8 (Figure 2.14). The overestimation of CWC by the Beer-Lambert model is clearly visible and varies depending on the crop type, which results in a remarkable forming of clusters. For example, the measured CWC of garlic and alfalfa is in a similar range, but the retrieval overestimates most of the alfalfa CWC by a factor of 2 to 3. The clusters indicate the different crop type architectures and penetration depths and thus, the varying ability to

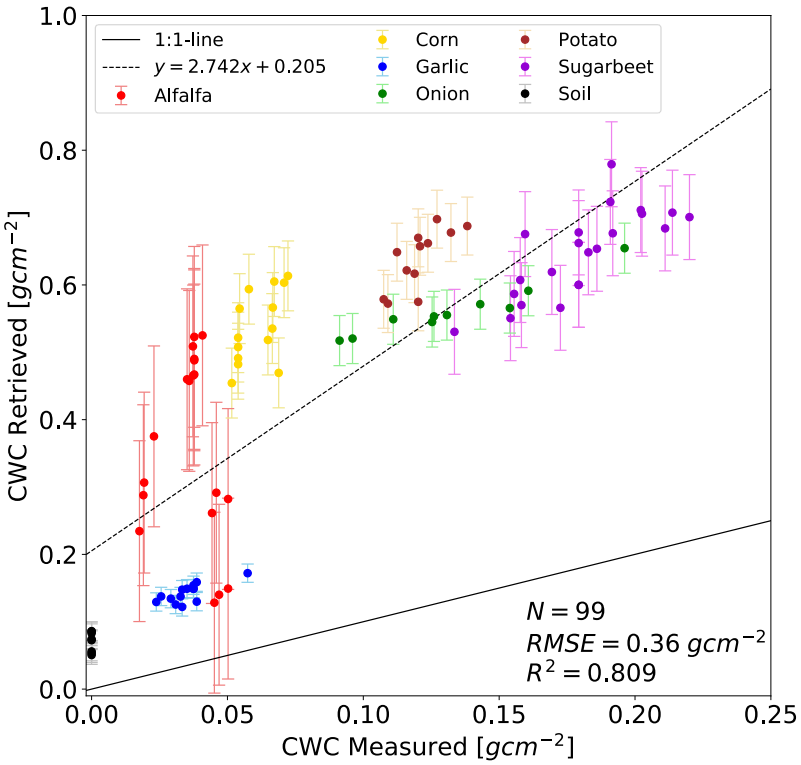


FIGURE 2.14: Comparison of retrieved CWC with measured CWC from the Barrax SPARC'03 field campaign. Error bars indicate the standard deviation of retrieved CWC.

detect CWC. Pasqualotto et al. (2018) recently developed two new hyperspectral indices to retrieve CWC: the water absorption area index (WAAI) and the depth water index (DWI). They also used the dataset of field measurements from the ESA SPARC'03 campaign in Barrax, Spain, acquired on 07/14/2003, but in combination with atmospherically corrected airborne HyMap data. They achieved an $R^2$ of 0.8 for the WAAI and 0.7 for the DWI. Hence, the result from the three phases retrieval ranges in the same order of magnitude and even outperforms one of the proposed hyperspectral indices.

Another substantial fact is that the algorithm is able to meaningfully map CWV and CWC without having the right shoulder of the 940 nm water absorption feature at its disposal since CHRIS-PROBA is missing channels beyond 1050 nm. However, these missing bands can lead to higher retrieval uncertainties when looking at the validation of absolute values. This is also expressed by the uncertainty maps from the a posteriori matrix, which show much higher uncertainties for both CWV and CWC than for the AVIRIS data. Especially, a strong correlation between retrieved CWC and retrieval error is observable (Figure 2.12e-f). Another error source within the CWV retrieval are the miscalibration trends of CHRIS-PROBA in the NIR wavelength range. This issue was reported by Guanter, Alonso, and Moreno (2005) who stated that the resulting underestimation of the signal cannot be used for

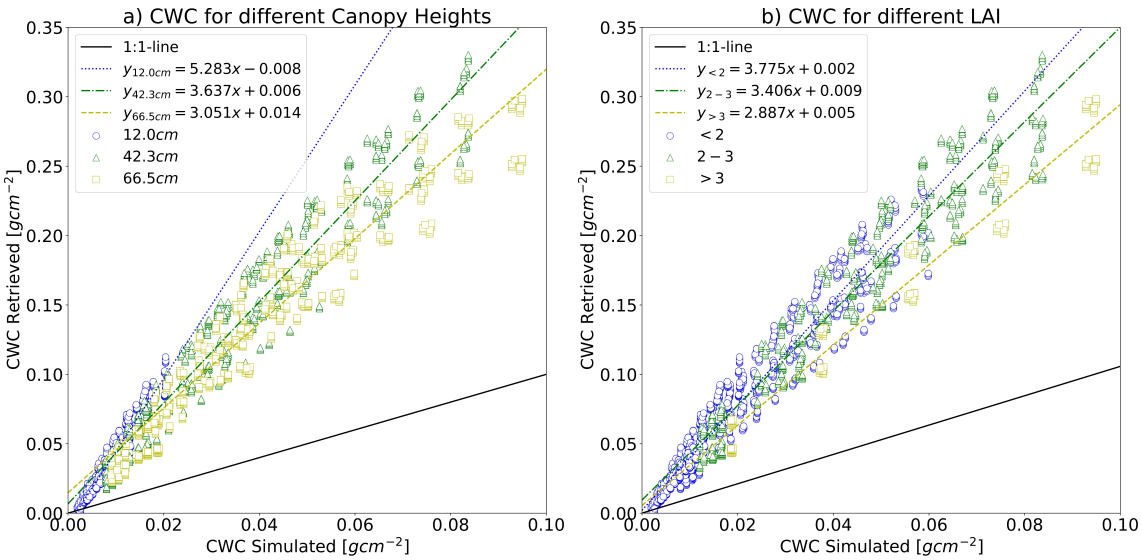


FIGURE 2.15: Comparison of retrieved CWC with simulated CWC as a function of a) mean canopy height, and b) LAI, from the simulated EnMAP data.

common radiative transfer algorithms, which instead have to be supplemented by empirical line approaches to obtain useful results.

### 2.4.4 Interpretation of CWC retrieval results

Wocher et al. (2018) used the regression slope for calibrating their CWC retrieval results, but our study indicates that this factor cannot be seen as a global calibration. As shown in Figure 2.14, the overestimation varies depending on the vegetation type and the according characteristics. We further investigate this with some analysis on the simulated EnMAP data. As a result, a critical factor influencing the overestimation is the vegetation canopy height (Figure 2.15a). Increasing the height of simulated cereal plants from 12 cm to 66.5 cm leads to a decrease in regression slope from 5.28 to 3.05. Furthermore, the overestimation decreases from 3.77 to 2.88 for increasing LAI from less than 2 to more than 3 (Figure 2.15b). On one hand, the overestimation can be attributed to volume scattering processes within the canopy, which the Beer-Lambert law is not able to account for (Zhang, Li, and Zhang, 2011). These are very special effects in vegetation canopies due to the multitude of scattering objects, e.g., leaves, and their ability to transmit radiation (Kuester and Spengler, 2018). On the other hand, it can be stated that the higher the modeled canopies and the LAI are, the better is the accuracy of retrieved CWC. Roberts et al. (1998a) showed that LAI and vegetation canopy liquid water amounts are well correlated. Consequentially, we assume that with increasing LAI the volume scattering effect indeed gets stronger, but since the liquid water contents simultaneously increase, the additional amounts retrieved by the Beer-Lambert law

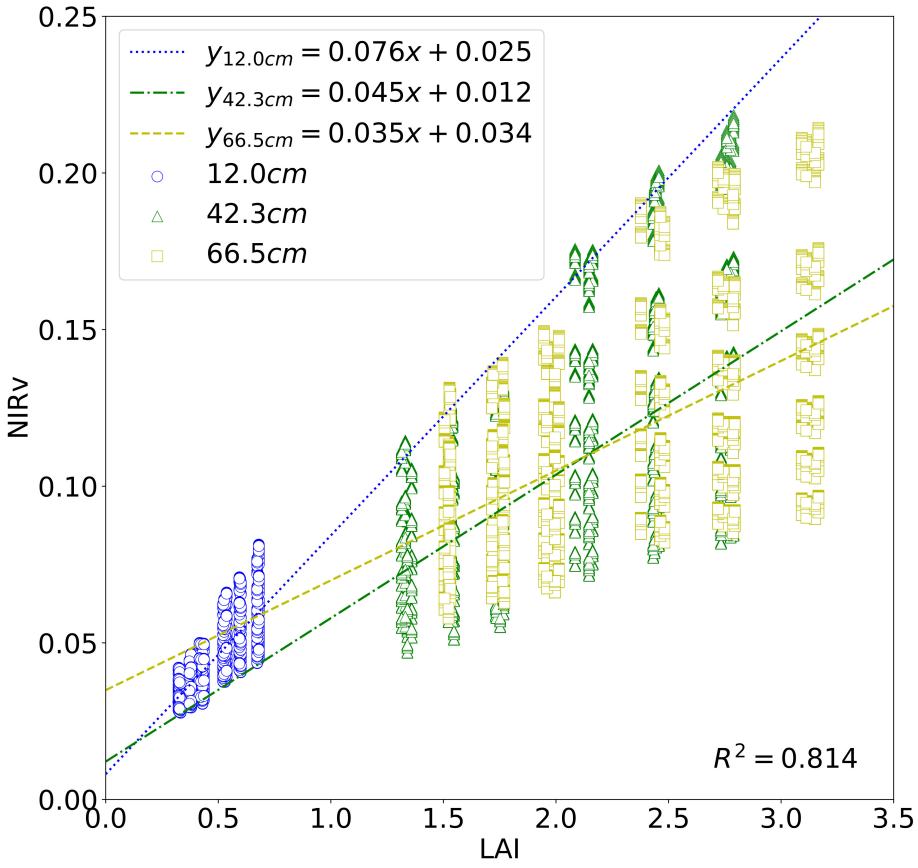


FIGURE 2.16: Comparison of NIRv with LAI for different mean canopy heights.

get smaller compared to the actual CWC and lead to a higher retrieval accuracy. This fits to the findings of Wocher et al. (2018) who got best results in the early young growth stages when most of the scattering objects in the canopy are leaves. In general, the more opaque stalks and ears are present in the canopy, the lower is the retrieval accuracy.

We added a test of NIR reflectance as an indicator of volume scattering by calculating the NIR reflectance of vegetation (NIRv) for each spectrum. This index was presented by Badgley, Field, and Berry (2017) and is related to photon escape probability, i.e., NIR reflectance, and corrects for the non-green parts of the pixel:

$$NIRv = (NDVI - 0.08) * \rho_{TOA,\lambda_{NIR}}. \tag{2.17}$$

It is calculated as the product of normalized difference vegetation index (NDVI) and NIR TOA reflectance $\rho_{TOA,\lambda_{NIR}}$ at $\lambda_{NIR} \sim 780\ nm$. Badgley, Field, and Berry (2017) proposed to substract 0.08 from the NDVI values to account for bare soil. Figure 2.16 shows the NIRv compared with LAI for different canopy heights. The NIR reflectance is well correlated with LAI yielding an $R^2$ of 0.81 and clearly increases for higher LAI. The canopy height seems to have less effect on the NIRv.

Only for very small vegetation the NIR reflectance is substantially lower. Concluding, we assume that the volume scattering effects are mainly correlated with LAI and not necessarily with canopy height. Thus, a future approach will be to supplement the surface reflectance model based on the Beer-Lambert law with information about the LAI and the NIR reflectance to correct for canopy structural effects. Finally, also soil moisture content and water included in surface minerals have to be considered. Both can influence the retrieved liquid water path over bare soil since the Beer-Lambert law is not able to distinguish between water included in different kinds of surface. An illustration can be found in Figure 2.14 where bare soil pixels with a measured CWC of 0 $gcm^{-2}$ show retrieved values of 0.05-0.08 $gcm^{-2}$.

Hunt, Ustin, and Riano (2013) proposed not to use the absolute CWC values retrieved by the surface model based on the Beer-Lambert for further analyses. They pointed to alternative retrieval methods, which are insensitive to volume scattering effects, e.g., partial least squares regression (Asner and Martin, 2008; Li et al., 2008) or wavelet transforms (Cheng, Rivard, and Sanchez-Azofeifa, 2011). However, our study shows that the Beer-Lambert surface reflectance model indeed can be improved with additional terms, but nevertheless, leads to promising results, which are already interpretable regarding absolute retrieved CWC.

## 2.5 Conclusion

We present a coupled retrieval of the three phases of water applied to spaceborne imaging spectroscopy measurements such as the upcoming German EnMAP mission. We analyze the sensitivity of the algorithm by a novel combination of field validation using CHRIS-PROBA measurements and a simulation study based on synthetic EnMAP data. The latter are obtained from canopy reflectance spectra simulated by the 3-dimensional HySimCaR system. Previous studies mainly validated their results by a visual interpretation (see Green et al. (2006), Thompson et al. (2015)) or used 1-dimensional PROSAIL spectra as input without simulating the atmosphere (see Clevers, Kooistra, and Schaepman (2010), Wocher et al. (2018)). Focusing on canopies of cereal crops, our sensitivity analysis demonstrates the ability of the proposed three phases of water retrieval to infer CWV and CWC with a high correlation to the simulation input showing an $R^2$ of 0.99 and 0.96, respectively.

However, our investigation shows that CWC is strongly overestimated by a mean factor of 3.37, which results from a large dependency on canopy structure and crop type. From a physical perspective, volume scattering effects related to LAI are primarily responsible for the observed overestimation. Otherwise, increasing the LAI from less than 2 to more than 3 leads to a decrease of the regression slope from 3.77 to

2.88. This supports the assumption that plant structure also plays an essential role in the overestimation. The more that stalks and ears influence the radiation signal, the less is the retrieval accuracy. This hypothesis is supported by the validation of CWC retrieved from CHRIS-PROBA data with field measurements. The analysis indeed yields an $R^2$ of 0.80 but provides a separation of different crop types depending on their physical structure. This is also visualized by a remarkable clustering in the scatter plot. Furthermore, by producing smoother and more plausible CWV maps we achieve an accuracy improvement of CWV retrieved from CHRIS-PROBA data instead from a band ratio retrieval in the presence of liquid water absorption. This indicates that the algorithm leads to improvements in atmospheric correction procedures.

As a confirmatory of previous studies, we additionally show results of the three phases retrieval applied to airborne AVIRIS-C data. Based on an evaluation of the derived CWC from a vegetated surface, we assume that imaging spectroscopy tracks changes in CWC better than multispectral indices, such as the NDWI. Furthermore, the snow/ice retrieval from AVIRIS-C data produces a good correlation with the NDSI with an $R^2$ of 0.94 illustrating the ability of the three phases retrieval to clearly distinguish between different quantities of ice. In fact, higher amounts are tracked better than by using the NDSI since it becomes saturated at a value of around 0.9.

In summary, our study shows that the presented surface reflectance model based on the Beer-Lambert law can indeed be improved with additional terms to account for physical processes such as volume scattering. Also, the retrieval accuracy could be increased by integrating, if available, a priori information about the type of vegetation and the structure of the canopy in the framework of optimal estimation. However, even without improvement, this process has delivered promising results, which are already interpretable regarding absolute retrieved CWC. Recently launched or upcoming spaceborne imaging spectroscopy missions like PRISMA or EnMAP will provide valuable input for a further validation of the three phases of water retrieval.

## Acknowledgments

This study is funded within the EnMAP scientific preparation program under the DLR Space Administration with resources from the German Federal Ministry for Economic Affairs and Energy, Berlin, Germany (grant ID 59EE1923) and the GFZ German Research Centre for Geosciences, Potsdam.

# Chapter 3

# Optimal estimation of snow and ice surface parameters

Niklas Bohn[1], Thomas H. Painter[2], David R. Thompson[3], Nimrod Carmon[3], Jouni Susiluoto[3], Michael J. Turmon[3], Mark C. Helmlinger[3], Robert O. Green[3], Joseph M. Cook[4], Luis Guanter[5].

**Publisher title:** Optimal estimation of snow and ice surface parameters from imaging spectroscopy measurements.
**Journal:** Remote Sensing of Environment, 264, 112613.
**Status:** Available online 5 August 2021.
**Publisher version:** https://doi.org/10.1016/j.rse.2021.112613.

[1]GFZ German Research Centre for Geosciences, Remote Sensing and Geoinformatics, Potsdam, Germany.
[2]Joint Institute for Regional Earth System Science and Engineering, UCLA, Los Angeles, CA, USA.
[3]Jet Propulsion Laboratory, California Institute of Technology, Pasadena, CA, USA.
[4]Department of Environmental Science, Aarhus Universitet, Roskilde, Denmark.
[5]Research Institute of Water and Environmental Engineering, UPV, Valencia, Spain.

# Chapter 4

# Glacier ice surface properties in South-West Greenland Ice Sheet

Niklas Bohn[1], Biagio Di Mauro[2], Roberto Colombo[3], David R. Thompson[4], Jouni Susiluoto[4], Nimrod Carmon[4], Michael J. Turmon[4], Luis Guanter[5].

**Publisher title:** Glacier ice surface properties in South-West Greenland Ice Sheet: first estimates from PRISMA imaging spectroscopy data.
**Journal:** Journal of Geophysical Research: Biogeosciences.
**Status:** Submitted 17 November 2021.
**Publisher version:** https://doi.org/10.1029/2021JG006718.

[1]GFZ German Research Centre for Geosciences, Remote Sensing and Geoinformatics, Potsdam, Germany.
[2]Institute of Polar Sciences, National Research Council of Italy, Venice, Italy.
[3]Earth and Environmental Sciences Department, University of Milano-Bicocca, Milan, Italy.
[4]Jet Propulsion Laboratory, California Institute of Technology, Pasadena, CA, USA.
[5]Research Institute of Water and Environmental Engineering, UPV, Valencia, Spain.

## Abstract

Snow and ice melt processes on the Greenland Ice Sheet are a key in Earth's energy balance and hydrological cycle, and they are acutely sensitive to climate change. Melting dynamics are directly related to a decrease in surface albedo, amongst others caused by the accumulation of light-absorbing particles (LAPs). Featuring unique spectral patterns, these accumulations can be mapped and quantified by imaging spectroscopy. In this contribution, we present first results for the retrieval of glacier ice properties from the spaceborne PRISMA imaging spectrometer by applying a recently developed simultaneous inversion of atmospheric and surface state using optimal estimation (OE). The image analyzed in this study was acquired over the South-West margin of the Greenland Ice Sheet in late August 2020. The area is characterized by patterns of both clean and dark ice associated with a high amount of LAPs deposited on the surface. We present retrieval maps and uncertainties for grain size, liquid water, and glacier algae concentration, as well as estimated reflectance spectra for different surface properties. We then show the feasibility of using imaging spectroscopy to interpret multiband sensor data to achieve high accuracy, fast cadence observations of changing snow and ice conditions. In particular, we show that glacier algae concentration can be predicted from the Sentinel-3 OLCI impurity index with less than 10% uncertainty. Our study evidence that present and upcoming orbital imaging spectroscopy missions such as PRISMA, EnMAP, CHIME, and the SBG designated observable, can significantly support research of melting ice sheets.


## 4.1 Introduction

Snow and ice melt processes on the Greenland Ice Sheet are a key in Earth's energy-balance and hydrological cycle, and they are acutely sensitive to climate change (Tedesco et al., 2016). Melting dynamics are directly related to environmental factors and to a decrease in surface albedo, amongst others caused by the accumulation of light-absorbing particles (LAPs), including both inorganic (i.e., mineral dust) and biological impurities (i.e., glacier algae) (Flanner et al., 2007; Skiles et al., 2018; Di Mauro, 2020). The magnitude of this absorption is controlled by LAP type, mass mixing ratio, and size distribution (Warren, 1982). Variability in snow and ice grain size caused by the presence of liquid water can also affect the surface reflectance (Dozier et al., 2009). At the same time, surface melting promotes the formation of cryoconite on bare ice, which is a supraglacial sediment composed of very fine organic and inorganic material transported by glacial streams

and therefore, leads to a further decrease of albedo by depositing LAP's on the ice surface (Sneed and Hamilton, 2011; Cook et al., 2016). The increasing amounts of melt water settle in supraglacial lakes, which play a crucial role in climate feedback processes and in the hydrological system of the Greenland Ice Sheet in general (Pope et al., 2016). Overall, snow and ice conditions can change on rapid timescales, and regular observations are critical to infer the rate at which accumulation, LAP deposition, and melt processes occur. A recent report by the National Academy of Sciences called for snow albedo observations on a weekly basis to constrain changes in the water and energy cycles (National Academies of Sciences, Engineering, and Medicine, 2018). Remote Sensing from space can significantly contribute to achieve these requirements by mapping local and global trends of snow and ice surface properties.

The most common variable of the cryosphere being monitored from space is the effective snow grain radius in $\mu m$ (Dozier, Schneider, and Jr., 1981). It is a measure of the ice crystal size and can also be expressed as specific surface area (Warren, 1982). Likewise, the spatial distribution and amount of LAP accumulation can be detected from space. In particular, depositions of algae in snow and glacier ice can be monitored by relying on chlorophyll and carotenoids absorption characteristics (Painter, Duval, and Thimas, 2001). Algal accumulation can be quantified as concentration in units of $cells\ ml^{-1}$ or as mass mixing ratio expressed in $\mu g/g_{snow/ice}$ (Painter, Duval, and Thimas, 2001; Cook et al., 2017b). Finally, the effective grain radius is also an indicator for surface wetness since the crystal size increases due to clustering processes in liquid water enriched snow and ice (Dozier et al., 2009). Alternatively, liquid water content can be expressed as spherical fraction of the snow and ice grains. However, this approach requires a separation of the liquid water and ice absorption lines and can therefore only be pursued by using imaging spectroscopy measurements (Green et al., 2002).

Optical remote sensing of snow and ice surface properties from space was among the earliest geophysical retrieval methods based on satellite missions and is a valuable tool to obtain amount and spatial distribution of different parameters on a global scale with a high temporal resolution (Rango and Itten, 1976). The potential of the near-infrared (NIR) wavelengths to estimate snow grain size was already demonstrated in the early 80's based on measurements from the NOAA Advanced Very High Resolution Radiometer (AVHRR) (Dozier, Schneider, and Jr., 1981). Prominent subsequent missions used to retrieve snow grain size include the Moderate Resolution Imaging Spectroradiometer (MODIS) (Zege et al., 2008; Zege et al., 2011; Carlsen et al., 2017), and the Sentinel-3 Ocean and Land Colour Instrument (S3 OLCI) (Kokhanovsky et al., 2019). The detection of biological LAP on snow

and ice surfaces has also been studied in detail and a couple of investigations focused on mapping glacier algal blooms and determining their effects on ice melt on the Greenland Ice Sheet (Takeuchi et al., 2006; Stibal et al., 2017; Wang et al., 2018; Wang et al., 2020; Cook et al., 2020; Gray et al., 2020). These studies applied retrieval algorithms to data from the Satellite Probatoire d' Observation de la Terre (SPOT), MODIS, S3 OLCI, the Medium Resolution Imaging Spectrometer (MERIS), or Sentinel-2.

In contrast to most of the existing optical satellite missions, imaging spectroscopy can be used to accurately map and quantify snow and ice surface properties using physically-based retrievals by modeling characteristic atmospheric and surface absorption features (Painter et al., 2013). So far, this technique has been almost entirely based on airborne spectrometers though, and in particular, on measurements from NASA's Airborne Visible Infrared Imaging Spectrometer (AVIRIS). Approaches to estimate snow grain size from AVIRIS data have been introduced by Nolin and Dozier (1993), and further developed by Nolin and Dozier (2000) and Painter et al. (2013). It has also been demonstrated that concentration of snow algal blooms can be quantified using AVIRIS acquisitions (Painter, Duval, and Thimas, 2001). The same instrument was used to quantify liquid water in-between the snow grains (Green et al., 2006). Recently, Bohn et al. (2021) demonstrated a promising potential of spaceborne imaging spectroscopy missions to simultaneously detect and quantify snow and ice grain size, liquid water, and glacier algal accumulation on the Greenland Ice Sheet based on simulated data and AVIRIS measurements. In this context, a new generation of orbital imaging spectroscopy missions is expected to provide much wider coverage on a more regular basis with high resolution footprints of only 30 $m$. The German Aerospace Center's (DLR) Earth Sensing Imaging Spectrometer (DESIS) (Mueller et al., 2016) and the Italian Hyperspectral Precursor of the Application Mission (PRISMA) (Cogliati et al., 2021) already are in operation since 2018 and 2019, respectively. Forthcoming missions include NASA's Earth Surface Mineral Dust Source Investigation (EMIT) (Green et al., 2018), the German Environmental Mapping and Analysis Program (EnMAP) (Guanter et al., 2015), the Copernicus Hyperspectral Imaging Mission (CHIME) led by ESA (Rast et al., 2019), and NASA's Surface Biology and Geology (SBG) designated observable (National Academies of Sciences, Engineering, and Medicine, 2018).

In this work, we present the first estimation of snow and ice surface properties from existing spaceborne imaging spectroscopy data. We apply a recently developed simultaneous Bayesian inversion of atmospheric and surface state using optimal estimation (OE). The algorithm was introduced by Bohn et al. (2021) and is an extended version of the concept presented in Thompson et al. (2018). It incorporates

prior knowledge, measurement noise as well as model uncertainties. We use a dataset from the PRISMA instrument in order to map and quantify ice grain size, surface liquid water, and algae mass mixing ratio. The image was acquired over the South-West margin of the Greenland Ice Sheet in late August 2020 capturing the "dark zone" or "k-transect", which is characterized by patterns of clean snow and dark ice featuring high concentration of deposited LAPs (Wientjes et al., 2011). We present retrieval maps and associated posterior uncertainties, as well as estimated reflectance spectra for different surface conditions. We also analyze the optical properties of melt ponds or supraglacial lakes, which are numerous in the selected PRISMA acquisition. In addition to presenting the new spectroscopic retrievals, we finally show how these measurements can be used in concert with multiband data in a comprehensive cryosphere observation system. We demonstrate for the first time that simple local regression models applied to multispectral S3 OLCI data can achieve a high degree of alignment with retrieval maps from imaging spectroscopy measurements.

## 4.2 Methods

### 4.2.1 Spectroscopic snow and ice property retrievals

The algorithm our study is based relies on statistical relationships between surface reflectance spectra and snow and ice properties to estimate the most probable solution state given a particular reflectance. It is based on the principles of OE described by Rodgers (2000) and uses a comprehensive library of reflectance spectra and associated snow and ice surface parameters as a representation of prior knowledge. Bohn et al. (2021) named this approach a "lazy Gaussian" or "lazy prior-driven" inversion since the forward model is a function of the atmospheric state and the surface reflectance, but not of the additional surface parameters. These extra parameters are estimated entirely based on the prior mean and covariance with the surface reflectance. They comprise grain radius, liquid water path length as well as mass mixing ratios of various LAPs. The statistical correlations between reflectance and surface properties are derived from runs of the snow and ice radiative transfer model (RTM) BioSNICAR-GO.

BioSNICAR-GO simulates surface spectral albedo by combining a bio-optical model with the two-stream multilayer SNow, ICe, and Aerosol Radiation model SNICAR (Flanner et al., 2007; Cook et al., 2020). It facilitates the modeling of ice grains and LAP either as collections of spheres based on Lorenz-Mie theory (Grenfell and Warren, 1999) or as arbitrarily large hexagonal plates and columns using a

geometric optics (GO) parameterization from Diedenhoven et al. (2014). To enable the estimation of surface liquid water, Bohn et al. (2021) coupled BioSNICAR-GO with the two-layer coated sphere reflectance model developed by Green et al. (2002). The model assumes an increased grain radius attributed to a particular liquid water fraction, and is based on a slight shift between the imaginary parts of the spectral refractive index of liquid water and ice (Dozier and Painter, 2004).

This section presents a brief discussion of the difference in modeling of snow and ice grains, followed by an overview about the forward model and OE in general. We adhere to standard conventions and denote matrices with uppercase boldface letters, and vectors as well as vector-valued functions with a lowercase boldface notation. For in-depth details, the reader is referred to Rodgers (2000), Thompson et al. (2018), and Bohn et al. (2021).

#### 4.2.1.1 Snow vs. ice grains

Most of the scientific literature on the retrieval of snow and ice surface parameters is focused on snow grain size (see, e.g., Nolin and Dozier (1993), Nolin and Dozier (2000), Painter et al. (2013), Kokhanovsky et al. (2019)). However, the optical properties of ice crystals are very different compared to snow, which is a mixture of air and ice (Warren, 2019). There is an inner complexity in estimating ice grain dimensions since the transition from snow to glacier ice is a continuum. On ice sheets, snow is compressed by its own weight and with increasing density, present air forms enclosed bubbles. The higher the density and the pressure, the smaller the bubbles get until they finally dissolve to spare pure ice (Warren, 2019).

The most common method to model the shape of snow grains is to assume non-spherical snow particles being arranged as a collection of spheres and to obtain their optical properties from Lorenz-Mie theory (Grenfell and Warren, 1999). This approach is justified by expecting the snow grain radius being much larger than the incident radiation wavelengths. However, this method features clear limitations when applied to surfaces of bare ice since the grains typically appear to be arbitrarily shaped as plates and columns with irregular dimensions (Kokhanovsky and Zege, 2004). To capture this in the modeling, Aoki et al. (2007) proposed to consider length, width, and thickness of the ice crystals instead of the collected-spheres approach. These parameters are likewise the basis of the geometric optics (GO) calculations introduced by Kokhanovsky and Zege (2004).

In this study, we run the "lazy Gaussian" inversion based on both the collected-spheres and the GO method representing the prior distributions. Although the simulated spectra for glacier ice surfaces display the more appropriate prior mean

and covariance for our case study, we also applied the Lorenz-Mie based snow spectral library to our PRISMA dataset to enable a comparison with the grain radius maps derived from S3 OLCI data. Furthermore, this demonstrates the resulting differences both in spatial distribution and value range of the estimated grain sizes, and therefore, gives an impression of the applicability of the different approaches to model snow and ice grain shape. Figure 4.1d shows representative surface reflectance spectra of clean snow and dark ice, respectively, with highlighted characteristic absorption features. Abundance of carotenoids and chlorophyll indicates presence of biological impurities on the surface, whereas ice and liquid water absorption bands are used for retrieving grain size as well as liquid water content. The spectra highlight the differences in reflectivity of snow and ice surfaces and thus, confirm the importance of choosing an appropriate prior knowledge for the inversion.

#### 4.2.1.2 Forward model

We denote the forward model as a vector-valued function $\mathbf{f}$ of the state vector $\mathbf{x} = [x_1, ..., x_n]^T$ yielding the measurement vector $\mathbf{y} = [y_1, ..., y_m]^T$:

$$\mathbf{y} = \mathbf{f}(\mathbf{x}) + \boldsymbol{\epsilon}, \tag{4.1}$$

with $\epsilon$ representing a random error vector, which in our case includes measurement noise, prior uncertainties in $\mathbf{x}$, and errors due to unknown forward model parameters. Following Thompson et al. (2018), $\mathbf{x}$ contains columnar water vapor in $g\ cm^{-2}$ and dimensionless Aerosol Optical Thickness (AOT) at 550 $nm$ being an atmospheric part $\mathbf{x}_{\mathrm{ATM}} = [x_{\mathrm{H_2O}}, x_{\mathrm{AOT}}]^T$, and the reflectance of each instrument channel as a surface part $\mathbf{x}_{\mathrm{SURF}}$. Here, the snow and ice properties are added leading to the extended version $\mathbf{x}_{\mathrm{SURF}} = [x_{\lambda_1}, ..., x_{\lambda_m}, x_{\mathrm{SURF}_1}, ..., x_{\mathrm{SURF}_n}]^T$. Thompson et al. (2018) use the hemispherical-directional reflectance factor (HDRF) as a representation of the surface reflectance. In contrast, our implementation of the "lazy Gaussian" method optimizes the hemispherically-integrated spectral albedo. This approach is limited by the used 2-stream snow and ice RTM BioSNICAR-GO. However, although the HDRF is the more appropriate quantity when modeling measurements of imaging spectrometers (Schaepman-Strub et al., 2006), the use of spectral albedo for applications to the flat parts of the Greenland Ice Sheet can be pursued (Bohn et al., 2021).

In specific form, $\mathbf{f}$ models the wavelength-dependent top-of-atmosphere (TOA) radiance using a simplified solution of the radiative transfer equation (Chandrasekhar, 1960):

$$L_{\mathrm{TOA}} = L_0 + \frac{1}{\pi}\frac{\rho_s(E_{\mathrm{dir}}\mu_{\mathrm{sun}} + E_{\mathrm{dif}})T_{\uparrow}}{1 - S\rho_s}, \tag{4.2}$$

where $L_0$ is the atmospheric path radiance; $E_{\text{dir}}$ and $E_{\text{dif}}$ are the direct and diffuse solar irradiance arriving at the surface; $\mu_{\text{sun}}$ is the cosine of the solar zenith angle; $T_{\uparrow}$ is the total upward atmospheric transmittance; $S$ is the spherical albedo of the atmosphere; and $\rho_{\text{s}}$ is the surface spectral albedo. For simplicity, we assume an infinite, horizontal, and isotropic Lambertian surface as well as clear sky and a plane-parallel atmosphere. At the same time, these assumptions ensure validity of using spectral albedo in place of HDRF (Bohn et al., 2021). The atmospheric flux parameters $L_0$, $E_{\text{dir}}$, $E_{\text{dif}}$, $T_{\uparrow}$, and $S$ are functions of $\mathbf{x}_{\text{ATM}}$, surface elevation as well as solar and observation geometry. They are derived from radiative transfer simulations using the MODTRAN code (Berk, Bernstein, and Robertson, 1989). The prior covariance matrix of $\mathbf{x}_{\text{ATM}}$ is assumed to be diagonal and unconstrained.

While the first part of the surface state vector, $[x_{\lambda_1}, ..., x_{\lambda_{\text{m}}}]$, is expressed by $\rho_{\text{s}}$ in $\mathbf{f}$, the remaining parameters of $\mathbf{x}_{\text{SURF}}$, $[x_{\text{SURF}_1}, ..., x_{\text{SURF}_{\text{n}}}]$, are not an input to the forward model. They are optimized entirely based on their prior mean and covariance, which are obtained from the prior surface statistics. These statistics are characterized by a multivariate Gaussian distribution of surface reflectance for each instrument channel and the additional surface parameters with a non-diagonal covariance matrix due to expected correlations across channels.

#### 4.2.1.3 Optimal estimation

OE acts on two main assumptions: measurement and state vectors as well as the associated errors follow a Gaussian distribution, and the forward model is locally linear. Then, $\mathbf{f}$ can be inverted by minimizing the following cost function, which is the negative logarithm of the posterior probability density function:

$$\mathcal{C}(\hat{\mathbf{x}}) = \frac{1}{2}(\hat{\mathbf{x}} - \mathbf{x_a})^{\text{T}}\mathbf{S}_{\text{a}}^{-1}(\hat{\mathbf{x}} - \mathbf{x_a}) + \frac{1}{2}\big(\mathbf{y} - \mathbf{f}(\hat{\mathbf{x}})\big)^{\text{T}}\mathbf{S}_{\epsilon}^{-1}\big(\mathbf{y} - \mathbf{f}(\hat{\mathbf{x}})\big). \tag{4.3}$$

Here, $\mathbf{x_a}$ is the prior state vector; $\mathbf{S}_{\text{a}}$ is the prior covariance matrix; and $\mathbf{S}_{\epsilon}$ is the measurement covariance matrix. The first term of the right-hand side penalizes the departure of the modeled TOA radiance from the measurement, weighted by $\mathbf{S}_{\epsilon}$, which captures both instrument noise, expressed by the noise-equivalent change in radiance, and uncertainties due to unknown forward model parameters. We assume no correlation between the measurement noise of different instrument channels as well as between the unknown parameters, so that $\mathbf{S}_{\epsilon}$ is diagonal. The second term evaluates the difference between prior and solution state by taking into account $\mathbf{S}_{\text{a}}$. The iteration then searches for the solution state $\hat{\mathbf{x}}$ that leads to a local minimum of Equation 4.3, being the state with the highest probability given the measurement

and the prior state. In this work, we find $\hat{\mathbf{x}}$ using a Gauss-Newton iteration scheme that typically converges in less than 30 iterations.

Besides the converged solution state, the OE retrieval scheme reports the posterior predictive uncertainty for each $\hat{\mathbf{x}}$:

$$\hat{\mathbf{S}} = (\mathbf{K}^{\mathrm{T}}\mathbf{S}_{\epsilon}^{-1}\mathbf{K} + \mathbf{S}_{\mathrm{a}}^{-1})^{-1}, \tag{4.4}$$

where $\mathbf{K}$ is the Jacobian of the forward model with respect to $\hat{\mathbf{x}}$. To facilitate an interpretation of the posterior uncertainties, $\hat{\mathbf{S}}$ can be normalized leading to an error correlation matrix (Govaerts et al., 2010).

### 4.2.2 Sentinel-3 OLCI snow property retrievals

Measurements from S3 OLCI can be used to derive several snow properties including spectral and broadband albedo, snow specific surface area, snow extent, and snow grain size (Kokhanovsky et al., 2019). Additionally, multiple band indices have been developed for identifying impurities on snow and ice surfaces from instruments such as MERIS, MODIS, or S3 OLCI, including different chlorophyll indices and the impurity index (Wang et al., 2018; Wang et al., 2020; Dumont et al., 2014). In this section, we briefly introduce the S3 OLCI grain size retrieval algorithm as well as the impurity index, as results from both are used for comparison with retrieval maps from PRISMA data.

The snow grain radius is estimated from S3 OLCI data using the following relation (Kokhanovsky et al., 2019):

$$r = \frac{Al}{2}, \tag{4.5}$$

where $l$ is the effective ice absorption length, and $A$ is derived from a scaling constant depending both on snow type and grain shape. Kokhanovsky et al. (2019) suggest $A = 0.06$ based on findings from various studies, which analyze the scaling constant (see Kokhanovsky (2006), Libois et al. (2014), Di Mauro et al. (2015)). The absorption length $l$ is calculated by:

$$l = \frac{1}{\alpha_2 f^2} ln(\frac{R_2}{R_1}), \tag{4.6}$$

where $R_1$ and $R_2$ are the OLCI TOA reflectance at 865 and 1020 $nm$, $\alpha_2$ is the ice absorption coefficient at 1020 $nm$, and $f$ is an angular function that depends on solar and viewing geometry as well as on the theoretical reflectance of a non-absorbing snow layer. The important assumptions of this approach are that $R_1$ and

$R_2$ have to be sensitive to the snow grain radius and least influenced by atmospheric absorption and scattering (Kokhanovsky et al., 2019). For more details about the algorithm the reader is referred to Kokhanovsky et al. (2019).

The impurity index was introduced by Dumont et al. (2014) and exploits the much higher sensitivity of the visible (VIS) wavelengths to impurity content compared with the near-infrared (NIR) spectral region. It is calculated by the ratio of the natural logarithms of green and NIR surface reflectance at 560 and 865 $nm$, respectively:

$$i_{imp} = \frac{ln(R_{560\ nm})}{ln(R_{865\ nm})}. \tag{4.7}$$

Dumont et al. (2014) showed that $i_{imp}$ is almost non-sensitive to the ice grain size, whereas it can be affected by atmospheric aerosols in case of biased atmospheric correction results. An accurate surface reflectance retrieval is therefore needed prior to calculating $i_{imp}$. Furthermore, Di Mauro et al. (2017) demonstrated that $i_{imp}$ is also sensitive to mineral dust and black carbon concentration on ice surfaces. Typical values of the impurity index are $0.2 - 0.5$ for bare ice, $0.7 - 0.9$ for low to moderate chlorophyll content, and more than 0.9 for high chlorophyll concentration (Wang et al., 2020). Its values can reach up to 1.2 for high loads of impurities and cryoconite on bare ice (Di Mauro et al., 2017).

## 4.3 Materials

### 4.3.1 Study area

Our study area is located at the South-West margin of the Greenland Ice Sheet at 66° – 68° N and 48° – 50° W. It belongs to the Kangerlussuaq transect (k-transect) and is characterized by patterns of clean snow and dark ice. Especially in the summertime, i.e., July and August, the k-transect features a low surface albedo forming a zone of dark ice (Alexander et al., 2014; Ryan et al., 2018). This process is highly correlated with meltwater production and runoff as well as with associated occurrences of algal blooms on the ice surface (Wang et al., 2018; Cook et al., 2020; Bohn et al., 2021). As shown by previous studies, the predominant species of biological impurities during the melt season in the dark zone are *Mesotaenium berggrenii* and *Ancylonema nordenskioldii* (Yallop et al., 2012; Williamson et al., 2018). In fact, these eukaryotic species are known to dominate the supraglacial environment both in Greenland and elsewhere (Di Mauro et al., 2020). Additionally, the large amount of meltwater production leads to the development of several widespread melt ponds (Diamond et al., 2021).

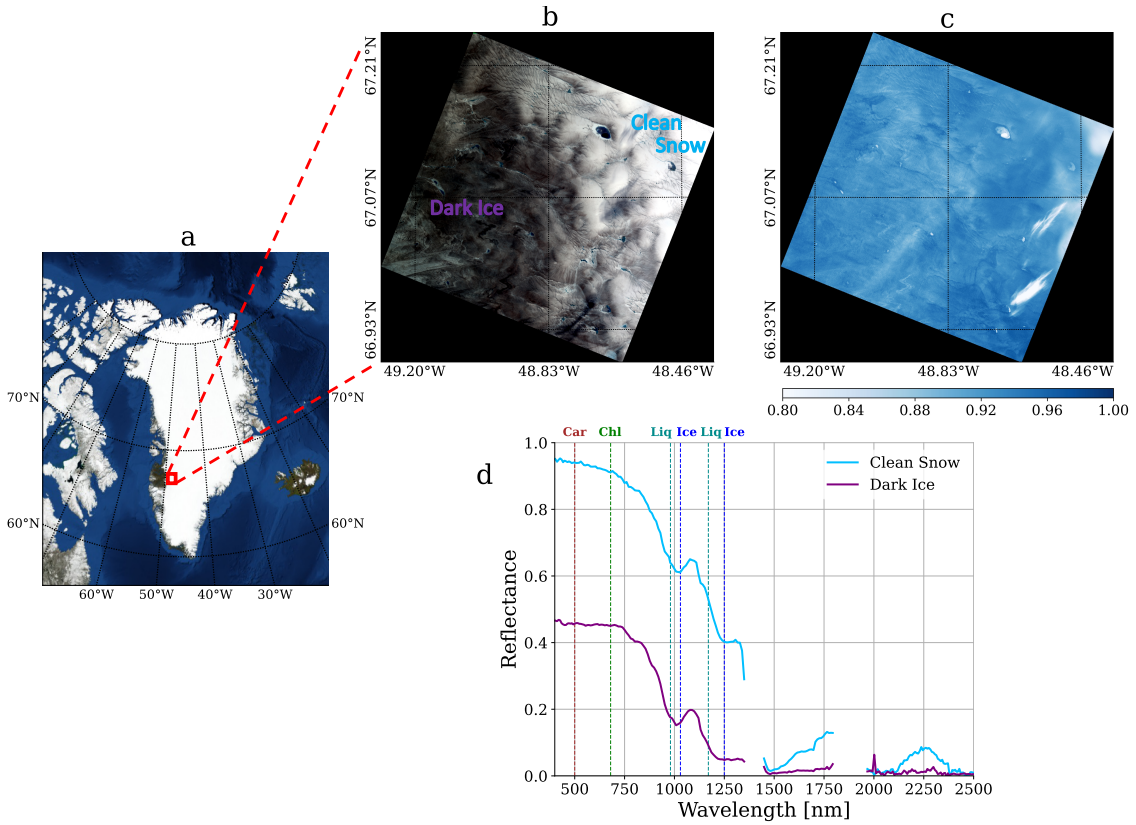


FIGURE 4.1: a) Map of Greenland showing the location of the PRISMA acquisition as a red box; b) a true-color image of the TOA radiance dataset; c) the normalized difference snow index (NDSI) calculated from the difference between the VIS green and shortwave infrared (SWIR) TOA reflectance; and d) exemplary surface reflectance spectra estimated from PRISMA TOA radiance data for clean snow and dark ice, respectively. Center wavelengths of characteristic absorption features of carotenoids (Car), chlorophyll (Chl), liquid water (Liq), and ice (Ice) are highlighted with dashed lines.

### 4.3.2 PRISMA data

PRISMA is an Italian satellite mission led by the Italian Space Agency (ASI) (Cogliati et al., 2021). The instrument was launched in March 2019 and provides on-demand data for most of the Earth. It features 239 spectral bands covering the wavelength region from 400 to 2500 $nm$ with a spectral sampling interval (SSI) less than 12 $nm$. The ground sampling distance (GSD) is 30 $m$, while the swath is 30 $km$.

For our study, we selected an acquisition from August 30, 2020, covering a part of the k-transect. Figure 4.1a-b shows a true-color representation of the scene and its location on the Greenland Ice Sheet. The image contains representative examples of both clean snow and dark ice at the end of the melting season. Several melt ponds are also displayed. After converting PRISMA L1 TOA radiance data to reflectance, we calculated the normalized difference snow index (NDSI) (Dozier, 1989), which is visualized in Figure 4.1c. We mostly obtain an NDSI beyond 0.8 with 0.74 being the

minimum value of the entire image, which clearly indicates that the surface is covered with snow and ice (Dozier and Painter, 2004). We can also observe some smooth structures towards the East showing lower values of NDSI, which might be some thin clouds not easily detectable in the true-color image. Stillinger et al. (2019) have shown that the NDSI of dark clouds can be high enough to cause misclassification.

In order to improve the radiometric and spectral quality of the selected PRISMA data, we applied a suite of preprocessing tools, including a spectral smile correction and a radiometric radiance correction (Chlus, Townsend, and Gierach, 2021).

To obtain the individual noise-equivalent change in radiance for each PRISMA spectrum needed by the OE-based inversion, we use an estimation of the signal-to-noise ratio (SNR) based on a discrete cosine transform and scale the results assuming a photon shot noise square root dependence with the radiance (Gorroño and Guanter, 2021).

### 4.3.3 Sentinel-3 OLCI data

OLCI is a moderate resolution imaging spectrometer installed on the Sentinel-3 satellite, which was launched in 2016. The instrument provides 21 spectral bands spanning 400 to 1020 $nm$ with an SSI between 2.5 and 40 $nm$. With $1,270$ $km$ and 300 $m$, it features much larger swath and GSD, respectively, than the PRISMA imaging spectrometer. OLCI was specifically designed for retrieving chlorophyll content, primarily over ocean surfaces, which is highly facilitated by its large footprint (Malenovský et al., 2012).

For the comparison with our PRISMA dataset, we selected an OLCI acquisition from the same date, i.e., August 30, 2020, and almost the same time of overpass, i.e., approximately 15:00 GMT-2. The scene covers large parts of the western shore of the Greenland Ice Sheet and part of the Canadian arctic. It includes our study area in the k-transect of southwest Greenland and shows a slightly larger cloud fraction, which is mainly located over water surfaces though. We used the OLCI L1B product providing radiometrically calibrated TOA radiances and converted the data both to TOA and surface reflectance using the S3 OLCI Snow and Ice Properties Processor (SICE). Details on SICE can be found in Kokhanovsky, Box, and Vandecrux (2020). Subsequently, we produced a snow grain size map and calculated the impurity index for each pixel using OLCI bands 6 at 560 $nm$ and 17 at 865 $nm$.

## 4.4 Results and discussion

### 4.4.1 Snow and ice parameter maps

The left panel of Figure 4.2 quantifies the spatial distribution of ice grain radius, ice liquid water path length, and glacier algae mass mixing ratio from the PRISMA data using the glacier ice spectral library as prior knowledge. Comparing the maps with the true-color image in Figure 4.1b, it is obvious that the darker the surface, the larger are the estimated ice grains and the algae concentration since high amounts of both quantities lead to decreasing reflectance in the VIS (Bohn et al., 2021). Likewise, the liquid water path length detected on the ice surface is significantly larger for the dark zone in the western part. The algae map is calculated from the sum of retrieved values of the species *Mesotaenium berggrenii* and *Ancylonema nordenskioldii*, and conforms to values measured in the field (Cook et al., 2020).

Figure 4.3 illustrates these findings by showing spatial transects of ice grain radius, ice liquid water path length, and glacier algae mass mixing ratio at 67.14° N. We selected this particular latitude as this transect not only covers the dark zone and clean ice and snow, but also the large dark melt pond located in the north-eastern part of the image. Between 48.5° and 48.8°W, the transect can generally be characterized as transition area from the dark zone near the coastline towards the clean ice at higher elevated parts of the Ice Sheet. This transition area is interrupted by some small scale accumulations of glacier algae around melt ponds, which typically cause algal disposition in the surrounding area. In contrast, we observe constantly large ice grain radii and ice liquid water path lengths as well as high algae concentration within the dark zone. The discrete spike in all transects between 48.8° and 48.9° W originates from a small and shallow melt pond, whose brighter reflectance properties are most likely influenced by underlying bare ice featuring a smaller grain radius and very low algae concentration. On the other hand, the dark melt pond is characterized by large estimated ice grains and high concentration of glacier algae (see Section 4.4.5 for a detailed analysis). Finally, the region of clean ice and snow shows small grain radii, less liquid water on the ice surface, and almost no biological impurities. Overall, the reported value ranges for the various parameters coincide with findings from previous studies (Cook et al., 2020; Bohn et al., 2021). Especially the comparison with samples of algal field measurements collected and provided by Cook et al. (2020) proves a similar value range of mass mixing ratios remotely retrieved from PRISMA data (Figure 4.3). In fact, the concentrations observed in the field are slightly lower, but this is probably due to an earlier sampling date within the melting season, i.e., mid of July instead of late August. Furthermore, the results from the PRISMA data rather represent

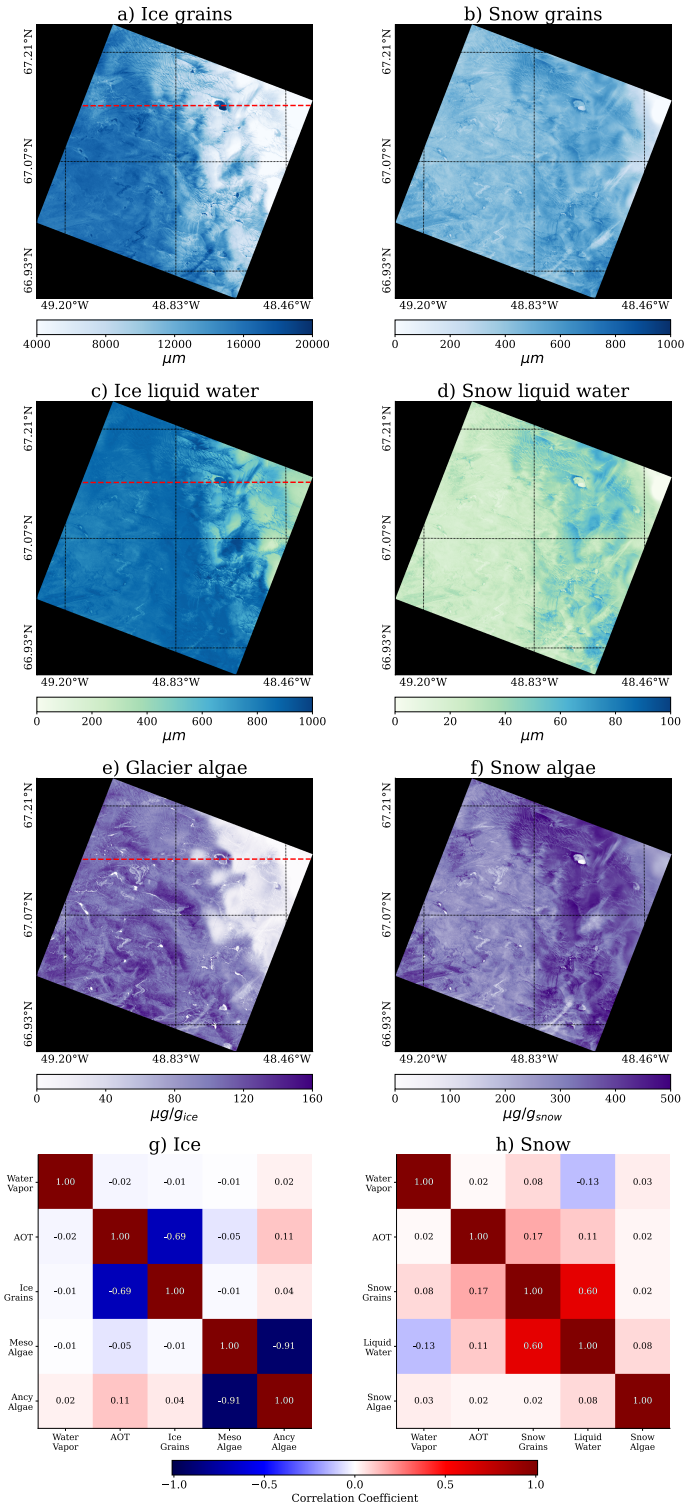


FIGURE 4.2: Estimated surface parameter maps from PRISMA data using different spectral libraries as prior knowledge. Left panel: glacier ice; right panel: snow. a-b) Grain radius; c-d) liquid water path length; e-f) algae mass mixing ratio; and g-h) posterior error correlation matrices for selected atmosphere and surface state parameters. The dashed red lines in a, c, and e indicate the latitude that is selected to create the spatial transects in Figure 4.3.

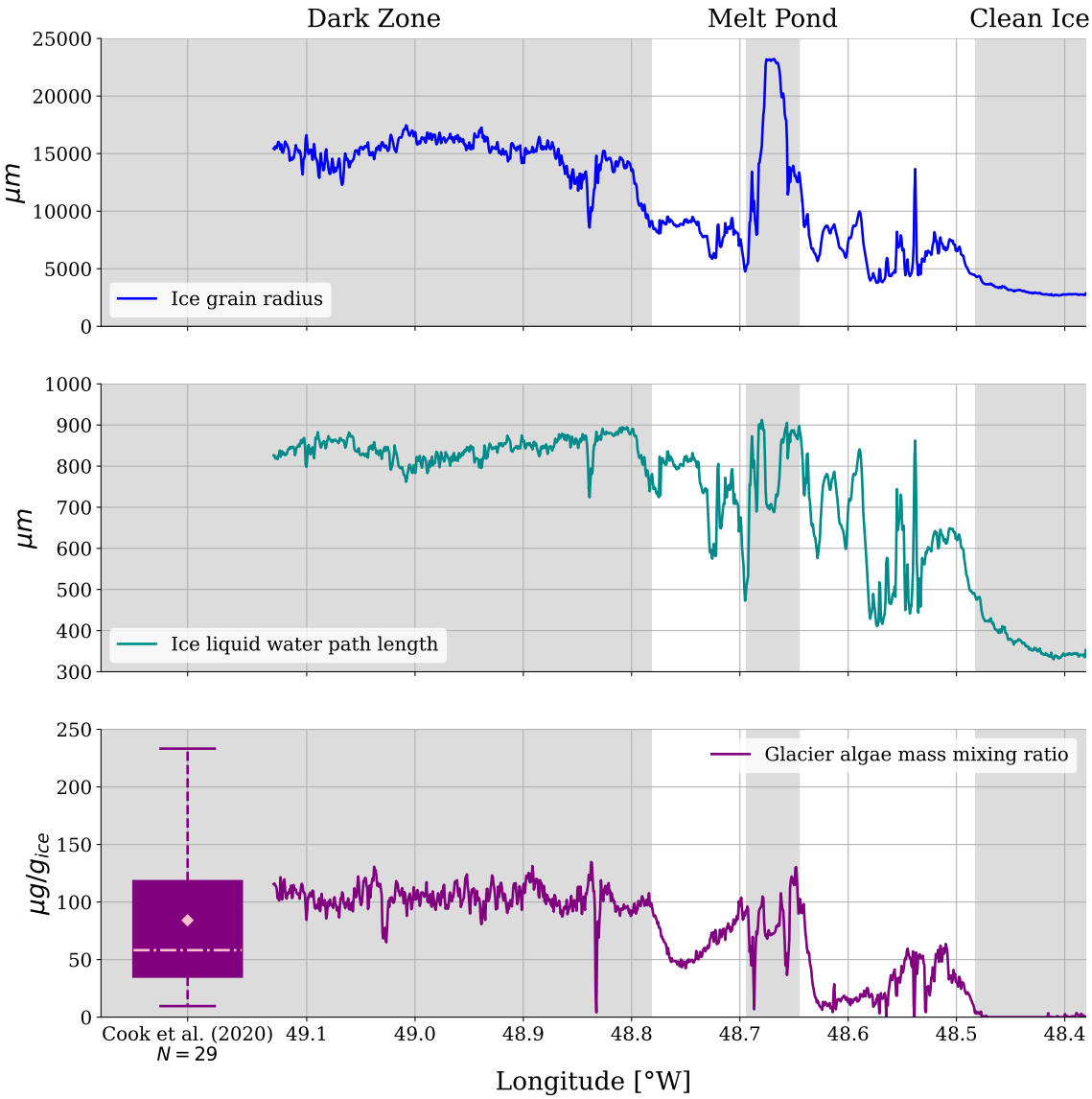


FIGURE 4.3: Spatial transects of estimated ice grain radius, ice liquid water path length, and glacier algae mass mixing ratio at 67.14° N (see dashed red lines in the left panel of Figure 4.2). The selected latitude covers the dark zone of high impurity concentration as well as a large dark melt pond and an area of clean ice and snow in the eastern part of the image. The lower panel is complemented by a boxplot calculated from samples of algal field measurements collected between 10 and 17 July 2017 within the k-transect by Cook et al. (2020). The pink dashed line and the pink colored point show median and mean of the distribution, respectively.

average values of $30 \times 30$ $m$ pixels than point measurements. Thus, the mean of the algal field measurements, indicated by a pink colored point within the boxplot, is the more appropriate quantity to compare with.

The right panel of Figure 4.2 presents the estimated maps for snow grain radius, snow liquid water path length, and snow algae mass mixing ratio using the Lorenz-Mie based snow spectral library as prior knowledge. In contrast to the retrieved ice grain size, a correlation with surface brightness is not observable for the snow grain radius. In fact, this retrieval ideally works for sphere-shaped snow grains, so that the reported values for the dark ice surface have to be treated carefully. Towards the most eastern part, the map features smaller grain radii potentially related to the increasing surface elevation, which rises from 1000 to 1500 $m$ in our PRISMA image and leads to lower air temperatures when moving landwards. Under these conditions, generally dry snow with small grain size is found on the surface (Warren, 2019). Several studies well describe the spatial distribution of snow grain size including its decline on the uplifted parts of the Greenland Ice Sheet (see, e.g., Kokhanovsky et al. (2019) or Bohn et al. (2021)). The estimated snow liquid water path lengths confirm the retrieved snow grain size map since the highest values can be observed for pixels with large grain radii of up to 800 to 1000 $\mu m$. The grains in liquid water enriched wet snow tend to form clusters, which behave as larger grains with the respective optical properties (Dozier et al., 2009). Finally, the snow algae map in Figure 4.2f points out the importance of selecting appropriate priors for the inversion. Applying the snow spectral library to retrievals on glacier ice surfaces obviously leads to less realistic results of algae concentration. The estimated mass mixing ratios do not correlate with surface brightness and show artificially high values when compared to the field observations of Cook et al. (2020) (see Figure 4.3). This is mainly due to the different approaches of modeling the shape of both snow and ice grains and the algal cells. Relying on prior knowledge based on GO calculations significantly enhances the retrieval results since it simulates existing conditions on glacier ice surfaces more appropriately (Cook et al., 2020).

### 4.4.2 Posterior error correlation

Then, we present posterior error correlation matrices for selected atmosphere and surface parameters to show how retrieval uncertainties of particular state vector elements affect each other. We calculated the mean coefficients from the posterior predictive uncertainties for all $\hat{\mathbf{x}}$ of the PRISMA image. Depending on the used surface prior spectral library, Figure 4.2g-h divides into glacier ice and snow surface parameters.

Although we do not analyze the retrieval of the atmospheric state $\mathbf{x}_{\mathrm{ATM}}$ in this study, we take a look at potential effects of water vapor and AOT on the additional surface parameters. Whereas water vapor uncertainties are clearly uncorrelated with all other parameters over glacier ice, a negative correlation between errors in the ice grain retrieval and the AOT estimation can be observed. Scattering and absorption by atmospheric aerosols show similar effects on the reflectance shape and magnitude in the VIS as increasing ice grain radii. Thus, corresponding retrieval uncertainties are introduced, which was one of the key findings in Bohn et al. (2021). Furthermore, posterior errors for the glacier algae species are strongly negatively correlated since their absorption features are similar (Cook et al., 2020). However, we report the sum of both in the retrieval maps, so that potential inaccuracies compensate for each other.

Figure 4.2h illustrates the positive correlation between uncertainties in the snow grain size retrieval and errors in the liquid water estimation. This is most likely due to the similarities between liquid and ice absorption shapes (Green et al., 2006). Even errors in the solution state for atmospheric water vapor can be little affected by posterior uncertainties in the surface liquid water estimation. However, the respective correlation coefficient is only $-0.13$ and likewise, the remaining values of the matrix are more or less close to 0. Overall, Figure 4.2g-h confirms the independence of most state vector parameters and therefore, our ability to estimate them with the "lazy Gaussian" inversion.

### 4.4.3 TOA radiance fits

Next, we present a comparison between PRISMA L1 data and the respective TOA radiance fits, modeled by Equation 4.2. As an example, the upper panel of Figure 4.4 shows three selected spectra of different Ice Sheet surface types as highlighted in Figure 4.3. The left panel represents a clean snow surface in the eastern part of the image featuring small ice crystals, a smaller liquid water path length, and no algae accumulation. In contrast, the spectrum in the middle panel originates from a dark ice pixel in the ablation zone having large ice crystals, a large liquid water path length, and a high glacier algae mass mixing ratio. Finally, the right panel emphasizes the radiative and reflective properties of the dark melt pond located on the spatial transect drawn in the left panel of Figure 4.2.

While showing almost no residuals in the SWIR, all spectral fits illustrate discrepancies of up to 2 $\mu W nm^{-1} cm^{-2} sr^{-1}$ in the VIS/NIR wavelength region. Generally, the modeled TOA radiance rather underestimates the measured PRISMA L1 data, except for the NIR part of the melt pond spectrum. However, we observe slightly different spectral regions of largest error occurrence. The radiance fit for the dark

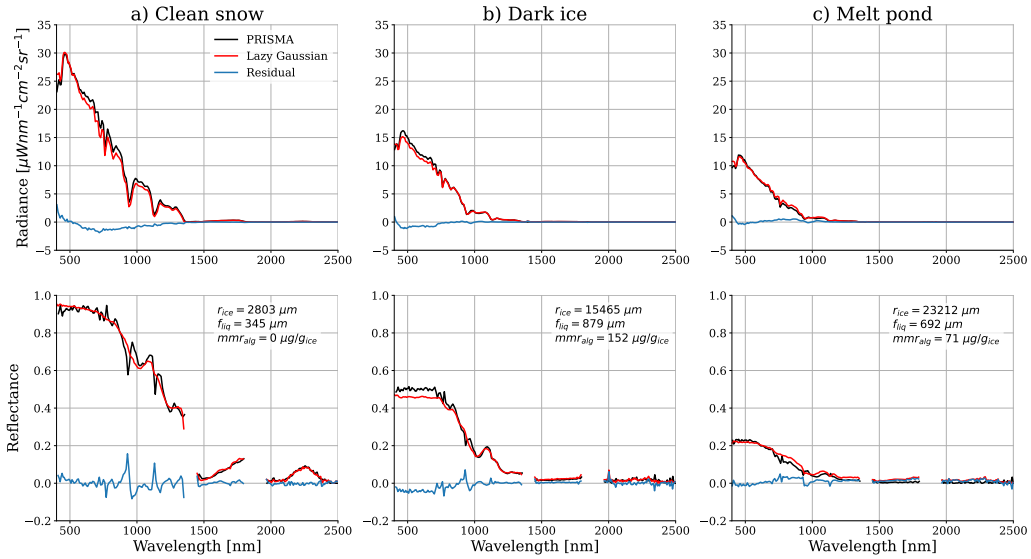


FIGURE 4.4: TOA radiance fits and estimated surface reflectance for three selected Ice Sheet surface types. a) Clean snow with small ice crystals, smaller liquid water path length, and no algae accumulation; b) dark ice with large ice crystals, large liquid water path length, and high algae accumulation; and c) dark melt pond with very large ice crystals, medium liquid water path length, and moderate algae accumulation. The upper panel shows fits between PRISMA L1 data and the forward modeled radiance at convergence. The lower panel presents a comparison of reflectance solution states with the PRISMA L2C product. The blue lines in all plots depict the absolute residuals between PRISMA data and the lazy Gaussian results.

ice surface almost exclusively deviates from the PRISMA measurement between 400 and 750 $nm$, where the TOA radiance signal is strongly affected by the scattering of atmospheric aerosols. An explanation is directly presented in Figure 4.2g. Here, we notice a correlation coefficient of $-0.69$ between errors in the ice grain radius retrieval and the AOT estimation. Therefore, the AOT value reported in the solution state for the dark ice spectrum might be overestimated due to an underestimated ice grain radius. This reduces the modeled radiance in the VIS. Additionally, the AOT estimation is biased by a missing first guess retrieval prior to the inversion.

The fit for the clean snow spectrum shows less influences by the AOT retrieval in the VIS. Here, we observe the largest model discrepancies in the NIR wavelength region. As the inversion reports a much smaller ice grain radius, but remarkably higher relative liquid water fraction, the residuals might be explained by error correlation in-between the three phases of water, i.e., atmospheric water vapor, surface liquid water, and ice grain radius. Figure 4.2h confirms this assumption since we note correlation coefficients of 0.60 between snow grain and liquid water retrieval uncertainties as well as at least $-0.13$ for errors in water vapor estimation and the reported liquid water fraction.

Finally, the radiance fit for the melt pond spectrum slightly deviates from the

PRISMA L1 data in the blue VIS region, but shows larger differences in the NIR wavelength range. The former is most likely caused by uncertainties in the AOT estimation, while the latter might be explained by insufficient surface prior knowledge. The applied spectral libraries of snow and ice reflectance do not include simulations for melt pond surfaces and consequentially, the prior state vector does not cover these characteristics in the inversion. This is also reflected in the estimated ice crystal size for this spectrum. The inversion reports a disproportionately large radius of 23212 $\mu m$, although we rather find open water than ice-covered surface in this pixel. Here, the solution state of the ice crystal size is clearly guided by the relatively low radiance, which is commonly observed for water surfaces.

Overall, the discrepancies in modeled TOA radiance may also originate from too strong constraints on the surface reflectance priors. The optimization then attends less to the measurement part of the cost function and consequentially, models $\mathbf{y}$ with a higher associated uncertainty. Increasing the surface reflectance diagonal of the prior covariance matrix may improve the performance of our forward model. Also, uncertainties introduced by the radiometric calibration of the instrument itself might be another source of errors influencing the TOA radiance fits.

Finally, we presume though that at least the amount of algae accumulation on the ice surface has less effects on the fitted TOA radiance. Bohn et al. (2021) have shown that the information content of the radiance measurement is almost unaffected by biological impurities. However, small errors might still remain in the TOA radiance fits.

### 4.4.4 Estimated surface reflectance

Since the "lazy Gaussian" inversion is embedded in an atmospheric correction algorithm and the spectral albedo for each instrument channel are elements of the state vector, the evaluation of the retrieved surface reflectance is an essential part of our analysis. Although we lack appropriate field measurements for validation, a qualitative comparison with the official PRISMA L2C product is informative. Since our resulting reflectance map is yet in sensor geometry similar to the PRISMA L1 product, we use the L2C data for comparison instead of the final orthorectified L2D product.

The lower panel of Figure 4.4 shows results for the same pixels as analyzed in Section 4.4.3. For clarity, we excluded reflectance values from instrument channels located within the deep SWIR water vapor absorption features around 1350 and 1850 $nm$, where the solar radiation is almost entirely absorbed by the atmosphere. Even marginally biased simulations of atmospheric water vapor transmission could

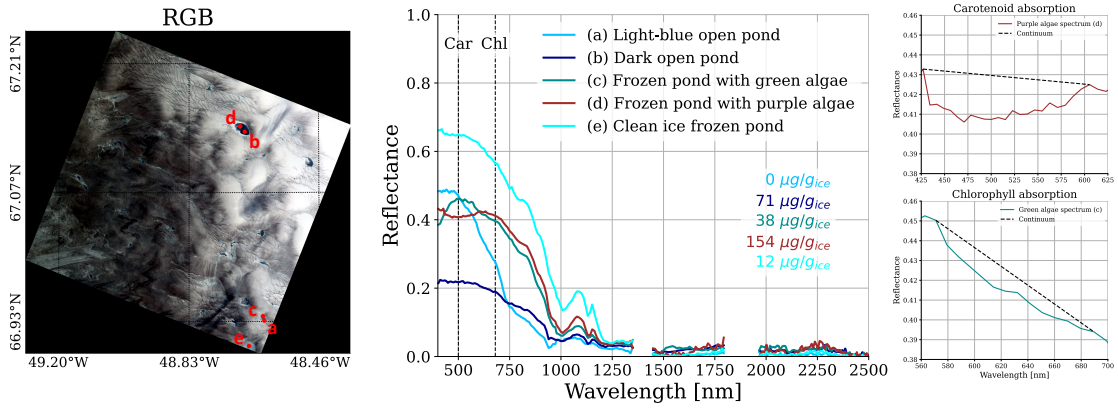


FIGURE 4.5: The middle panel presents examples of retrieved melt pond surface reflectance spectra from the PRISMA image. In addition to the figure legend, estimated mass mixing ratios of glacier algae are displayed in textcolor according to the respective spectrum. Dashed vertical lines indicate the positions of both carotenoid and chlorophyll absorption features at 500 and 680 *nm*, respectively. The left panel shows a true-color RGB with the location of the areas on the map. The right panel zooms in on carotenoid and chlorophyll absorption features between 400 and 700 *nm* present in spectra (c) and (d).

lead to artificially high reflectance values at these wavelengths. Again, we evaluate spectra of clean snow, dark ice, and a melt pond surface. Overall, we see a good agreement with PRISMA L2C spectra. The results from the "lazy Gaussian" inversion feature less spikes and a smoother reflectance gradient especially in the VIS. This emphasizes the capabilities of OE, which enables a less noisy reflectance estimation by incorporating the prior distribution in the surface model (Thompson et al., 2018). However, all spectra show deviations from the PRISMA data in the same spectral ranges as illustrated by the upper panel of Figure 4.4. This confirms the assumptions of the previous Section 4.4.3. On the other hand, further studies are needed to assess the quality of PRISMA L2C spectra and if they can serve as validation targets (Cogliati et al., 2021). Instead, an accurate evaluation of the retrieval results from the "lazy Gaussian" inversion would require field measurements of surface reflectance.

### 4.4.5 Melt ponds

Figure 4.5 shows selected melt pond reflectance spectra representing different water types. Additionally, the estimated glacier algae accumulation for the respective pixels is given in the plot. When comparing with snow or ice surfaces, the reflectance spectrum of melt ponds is characterized by a missing peak at 1100 *nm*. The reflectance beyond 900 *nm* is typically low due to strong liquid water absorption in these wavelengths, with any signal due only to Fresnel reflection (Malinka et al., 2018). Spectra (a) and (b) in Figure 4.5 only show a marginal peak in the NIR

indicating an open pond without ice cover. Shape and magnitude of both spectra conform with field spectrometer measurements of dark and light-blue ponds presented in Malinka et al. (2018). However, while the inversion reports no present algae accumulation for spectrum (a), the estimated mass mixing ratio of 71 $\mu g/g_{ice}$ is comparatively high for spectrum (b). Here, we most likely observe the influence of cryoconite on the bottom of the pond, which has been interspersed with melt water.

In contrast, spectra (c) and (d) exhibit absorption features in the VIS spectral region caused by abundance of biological impurities on the surface. This assumption is confirmed by retrieved glacier algae mass mixing ratios of 38 and 154 $\mu g/g_{ice}$, respectively. Even a distinction between different species of algae is enabled by the retrieval result since both spectra hold different characteristic absorption features. The right panel of Figure 4.5 presents a closer look at carotenoid and chlorophyll absorption between 400 and 700 $nm$ present in spectra (c) and (d). We observe a mixture of phycoerythrin and chlorophyll absorption around 620 $nm$ in spectrum (c) (Bryant, 1982), pointing to green algae or blue colored cyanobacteria, which are commonly found on the Greenland Ice Sheet (Wientjes et al., 2011; Yallop et al., 2012; Gray et al., 2020; Di Mauro et al., 2020). In contrast, spectrum (d) can be distinguished by a broad carotenoid feature around 500 $nm$ indicating the presence of red or purple algae (Hoham and Remias, 2020). They are found in large quantities on the Greenland Ice Sheet (Cook et al., 2020), which is underlined by the relatively high retrieved concentration of 154 $\mu g/g_{ice}$. Present reflectance peaks at 1100 $nm$ in spectra (c) and (d) suggest though that the respective ponds seem to be either partly covered with ice or to consist of a mixture of water and ice grains (Malinka et al., 2018). This is further endorsed since both spectra (c) and (d) resemble the shape of spectrum (e), which is retrieved from a frozen pond featuring almost clean ice without significant algae accumulation.

Overall, the results demonstrate that the "lazy Gaussian" inversion is able to report meaningful results from PRISMA data for glacial melt ponds by quantifying different brightness of water surfaces, distinguishing turbid and clear water as well as identifying potential ice cover. Furthermore, we show that even weak chlorophyll absorption can be resolved by PRISMA data. To our knowledge, this is the first time that this small absorption is observed from a spaceborne imaging spectrometer, which opens a valuable perspective for the life detection on snow and ice using imaging spectroscopy data.

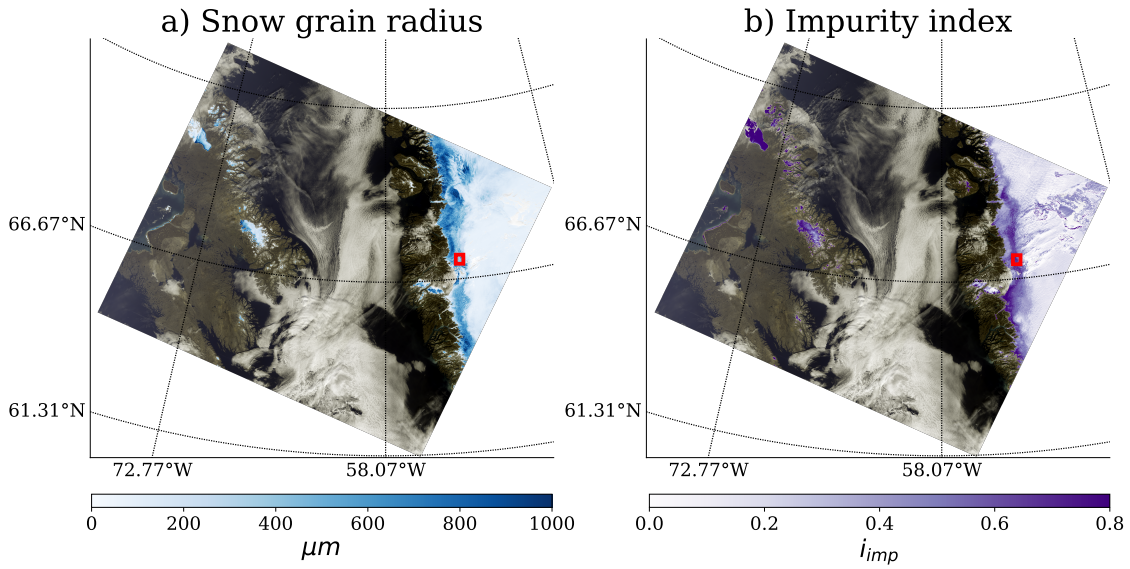


FIGURE 4.6: Resulting maps from the S3 OLCI snow properties retrieval for the western Greenland dataset (acquisition date: August 30, 2020, 15:00 GMT-2). a) Snow grain radius; and b) impurity index. For non-snow covered pixels, the true-color image is displayed. Red boxes indicate the location of the PRISMA acquisition analyzed in this study.

### 4.4.6 Comparison with Sentinel-3 OLCI

Finally, we present results from the S3 OLCI snow properties retrieval and show a comparison with the PRISMA retrieval maps. In particular, we demonstrate the potential of snow and ice surface parameters derived from imaging spectrometers to develop regression models for multispectral data.

Figure 4.6 shows S3 OLCI snow grain radius and impurity index calculated according to Equations 4.5 and 4.7, respectively. It is important to note that the OLCI grain size algorithm assumes a spherical grain shape, so that the retrieval rather reports radii of snow grains than dimensions of arbitrarily shaped ice crystals (Kokhanovsky et al., 2019). We masked out non-snow covered pixels to save processing time and complemented the plot with a true-color image of the S3 acquisition. When looking at the eastern part of the scene, we observe a distinct spatial pattern of both parameters having the largest values towards the edge of the ice sheet in a stripe parallel to the coastline. Moving landwards, snow grain radius and impurity index significantly decline. Both their value range and spatial distribution coincide with reported values in, e.g., Kokhanovsky et al. (2019) or Wang et al. (2020), and are in line with the seasonal conditions to be found at the end of the melting season in late August (Alexander et al., 2014).

As a next step, we generated spatial subsets from the S3 OLCI retrieval maps to match the geographic extent of the PRISMA acquisition. Figure 4.7 shows a visual

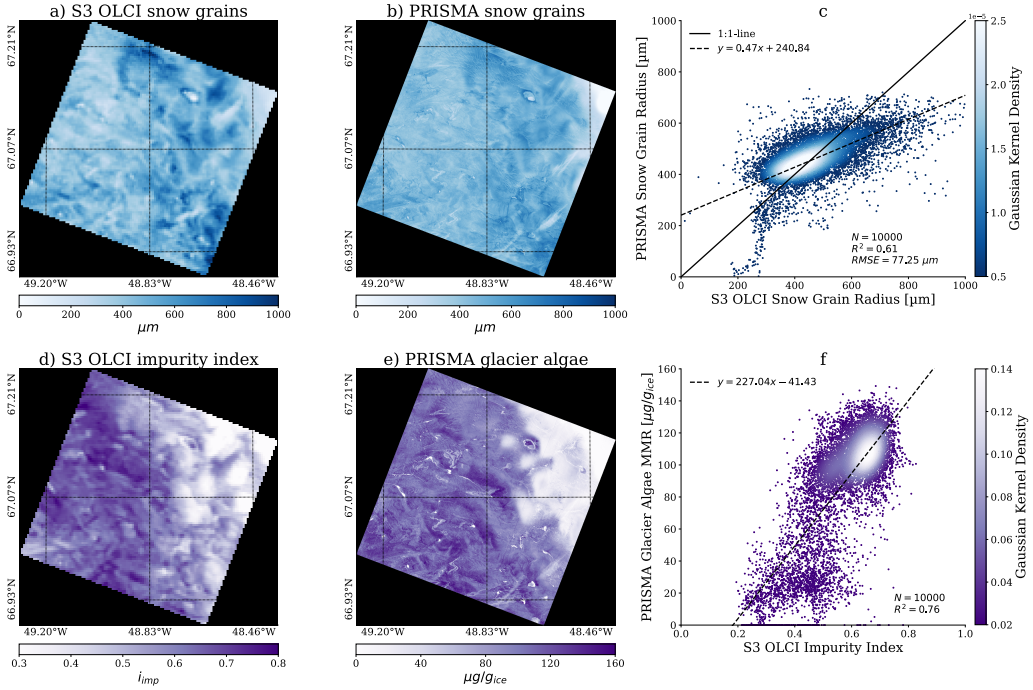


FIGURE 4.7: Visual comparison of PRISMA snow grain radius and glacier algae mass mixing ratio retrieval maps with the spatially equal subsets from the S3 OLCI results. a) Subset of the S3 OLCI snow grain radius map (GSD: 300 $m$); b) PRISMA snow grain radius map (GSD: 30 $m$); d) subset of the S3 OLCI impurity index map (GSD: 300 $m$); and e) PRISMA glacier algae mass mixing ratio map (GSD: 30 $m$). The right panel shows scatter plots for the results shown in a-b and d-e. c) Snow grain radius; and f) impurity index vs. glacier algae mass mixing ratio. To enable a per pixel comparison, the PRISMA surface parameter maps were resampled to 300 $m$ GSD by calculating mean values of $10 \times 10$ pixel aggregates.

comparison of retrieved snow grain radius from both instruments as well as the S3 impurity index and estimated PRISMA glacier algae concentration. First of all, the maps derived from PRISMA data reveal finer spatial structures and patterns on the surface due to the much smaller GSD. Nevertheless, both distribution and value range of snow grain radius are very similar. We observe a broader stripe of larger radii of up to 1000 $\mu m$ extending from North to South in the eastern part of the image and a distinct decrease towards the most north-eastern corner with values of around 200 $\mu m$. The impurity index likewise follows the spatial distribution of retrieved glacier algae accumulation. However, the PRISMA glacier algae map yields a clearer distinction of high algae accumulation spots, which is especially demonstrated by the patterns in the middle of the image with mass mixing ratios of up to 160 $\mu g/g_{ice}$, and the large melt pond towards the North showing algae concentration both on the water surface and at the shoreline. It is important to note that the impurity index is not only sensitive to biological impurities but also to inorganic LAP such as mineral dust, black carbon, and cryoconite (Dumont et al.,

2014; Di Mauro et al., 2017; Wang et al., 2020). Consequentially, deposits of these particles on the ice surface might influence the value of $i_{imp}$, and thus, explain a part of the variability in the comparison.

We assess the before-mentioned spatial correlation of S3 and PRISMA snow grain radius as well as impurity index and algae concentration by showing scatter plots in Figure 4.7c and f. To enable a per pixel comparison, we resampled the PRISMA surface parameter maps to 300 $m$ GSD by taking the mean values of $10 \times 10$ pixel aggregates. Estimated snow grain radii show a remarkable consistency. While we achieve an $R^2$ of 0.61 and an RMSE of 77.25 $\mu m$, the values retrieved from multispectral S3 data spread over a larger range reaching 1000 $\mu m$. In contrast, the estimated grain radii for the most north-eastern part of the image are much smaller when applying our proposed approach to the PRISMA data. Here, we observe values even lower than 200 $\mu m$. The impurity index seems to be less correlated with glacier algae mass mixing ratio, although featuring an $R^2$ of 0.76. It is obvious that most of the correlation is influenced by two clusters in the scatter plot, one at $i_{imp}$ around $0.6 - 0.7$ and mass mixing ratios of $100 - 140$ $\mu g/g_{ice}$, and another at concentrations below 40 $\mu g/g_{ice}$ with corresponding $i_{imp}$ of $0.2 - 0.5$. When only considering high glacier algae mass mixing ratio, the impurity index does not significantly increase and remains almost constant at values of around 0.7. This is an indicator that $i_{imp}$ is in fact able to detect algae accumulation on the ice surface, but is less appropriate for describing fine-scale variations of higher amounts of concentration (Wang et al., 2020). Finally, the scattering of points in both plots may also be due to a geometric mismatch, so that a correction for geolocation of the PRISMA image may improve the regression. However, our results demonstrate sufficient potential of the correlation between impurity index and glacier algae mass mixing ratio derived from PRISMA spectra to build predictors for S3 OLCI data.

Figure 4.8 presents predicted glacier algae concentrations for the S3 OLCI acquisition using two different regression methods. First, we applied the linear regression derived from Figure 4.7f, $y = 227.04x - 41.43$, to each pixel of the S3 OLCI image. Then, we fit a Gaussian process regressor (GPR) with a constant kernel to the data from the subset and predicted the glacier algae mass mixing ratios for the complete dataset. We selected these two regression approaches as examples for both a simple and a more complex method in order to show the manifold choice of well performing algorithms in the field of supervised learning. Figures 4.8c and d illustrate the performance of both regressors when applied to the S3 OLCI subset covering the same extent as the PRISMA image. We observe almost identical $R^2$ values of 0.76 and 0.75, respectively, with a larger RMSE of 36.12 $\mu g/g_{ice}$ though

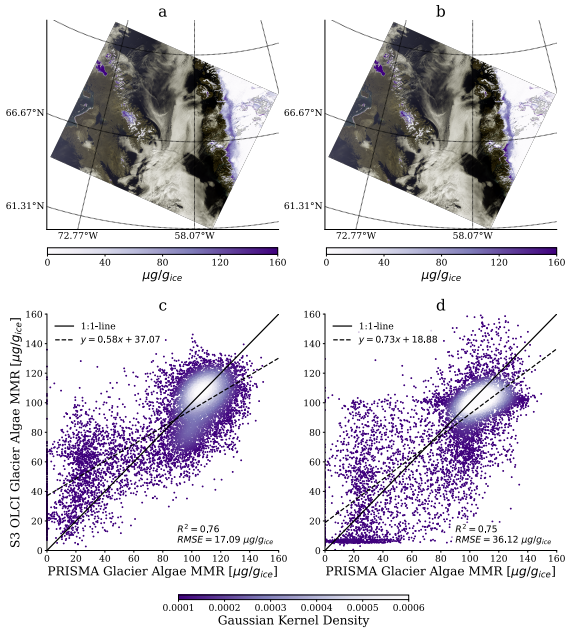


FIGURE 4.8: a-b) Predicted glacier algae mass mixing ratio maps for the S3 OLCI dataset; and c-d) scatter plots from the comparison of predicted glacier algae mass mixing ratio for the S3 OLCI subset and the resampled PRISMA map. The left panel shows results for a simple linear regression. The right panel illustrates the performance of a more complex Gaussian process regression.

for the GPR. Furthermore, the Gaussian kernel densities suggest that a larger fraction of the values predicted by the linear regression is located on the 1 : 1-line. The respective prediction maps in Figures 4.8a and b indicate that both methods are able to locate the dark zone of high glacier algae accumulation at the edge of the ice shield. However, the linear regression leads to smoother transitions towards lower concentrations, whereas the GPR can better reproduce high amounts of algae on the surface. Nevertheless, for GPR prediction quality, learning the kernel is critically important, and the results could be improved by a detailed investigation and a careful selection of the covariance function and the optimizer of the kernel parameters (Rasmussen and Williams, 2006).

Overall, our results provide a promising basis for future exploitation of spectroscopic retrievals to be used as predictors for multispectral data. Different instrument revisit times and the possibility to use imaging spectroscopy data for re-calibration purposes of multiband sensors are other potential synergies. However, a detailed analysis of uncertainty quantification would require concurrent field measurements for a validation of estimated quantities of ice surface parameters.

### 4.4.7 Scaling to a global cryosphere product

With the setup presented in this study, the "lazy Gaussian" inversion can appropriately be applied to snow and ice surfaces without significant topographic characteristics under sufficient illumination conditions, i.e., solar zenith angles not significantly exceeding $50 - 60°$ (Bohn et al., 2021). This holds true for many parts of the Greenland Ice Sheet during summertime. However, forthcoming orbital imaging spectroscopy missions will deliver high-resolution data both on a global scale and daily basis, which requests for independently applicable retrieval algorithms (Cawse-Nicholson et al., 2021). Especially the SBG designated observable and ESA's CHIME mission are expected to record large data volumes covering a wide range of different snow and ice surface conditions spanning over almost all latitudes.

The results from PRISMA data demonstrate that our approach for mapping snow and ice surface properties has the potential for providing a robust cryosphere product based on orbital imaging spectroscopy. However, the method still faces some challenges that need to be confronted prior to a global application. So far, the inversion uses simulations of spectral albedo by a two-stream snow and ice RTM as prior knowledge, which does not account for directional effects in the reflectance. Likewise, geometric characteristics of the surface such as slope, aspect, sky view factor, or shadow fraction are not considered in the forward model. In order to achieve accurate retrieval results over mountainous areas with complex terrain as well as varying illumination and observation geometries, simulations of directional reflectance based on multi-stream RTMs such as DISORT have to be considered as prior knowledge (Lamare et al., 2020). Furthermore, Equation 4.2 needs to be extended by some additional terms accounting for surface topography. However, by applying an OE-based simultaneous atmosphere and surface inversion scheme our approach provides the basis for a straightforward implementation of these requirements. This will enable a global mapping of snow and ice surface properties corrected for latitudinal and topographic biases including a rigorous quantification of uncertainties.

## 4.5 Conclusion

We present first results from the recently introduced "lazy Gaussian" inversion to infer glacier ice surface properties from a PRISMA imaging spectroscopy dataset acquired over the Greenland Ice Sheet. It is the first time that PRISMA data are used for studying the cryosphere and it serves as a finger board to the global availability of spaceborne imaging spectroscopy data, which will allow to detect and quantify

snow and ice variables with unprecedented accuracy. The algorithm maps grain radius, liquid water path length, and algae mass mixing ratio, and reports associated posterior predictive uncertainties. Additionally, we show a comparison with multispectral data from the S3 OLCI instrument to detect potential synergies and to reveal how these data can be complimented by satellite spectroscopy observations.

Our results demonstrate that spectroscopic observations from space will play a crucial rule in upcoming research of the Greenland Ice Sheet. We show that these data can be used to detect and quantify patterns of LAP accumulated on the surface in areas such as the dark zone or k-transect. Maps of algae accumulation, surface liquid water, and melt pond evolution provided on a regular basis can support the ongoing investigations of ice sheet melt processes and the resulting sea level rise.

Furthermore, we evidence that glacier algae maps derived from the PRISMA imaging spectrometer can be used to predict the same surface parameter from simple band indices such as the impurity index. This opens new possibilities of producing multi-year time series of glacier algae mapping on the Greenland Ice Sheet based on multispectral datasets acquired by instruments such as Landsat or Sentinel-2 and 3. High-frequency observations may not be possible even from the next generation of imaging spectrometers due to their global charter and the high fraction of cloud cover over the Arctic. In contrast, multiband sensors like Sentinel-3 have far greater temporal coverage, but lack imaging spectrometer's sensitivity to subtler snow and ice parameters. Under such circumstances, a hybrid approach can capture the best of both, with sparse imaging spectroscopy data being used to build local models for a more complete interpretation of the multiband data. At the same time, this can fill the gap of missing spectroscopic observations from space during the past four decades. A multitude of upcoming missions such as EnMAP, EMIT, CHIME, and SBG will lead to an unprecedented availability of high-resolution data both on a global scale and daily basis, and thus, improve our understanding of snow and ice surface processes and facilitate the monitoring of glacier ice changes over time.

## Acknowledgments

This work has been done in the frame of EnMAP, which is funded under the DLR Space Administration with resources from the German Federal Ministry of Economic Affairs and Energy (grant No. 50 EE 0850) and contributions from DLR, GFZ and OHB System AG. A portion of this research took place at the Jet Propulsion Laboratory, California Institute of Technology, under a contract with the National Aeronautics and Space Administration (80NM0018D0004). US Government Support Acknowledged.

# Chapter 5

# Synthesis

The main objective of this thesis is to assess the contributions from a new generation of spaceborne imaging spectroscopy missions to further the detection and quantification of the three phases of water on Earth's surface by introducing novel joint retrieval methods. In particular, these methods are investigated for their potential of providing a robust global product independent from latitudinal and topographic characteristics and delivering rigorous uncertainty quantification. Section 5.1 of this final chapter summarizes the main outcomes of the consecutive self-contained manuscripts in Chapters 2 - 4 with respect to the main research questions formulated in Chapter 1. Ultimately, Section 5.2 provides an outlook to future research perspectives and recommendations.

## 5.1 Conclusions

This section addresses the key results from Chapters 2 - 4 by presenting their particular contributions to answering the main research questions of this thesis.

**(1) Are present and forthcoming orbital imaging spectroscopy missions applicable to robustly map and quantify the three phases of water?**

Chapters 2 and 3 assessed the accuracy of retrieved vegetation liquid water content and snow and ice properties and evaluated the decoupling of atmosphere and surface state within two novel joint inversion schemes for spaceborne imaging spectroscopy data. Below, the main outcomes of these analyses are summarized, each followed by a more detailed elaboration:

- Spaceborne imaging spectroscopy permits improved atmospheric water vapor estimations by a removal of perturbing influences from overlapping surface liquid water and ice absorption.

The sensitivity analysis of the coupled retrieval of the three phases of water in Chapter 2 reveals that estimations of atmospheric water vapor are less biased compared with results from traditional band ratio approaches. This is in accordance with results from previous studies that used AVIRIS data as a pathfinder for future spaceborne instruments (Green et al., 2006; Thompson et al., 2015). Furthermore, the investigation of retrieval error correlation matrices indicates a distinct separation of atmosphere and surface state during the inversion, which not only facilitates a quantification of the three phases of water, but also improves the results of atmospheric correction procedures especially over liquid and solid water enriched surfaces such as vegetation and snow. The proposed joint atmosphere and surface inversion in Chapter 3 confirms this strict decoupling of atmospheric water vapor from influences induced by background surface reflectance.

- The accuracy of estimated vegetation liquid water content strongly depends on plant species as well as on the physical processes considered in the surface model.

Chapter 2 demonstrates the general robustness of the coupled retrieval of the three phases of water in terms of estimating vegetation canopy water content. However, the results show that an accurate quantification requires the consideration of both scattering and absorption processes on the surface, e.g., in leaves of vegetation or the superior canopy. The coupled retrieval incorporates a surface model based on the Beer-Lambert law that only accounts for absorption without respecting multiple volume scattering effects. Neglecting these effects leads to a systematic overestimation of canopy water content. Similar studies determined a constant factor representing this overestimation, which was then used to calibrate the retrieval results (see, e.g., Wocher et al. (2018)). However, the results from Chapter 2 clearly outline that the magnitude of overestimation depends on the native structure of plant species, most importantly population height and LAI, so that a global application of such calibration is not accurate. In fact, considering multiple scattering events in the surface model might be the more appropriate way to achieve improvements in retrieval accuracy. A promising approach is demonstrated in Chapter 3. The local prior spectral library of snow and ice reflectance could straightforwardly be replaced by simulations of canopy reflectance obtained from a 3D canopy RTM such as HySimCaR (Kuester et al., 2014). This would automatically introduce information about the type of vegetation and the structure of the canopy and thus, facilitate a more accurate retrieval of vegetation biophysical variables including liquid water content.

- Spaceborne imaging spectroscopy can provide accurate retrieval maps of snow and ice grain size, surface liquid water content, as well as biological LAP accumulation.

The coupled retrieval of the three phases of water demonstrates the ability to clearly distinguish between different quantities of ice on the surface. Furthermore, the method enables a discrimination between dry and wet snow and tracks high amounts clearly better than empirical indices, such as the NDSI. This concept is then advanced to the joint atmosphere and surface inversion as presented in Chapter 3, which provides an even more accurate quantification of snow and ice properties. In particular, the ability to incorporate different surface models as prior knowledge enables a separation between snow and ice grains based on their optical properties, as well as an additional retrieval of LAP accumulation on the surface. Moreover, this novel OE-based retrieval scheme yields a direct interpretation of snow and ice retrieval uncertainties and their intercorrelation with the atmospheric state. For instance, it is for the first time demonstrated that errors in the retrieval of atmospheric AOT can significantly bias the estimation of ice crystal dimensions on the surface.

- The joint atmosphere and surface inversion serves as a prototype for a globally applicable algorithm to estimate the three phases of water from orbital imaging spectroscopy missions including a rigorous propagation and quantification of retrieval uncertainties.

The results from Chapters 3 and 4 demonstrate the eligibility of the joint atmosphere and surface inversion to serve as a basis for providing robust global products and associated uncertainties. The OE-based inversion scheme permits a novel rigorous propagation of uncertainties caused by instrument noise, unknown model parameters, and prior knowledge, through the retrieval chain up to a quantification of final level 3 product uncertainties. This leverages the interpretation of surface property mapping as shown in previous studies, for instance, on the example of minerals (Carmon et al., 2020). But also the analyses of posterior predicted distribution of covariances presented in this thesis confirm the ability of OE to associate rigorous uncertainties with the estimated three phases of water. In particular, it enables a detailed investigation of posterior error correlation between atmospheric and surface state parameters.

However, a robust global mapping of vegetation liquid water content as well as snow and ice surface properties is critically contingent on a precise incorporation of solar and observation geometry in the retrieval scheme. Biased assumptions of the

instrument viewing angles have the most significant negative effects on the retrieval of vegetation liquid water content along with LAI (Asner and Martin, 2008). The solar zenith angle strongly affects the reflectivity of snow and ice surfaces. Especially sun angles beyond 50° lead to remarkably increased directional effects in the snow and ice reflectance (Painter and Dozier, 2004b; Painter and Dozier, 2004a). The sensitivity analysis of Chapter 3 has attested retrieval errors of snow grain radius within several orders of magnitude if directional effects are neglected in the prior knowledge. To avoid increasing uncertainties due to acquisition geometries, an incorporation of appropriate prior knowledge in the OE inversion scheme will be necessary. This could be accomplished by relying on respective reflectance simulations under changing illumination and observation conditions as prior spectral library.

Although featuring high-resolution footprints of 30 $m$, the issue of mixed pixels is still of importance for forthcoming orbital imaging spectroscopy observations. An accurate retrieval of surface liquid water as well as snow and ice properties is impeded if significant background reflectance properties featuring absorption in a similar wavelength region but due to different materials influence the measured signal. A descriptive example is the underlying soil of vegetation, which becomes imposed if the fractional cover falls below a value of 1. If present, ferruginous minerals such as hematite or goethite virtually increase water absorption by having broad iron features superimposing NIR water bands (Carmon et al., 2020). But also sulfate minerals such as gypsum show small absorption around the 940 and 1140 $nm$ water bands, so that retrievals could be biased (Milewski et al., 2019). This also accounts for snow and ice surfaces in cases of low snow fractional cover. However, on condition that this fractional cover is known, the approaches to simultaneously optimize for all three phases of water presented in this thesis would significantly improve retrievals for mixed pixels.

Finally, the joint atmosphere and surface inversion as presented in Chapter 4 can appropriately be applied to surfaces without significant topographic characteristics, i.e., assuming a flat and horizontal orientation. While this holds true for, e. g., many parts of the Greenland Ice Sheet, a multitude of observation targets is located in mountainous areas with rugged terrain. The consideration of topographic features, such as surface slope and aspect, sky view factor, or shadow fraction, in the retrieval algorithm is therefore crucial for achieving accurate estimations of surface properties. Although such effects are not yet considered in the forward model, the OE-based inversion scheme provides the basis for a straightforward implementation of these requirements.

**(2) How can spaceborne imaging spectroscopy contribute to the analyses of vegetation dynamics and ice melt processes and their link to climate change?**

A quantitative mapping of water in its three states on a global scale is crucial as it helps to assess physical and biological processes both in Earth's atmosphere and on its surface. In particular, the role of vegetation as well as snow and ice surfaces in climate change can be better evaluated by integrating knowledge obtained from high-resolution optical remote sensing from space into climate models. The independent studies in Chapters 2 - 4 lead to the following main conclusions that are outlined in more detail hereinafter:

- By tracking changes in vegetation liquid water content more reliable than empirical band indices, spaceborne imaging spectroscopy facilitates a prediction of drought stress and wildfire potential in the context of climate change.

Vegetation that is exposed to excessive heat and aridity develops indications of water stress including wilting or loss of leaves. However, the actual water content decreases comparatively slowly. Hunt, Ustin, and Riano (2013) stated that measurements are required to detect differences of only 0.02 $gcm^{-2}$ in relative water content in order to show evidence of drought stress on leaf level. The commonly applied upscaling method to canopy level of multiplying by the LAI leads to increasing differences, making spaceborne observations an ideal tool to detect plant water stress. However, the sensitivity analysis in Chapter 2 demonstrates that such small differences in canopy water content are hardly detectable by empirical band indices. Even traditional indices such as the normalized difference vegetation index (NDVI) have only limited capabilities to detect drought stress since the decrease in water content starts prior to a reduction in LAI (Hunt, Ustin, and Riano, 2013). In contrast, the coupled retrieval of the three phases of water leads to much subtler differentiation of quantitative values, pointing to the significant potential of spaceborne imaging spectroscopy to early detect droughts and the associated wildfire risk. In fact, the sensitivity of vegetation liquid water content to drought stress is too low for being distinguishable by spectroscopic measurements from a single date (Serrano et al., 2000; Hunt, Ustin, and Riano, 2013), but the expected data availability on a daily basis delivered by forthcoming orbital imaging spectroscopy missions will enable reliable estimates of changes in vegetation water content and consequentially, provide useful drought predictions. This will lead to important data records for assessing the impacts of climate change on agricultural and ecological processes.

- Imaging spectroscopy observations from space will significantly contribute to the understanding of biophysical processes on Earth's Ice Sheets by revealing the positive climate feedback between surface liquid water content and algae accumulation.

The sensitivity analysis in Chapter 3 shows that the information content of imaging spectroscopy measurements is almost independent from the occurrence of biological LAP in-between the ice crystals. This is a promising basis for using such observations to enhance the understanding of algal blooms on snow and ice surfaces. Estimated glacier algae concentration from both airborne AVIRIS-NG and spaceborne PRISMA acquisitions, as presented in Chapters 3 and 4, revealed a distinct accordance with field measurements in terms of value range and spatial distribution. In particular, the results confirmed a remarkable correlation between the amount of available liquid water on the surface and the blooms of glacier algae. This supports the theory of the positive algae-liquid water climate feedback as described in previous studies (Williamson et al., 2018; Dial, Ganey, and Skiles, 2018). A major consequence of this interaction is an increased melting of the Ice Sheets, which in turn significantly contributes to global sea level rise in the context of ongoing climate change (Benning et al., 2014; Bamber et al., 2018). Hence, quantitative maps of surface liquid water and glacier algae accumulation derived from spaceborne imaging spectroscopy on a daily basis will be an important input to surface process and climate models.

**(3) What are the synergies between imaging spectroscopy from space and observations from existing multiband orbital instruments?**

Forthcoming spaceborne imaging spectroscopy missions, such as SBG and CHIME, will provide a comprehensive global monitoring of Earth's surface. Generally, a complementation with multispectral or medium resolution instruments, such as Landsat and Sentinel-2 or 3, will facilitate the mapping of climate change related biophysical variables. The resulting lower spectral resolution is then balanced by a high temporal revisit (Cawse-Nicholson et al., 2021). Synergistic approaches to existing Earth observation missions are expected to contribute new aspects of science to climate research (Malenovský et al., 2012; Cawse-Nicholson et al., 2021).

In particular, snow and ice conditions can change on rapid timescales, and regular observations are critical to infer the rate at which accumulation, LAP deposition, and melt processes occur. A recent report by the National Academy of Sciences called for snow albedo observations on a weekly basis to constrain changes in the water and energy cycles (National Academies of Sciences, Engineering, and

Medicine, 2018). Such dense observations may not be possible even from the next generation of imaging spectrometers due to their global charter and the high fraction of cloud cover over the Arctic. In contrast, multiband sensors like Sentinel-2 or 3 have far greater temporal coverage, but lack imaging spectrometer's sensitivity to subtler snow and ice parameters. Under such circumstances, a hybrid approach can capture the best of both, with sparse imaging spectroscopy data being used to build local models for a more complete interpretation of the multiband data. Chapter 4 demonstrates for the first time how measurements derived from the new era of spaceborne imaging spectrometers can be used in concert with multiband data in a comprehensive cryosphere observation system. The results show that simple local regression models applied to moderate resolution optical remote sensing data can achieve a high degree of alignment with the spectroscopic measurements over snow and ice surfaces. Including such a temporal component in the prior knowledge of the spectroscopic retrieval scheme could further improve the algorithm performance as it would capture both short- and long-time variations in alternating melt and freezing events.

In the same way, regular observations of vegetation on a daily basis using orbital imaging spectroscopy will provide large data volumes of quantitatively estimated biophysical surface parameters including canopy liquid water content. These can complement long-term time series of empirical band indices, such as NDWI or NDVI, obtained from multiband and medium resolution measurements in order to transform spectral band ratios into accurate physical quantities.

## 5.2 Outlook

Given the short time period since the new generation of orbital imaging spectrometers has been heralded by the launch of DESIS and PRISMA, the wealth of retrieval algorithms already available for application in different scientific disciplines is compelling. This has mainly been facilitated by long-term mission planning and comprehensive precursor studies based on airborne technologies, such as NASA's AVIRIS instruments. These studies also pioneered several approaches for the detection and quantification of the three phases of water with imaging spectroscopy (Gao and Goetz, 1990; Roberts, Green, and Adams, 1997; Nolin and Dozier, 2000; Green et al., 2002; Green et al., 2006; Painter et al., 2013; Thompson et al., 2018). Based on that, this thesis introduces two novel methods of joint atmosphere and surface inversions that are tailored to the application to the new era of spectroscopic measurements from space. However, several limitations need to be addressed in further improving retrieval algorithms, paving the way for their independent applicability

as requested in Cawse-Nicholson et al. (2021). In this context, the following aspects are of particular relevance:

1. Future global retrieval algorithms must include a consideration of topographic characteristics, such as surface slope and aspect as well as sky view factor and shadow fraction.

2. Directional effects, particularly in snow and ice reflectance, depending on illumination and observation conditions must be integrated as prior knowledge in future OE retrieval schemes.

3. Improved retrieval algorithms must account for mixed pixels by determining influences from background reflectance and fractional cover.

4. Both absorption and scattering processes must be rigorously treated by future surface models in order to increase the accuracy of retrieved vegetation liquid water content.

5. A comprehensive ground-based validation is needed for a proper characterization of uncertainties in estimated atmosphere and surface state parameters and to interpret OE-retrieved posterior error measures.

6. Strategies to handle terabytes of data volume expected from upcoming satellite imaging spectroscopy missions need to be integrated in improved retrieval algorithms, including processing efficiency and storage of data output.

While the joint atmosphere and surface inversion presented in Chapter 4 can appropriately be applied to flat and horizontal surfaces, extensions to the forward model accounting for topographic characteristics, such as introduced in Carmon et al. (2021), are crucial for a global application (point 1). Just as importantly, future OE retrieval schemes should rely on simulations of directional reflectance instead of spectral albedo as prior knowledge, using multistream radiative transfer models, such as DISORT (Painter and Dozier, 2004b; Lamare et al., 2020) (point 2). Point 3 could be addressed by incorporating algorithms to calculate fractional cover similar to the MEMSCAG (Multiple EndMember Snow-Covered Area and Grain size) model (Roberts et al., 1998b; Painter et al., 2003). The retrieval of vegetation liquid water content requests for a consideration of both absorption and multiple scattering processes, which could be accomplished by reverting to prior knowledge obtained from 3D canopy reflectance models, such as HySimCaR (Kuester et al., 2014) (point 4). The entire suite of retrieval algorithms also necessitates more frequent efforts of ground-based validation, particularly from remote areas of the

Earth, such as the Greenland Ice Sheet (point 5). Finally, strategies to improve processing efficiency of retrieval algorithms have been initialized, but still need to be implemented for operational use (point 6). They include the training of local linear emulators assuming spatial continuity of atmospheric fields (Thompson et al., 2021), or the design of high-performance Bayesian inversions speeding up the traditional OE scheme by about two orders of magnitude (Susiluoto et al., 2021). To reduce memory demand of algorithm output, approaches to decompose large retrieval uncertainty matrices into a few principal components are also under consideration. In summary, retrieval algorithms for spaceborne imaging spectroscopy of the three phases of water still need to experience extensive future research.

Nevertheless, optical remote sensing of Earth's surface from space will be advanced to an unprecedented level in the near future in terms of both data availability and quality. Complementing already existing multispectral and medium resolution instruments, upcoming launches of several imaging spectroscopy missions including EMIT, EnMAP, CHIME, and SBG, open new perspectives in regularly monitoring and mapping atmosphere and surface properties including the three phases of water on a global scale. As demonstrated in this thesis, these maps will provide a valuable input to the modeling of biological and physical processes that help to better understand climate change and to predict and adapt to its socioeconomic consequences.

# List of Abbreviations

| | |
|---|---|
| AERONET | Aerosol Robotic Network |
| AOT | aerosol optical thickness |
| APDA | atmospheric precorrected differential absorption technique |
| ASD | Analytical Spectral Device |
| ASI | Italian Space Agency |
| ASO | Airborne Snow Observatory |
| ATREM | Atmospheric Removal algorithm |
| AVHRR | Advanced Very High Resolution Radiometer |
| AVIRIS | Airborne Visible Infrared Imaging Spectrometer |
| AVIRIS-C | AVIRIS-Classic |
| AVIRIS-NG | AVIRIS-Next generation |
| | |
| BC | black carbon |
| BioSNICAR-GO | Bio-optical Snow, Ice, and Aerosol Radiation - Geometric Optics model |
| BOA | bottom-of-atmosphere |
| | |
| CHIME | Copernicus Hyperspectral Imaging Mission |
| CHRIS-PROBA | Compact High Resolution Imaging Spectrometer - Project for On-Board Autonomy |
| CIBR | continuum interpolated band ratio |
| CWC | canopy water content |
| CWV | columnar water vapor |
| | |
| DESIS | DLR Earth Sensing Imaging Spectrometer |
| DISORT | Discrete Ordinates Radiative Transfer Program |
| DLR | German Aerospace Center |
| DOF | degree of freedom |
| DRAT | Advanced Radiometric Ray Tracer |
| DWI | depth water index |
| | |
| EeteS | EnMAP end-to-end Simulation tool |

| | |
|---|---|
| EMIT | Earth Surface Mineral Dust Source Investigation |
| EnMAP | Environmental Mapping and Analysis Program |
| EO | Earth observation |
| ER-2 | Earth Resources 2 |
| ESA | European Space Agency |
| fCover | fractional cover |
| GMT | Greenwich Mean Time |
| GO | Geometric Optics |
| GOME-2 | Global Ozone Monitoring Experiment 2 |
| GOSAT | Greenhouse Gases Observing Satellite |
| GPR | Gaussian process regression |
| GSD | ground sampling distance |
| GFZ | German Research Centre for Geosciences |
| HCRF | hemispherical conical reflectance factor |
| HDRF | hemispherical directional reflectance factor |
| HITRAN | High-resolution Transmission Molecular Absorption Database |
| HSF | surface elevation |
| HyMap | Hyperspectral Mapper |
| HySimCaR | Hyperspectral Simulation of Canopy Reflectance system |
| IR | infrared |
| ISOFIT | Imaging Spectrometer Optimal Fitting |
| LAI | leaf area index |
| LAP | light-absorbing particles |
| LUT | look-up-table |
| LWC | leaf water content |
| MCRT | Monte Carlo Ray Tracing |
| MEMSCAG | Multiple EndMember Snow-Covered Area and Grain Size model |
| MERIS | Medium Resolution Imaging Spectrometer |
| MODIS | Moderate Resolution Imaging Spectroradiometer |
| MODTRAN | Moderate Resolution Atmospheric Transmission |

| | |
|---|---|
| NASA | National Aeronautics and Space Administration |
| NDSI | normalized difference snow index |
| NDVI | normalized difference vegetation index |
| NDWI | normalized difference water index |
| NIR | near-infrared |
| NIRv | NIR reflectance of vegetation |
| NOAA | National Oceanic and Atmospheric Administration |
| OE | Optimal Estimation |
| OLCI | Ocean and Land Colour Instrument |
| OMI | Ozone Monitoring Instrument |
| PRISMA | Hyperspectral Precursor of the Application Mission |
| PROSAIL | PROSPECT and SAIL radiative transfer model |
| RAA | relative azimuth angle |
| RAMI | Radiation Transfer Model Intercomparison |
| RGB | red-green-blue |
| RMSE | root mean squared error |
| RTM | radiative transfer model |
| SAA | solar azimuth angle |
| SBG | Surface Biology and Geology |
| SCOPE | Soil Canopy Observation, Photochemistry and Energy fluxes radiative transfer model |
| SGSP | snow grain size and pollution amount algorithm |
| SICE | S3 OLCI Snow and Ice Properties Processor |
| SNICAR | Snow, Ice, and Aerosol Radiation model |
| SNR | signal-to-noise ratio |
| SPARC'03 | Spectra Barrax Campaign 2003 |
| SPOT | Satellite Probatoire d'Observation de la Terre |
| SSD | spatial sampling distance |
| SSI | spectral sampling interval |
| SWIR | shortwave-infrared |
| SZA | solar zenith angle |
| TIR | thermal infrared |
| TM | Thematic Mapper |

| | |
|---|---|
| TOA | top-of-atmosphere |
| TOC | top-of-canopy |
| UV | ultraviolet |
| VIS | visible |
| VNIR | visible to near-infrared |
| VZA | view zenith angle |
| WAAI | water absorption area index |

# List of Figures

# List of Tables

# Bibliography

AERONET (2019). *AERONET Aerosol Optical Depth Data Display Interface - Version 3 Aerosol Optical Depth*. https://aeronet.gsfc.nasa.gov/cgi-bin/data_display_aod_v3. Accessed: 05/27/2019.

Albert, P., R. Bennartz, R. Preusker, R. Leinweber, and J. Fischer (2005). "Remote sensing of atmospheric water vapor using the moderate resolution imaging spectroradiometer". In: *J. Atmos. Ocean. Tech.* 22, 309–314. DOI: 10.1175/JTECH1708.1.

Alexander, P. M., M. Tedesco, X. Fettweis, R. S. W. van de Wal, C. J. P. P. Smeets, and M. R. van den Broeke (2014). "Assessing spatiotemporal variability and trends in modelled and measured Greenland Ice Sheet albedo (2000–2013)". In: *Cryosphere* 8, 2293–2312. DOI: 10.5194/tc-8-2293-2014.

Aoki, T., A. Hachikubo, and M. Hori (2003). "Effects of snow physical parameters on shortwave broadband albedos". In: *J. Geophys. Res.* 108.D19. DOI: 10.1029/2003JD003506.

Aoki, T., M. Hori, H. Motoyoshi, T. Tanikawa, A. Hachikubo, K. Sugiura, T. J. Yasunari, R. Storvold, H. A. Eide, K. Stamnes, W. Li, J. Nieke, Y. Nakajima, and F. Takahashi (2007). "ADEOS-II/GLI snow/ice products—Part II: Validation results using GLI and MODIS data". In: *Remote Sens. Environ.* 111, pp. 274–290. DOI: 10.1016/j.rse.2007.02.035.

Arnaud, L., G. Picard, N. Champollion, F. Domine, J. C. Gallet, E. Lefebvre, M. Fily, and J.M. Barnola (2011). "Measurement of vertical profiles of snow specific surface area with a 1 cm resolution using infrared reflectance: instrument description and validation". In: *J. Glaciol.* 57.201, pp. 17–29. DOI: 10.3189/002214311795306664.

Asner, G. P. and R. E. Martin (2008). "Spectral and chemical analysis of tropical forests: scaling from leaf to canopy levels". In: *Remote Sens. Environ.* 112, pp. 3958–3970. DOI: 10.1016/j.rse.2008.07.003.

Bach, H., M. Rast, and J. Nieke (2018). "CHIME - The Copernicus Hyperspectral Imaging Mission". In: *Nationales Forum fuer Fernerkundung und Copernicus 2018 Berlin, 27-29 November 2018*.

Badgley, G., C. B. Field, and J. A. Berry (2017). "Canopy near-infrared reflectance and terrestrial photosynthesis". In: *Sci. Adv.* 3.3. DOI: 10.1126/sciadv.1602244.

Bamber, J., R. M. Westway, B. Marzeion, and B. Wouters (2018). "The land ice contribution to sea level during the satellite era". In: *Environ. Res. Lett.* 13. DOI: 10.1088/1748-9326/aac2f0.

Barducci, A., D. Guzzi, P. Marcoionni, and I. Pippi (2004). "Algorithm for the retrieval of columnar water vapor from hyperspectral remotely sensed data". In: *Appl. Optics* 43.29, pp. 5552–5563. DOI: 10.1364/AO.43.005552.

— (2005). "CHRIS-PROBA performance evaluation: Signal-to-noise ratio, instrument efficiency and data quality from acquisitions over San Rossore (Italy) test site". In: *Proc. of the 3rd ESA CHRIS/Proba Workshop, 21-23 March (ESA SP-593, June 2005)*.

Bennartz, R. and J. Fischer (2001). "Retrieval of columnar water vapour over land from backscattered solar radiation using the Medium Resolution Imaging Spectrometer". In: *Remote Sens. Environ.* 78, pp. 274 –283. DOI: 10.1016/S0034-4257(01)00218-8.

Benning, L. G., A. M. Anesio, S. Lutz, and M. Tranter (2014). "Biological impact on Greenland's albedo". In: *Nat. Geosci.* 7.691. DOI: 10.1038/ngeo2260.

Berk, A., G. P. Anderson, P. K. Acharya, M. L. Hoke, J. H. Chetwynd, L. S. Bernstein, E. P. Shettle, M. W. Matthew, and S. M. Adler-Golden (2003). MODTRAN*4 version 3 revision 1 user's manual*. Tech. rep. Hanscom Air Force Base, MA, USA: Air Force Research Laboratory.

Berk, A., L. S. Bernstein, and D. C. Robertson (1989). MODTRAN*: a moderate resolution model for* LOWTRAN*7*. Tech. rep. GL-TR-89-0122. Hanscom Air Force Base, MA, USA: Air Force Geophysics Laboratory.

Bernstein, L. S., A. Berk, and R. L. Sundberg (2007). *Application of* MODTRAN *to extra-terrestrial planetary atmospheres*. Tech. rep. Burlington, MA, USA: Spectral Sciences, Inc.

Bohn, N., L. Guanter, T. Kuester, R. Preusker, and K. Segl (2020). "Coupled retrieval of the three phases of water from spaceborne imaging spectroscopy measurements". In: *Remote Sens. Environ.* 242. DOI: 10.1016/j.rse.2020.111708.

Bohn, N., T. H. Painter, D. R. Thompson, N. Carmon, J. Susiluoto, M. J. Turmon, M. C. Helmlinger, R. O. Green, J. M. Cook, and L. Guanter (2021). "Optimal estimation of snow and ice surface parameters from imaging spectroscopy measurements". In: *Remote Sens. Environ.* 264. DOI: 10.1016/j.rse.2021.112613.

Born, M. and E. Wolf (1959). *Principles of Optics*. New York, USA: Elsevier, p. 614.

Brandt, R. E., S. G. Warren, and A. D. Clarke (2011). "A controlled snowmaking experiment testing the relation between black carbon content and reduction of snow albedo". In: *J. Geophys. Res.* 116. DOI: 10.1029/2010JD015330.

Bryant, D. A. (1982). "Phycoerythrocyanin and phycoerythrin: Properties and occurrence in cyanobacteria". In: *J. Gen. Microbiol.* 128.4, pp. 835–844. DOI: 10.1099/00221287-128-4-835.

Carlsen, T., G. Birnbaum, A. Ehrlich, J. Freitag, G. Heygster, L. Istomina, S. Kipfstuhl, A. Orsi, M. Schäfer, and M. Wendisch (2017). "Comparison of different methods to retrieve optical-equivalent snow grain size in central Antarctica". In: *Cryosphere* 11, 2727–2741. DOI: 10.5194/tc-11-2727-2017.

Carmon, N., A. Berk, N. Bohn, P. G. Brodrick, H. Nguyen, D. R. Thompson, and M. Turmon (2021). "Unified topographic and atmospheric correction for remote imaging spectroscopy". In: *In prep.*

Carmon, N., D. R. Thompson, N. Bohn, J. Susiluoto, M. Turmon, P. G. Brodrick, D. S. Connelly, A. Braverman, K. Cawse-Nicholson, R. O. Green, and M. Gunson (2020). "Uncertainty quantification for a global imaging spectroscopy surface composition investigation". In: *Remote Sens. Environ.* 251, p. 112038. DOI: 10.1016/j.rse.2020.112038.

Carrere, V. and J. E. Conel (1993). "Recovery of Atmospheric Water Vapor Total Column Abundance from Imaging Spectrometer Data Around 940 nm - Sensitivity Analysis and Application to Airborne Visible/Infrared Imaging Spectrometer (AVIRIS) Data". In: *Remote Sens. Environ.* 44, pp. 179–204. DOI: 10.1016/0034-4257(93)90015-P.

Cawse-Nicholson, K., P. A. Townsend, D. Schimel, A. M. Assiri, P. L. Blake, M. F. Buongiorno, P. Campbell, N. Carmon, K. A. Casey, R. E. Correa-Pabón, K. M. Dahlin, H. Dashti, P. E. Dennison, H. Dierssen, A. Erickson, J. B. Fisher, R. Frouin, C. K. Gatebe, H. Gholizadeh, M. Gierach, N. F. Glenn, J. A. Goodman, D. M. Griffith, L. Guild, C. R. Hakkenberg, E. J. Hochberg, T. R.H. Holmes, C. Hu, G. Hulley K. F. Huemmrich, R. M. Kudela, R. F. Kokaly, C. M. Lee, R. Martin, C. E. Miller, W. J. Moses, F. E. Muller-Karger, J. D. Ortiz, D. B. Otis, N. Pahlevan, T. H. Painter, R. Pavlick, B. Poulter, Y. Qi, V. J. Realmuto, D. Roberts, M. E. Schaepman, F. D. Schneider, F. M. Schwandner, S. P. Serbin, A. N. Shiklomanov, N. Stavros, D. R. Thompson, J. L. Torres-Perez, K. R. Turpie, M. Tzortziou, S. Ustin, Q. Yu, Y. Yusup, Q. Zhang, and the SBG Algorithms Working Group (2021). "NASA's surface biology and geology designated observable: A perspective on surface imaging algorithms". In: *Remote Sens. Environ.* 257, p. 112349. DOI: 10.1016/j.rse.2021.112349.

Cernicharo, J., A. Verger, and F. Camacho (2013). "Empirical and Physical Estimation of Canopy Water Content from CHRIS/PROBA Data". In: *Remote Sens.* 5.10, pp. 5265 –5284. DOI: 10.3390/rs5105265.

Champagne, C. M., K. Staenz, A. Bannari, H. McNairn, and J.-C. Deguise (2003). "Validation of a hyperspectral curve-fitting model for the estimation of plant water content of agricultural canopies". In: *Remote Sens. Environ.* 87, 188–197. DOI: 10.1016/S0034-4257(03)00137-8.

Chandrasekhar, S. (1960). *Radiative Transfer Theory*. Mineola, N.Y., USA: Dover Publications Inc., p. 393.

Cheng, T., B. Rivard, and A. Sanchez-Azofeifa (2011). "Spectroscopic determination of leaf water content using continuous wavelet analysis". In: *Remote Sens. Environ.* 115, pp. 659–670. DOI: 10.1109/IGARSS.2010.5654453.

Chlus, A., P. Townsend, and M. Gierach (2021). "SISTER: SBG Space-based Imaging Spectroscopy and Thermal pathfindER". In: *Hyperspectral Remote Sensing Workshop 2021: PRISMA Mission and beyond, 13-14 April 2021, online*.

Clarke, A. D. and K. J. Noone (1985). "Soot in the Artic snowpack: A cause for perturbations in radiative transfer". In: *Atmos. Environ.* 19, pp. 2045–2053. DOI: 10.1016/0004-6981(85)90113-1.

Clevers, J. G. P. W., L. Kooistra, and M. E. Schaepman (2008). "Using spectral information from the NIR water absorption features for the retrieval of canopy water content". In: *Int. J. Appl. Earth Obs.* 10.3, pp. 388 –397. DOI: 10.1016/j.jag.2008.03.003.

— (2010). "Estimating canopy water content using hyperspectral remote sensing data". In: *Int. J. Appl. Earth Obs.* 12, pp. 119–125. DOI: 10.1016/j.jag.2010.01.007.

Cogliati, S., F. Sarti, L. Chiarantini, M. Cosi, R. Lorusso, E. Lopinto, F. Miglietta, L. Genesio, L. Guanter, A. Damm, S. Pérez-López, D. Scheffler, G. Tagliabue, C. Panigada, U. Rascher, T. P. F. Dowling, C. Giardino, and R. Colombo (2021). "The PRISMA imaging spectroscopy mission: overview and first performance analysis". In: *Remote Sens. Environ.* 262, p. 112499. DOI: 10.1016/j.rse.2021.112499.

Colbeck, S. C. (1979). "Grain clusters in wet snow". In: *J. Colloid Interf. Sci.* 72, pp. 371 –384. DOI: 10.1016/0021-9797(79)90340-0.

Cook, J., A. Edwards, N. Takeuchi, and T. Irvine-Fynn (2016). "Cryoconite: The dark biological secret of the cryosphere". In: *Prog. Phys. Geogr.* 40.1, pp. 66–111. DOI: 10.1177/0309133315616574.

Cook, J. M., A. J. Hodson, A. S. Gardner, M. Flanner, A. J. Tedstone, C. Williamson, T. D. L. Irvine-Flynn, J. Nilsson, R. Bryant, and M. Tranter (2017a). "Quantifying bioalbedo: a new physically based model and discussion of empirical methods for characterising biological influence on ice and snow albedo". In: *Cryosphere* 11, pp. 2611–2632. DOI: 10.5194/tc-11-2611-2017.

Cook, J. M., A. J. Hodson, A. J. Taggart, S. H. Mernild, and M. Tranter (2017b). "A predictive model for the spectral "bioalbedo" of snow". In: *J. Geophys. Res. Earth Surf.* 122, pp. 434–454. DOI: 10.1002/2016JF003932.

Cook, J. M., A. J. Tedstone, C. Williamson, J. McCutcheon, A. J. Hodson, A. Dayal, M. Skiles, S. Hofer, R. Bryant, O. McAree, A. McGonigle, J. Ryan, A. M. Anesio, T. D. L. Irvine-Fynn, A. Hubbard, E. Hanna, M. Flanner, S. Mayanna, L. G. Benning, D. van As, M. Yallop, J. B. McQuaid, T. Gribbin, and M. Tranter (2020). "Glacier algae accelerate melt rates on the south-western Greenland Ice Sheet". In: *Cryosphere* 14, pp. 309–330. DOI: 10.5194/tc-14-309-2020.

Cressie, N. (2018). "Mission CO2ntrol: A statistical scientist's role in remote sensing of atmospheric carbon dioxide." In: *J. Am. Stat. Assoc.* 113.521, pp. 152–181. DOI: 10.1080/01621459.2017.1419136.

Dang, C., Q. Fu, and S. G. Warren (2016). "Effect of snow grain shape on snow albedo". In: *J. Atmos. Sci.* 73, pp. 3573–3583. DOI: 10.1175/JAS-D-15-0276.1.

Delegido, J., J. Verrelst, C. M. Meza, J. P. Rivera, L. Alonso, and J. Moreno (2013). "A red-edge spectral index for remote sensing estimation of green LAI over agroecosystems". In: *Eur. J. Agron.* 46, pp. 42–52. DOI: 10.1016/j.eja.2012.12.001.

Di Mauro, B. (2020). "A darker cryosphere in a warming world". In: *Nat. Clim. Chang.* 10, 979–980. DOI: 10.1038/s41558-020-00911-9.

Di Mauro, B., G. Baccolo, R. Garzonio, C. Giardino, D. Massabò, A. Piazzalunga, M. Rossini, and R. Colombo (2017). "Impact of impurities and cryoconite on the optical properties of the Morteratsch Glacier (Swiss Alps)". In: *Cryosphere* 11, 2393–2409. DOI: 10.5194/tc-11-2393-2017.

Di Mauro, B., F. Fava, L. Ferrero, R. Garzonio, G. Baccolo, B. Delmonte, and R. Colombo (2015). "Mineral dust impact on snow radiative properties in the European Alps combining ground, UAV, and satellite observations". In: *J. Geophys. Res. Atmos.* 120, 6080–6097. DOI: 10.1002/2015JD023287.

Di Mauro, B., R. Garzonio, G. Baccolo, A. Franzetti, F. Pittino, B. Leoni, D. Remias, R. Colombo, and M. Rossini (2020). "Glacier algae foster ice-albedo feedback in the European Alps". In: *Sci. Rep.* 10.4739. DOI: 10.1038/s41598-020-61762-0.

Dial, R. J., G. Q. Ganey, and S. M. Skiles (2018). "What color should glacier algae be?" In: *FEMS Microbiol. Ecol.* 53. DOI: 10.1093/femsec/fiy007.

Diamond, R., L. C. Sime, D. Schroeder, and M.-V. Guarino (2021). "The contribution of melt ponds to enhanced Arctic sea-ice melt during the Last Interglacial". In: *Cryosphere*. DOI: 10.5194/tc-2021-6.

Diedenhoven, B. van, A. S. Ackerman, B. Cairns, and A. M. Fridlind (2014). "A flexible parameterization for shortwave optical properties of ice crystals". In: *J. Atmos. Sci.* 71, pp. 1763–1782. DOI: 10.1175/JAS-D_13-0205.1.

Diedrich, H. (2016). "Observation of Total Column Water Vapour". PhD thesis. Freie Universitaet Berlin, Mathematisch-Naturwissenschaftliche Fakultaet.

Diedrich, H., R. Preusker, R. Lindstrot, and J. Fischer (2015). "Retrieval of daytime total columnar water vapour from modis measurements over land surfaces". In: *Atmos. Meas. Tech.* 8.2, 823–836. DOI: 10.5194/amt-8-823-2015.

Diedrich, H., R. Preusker, R., and J. Fischer (2013). "Quantification of uncertainties of water vapour column retrievals using future instruments". In: *Atmos. Meas. Tech.* 6, pp. 359–370. DOI: 10.5194/amt-6-359-2013.

Dozier, J. (1989). "Spectral signature of alpine snow cover from the Landsat Thematic Mapper". In: *Remote Sens. Environ.* 28, pp. 9–22. DOI: 10.1016/0034-4257(89)90101-6.

Dozier, J., R. O. Green, A. W. Nolin, and T. H. Painter (2009). "Interpretation of snow properties from imaging spectrometry". In: *Remote Sens. Environ.* 113, S25–S37. DOI: 10.1016/j.rse.2007.07.029.

Dozier, J. and D. Marks (1987). "Snow mapping and classification from Landsat Thematic Mapper data". In: *Ann. Glaciol.* 9, pp. 97–103. DOI: 10.3189/S026030550000046X.

Dozier, J. and T. H. Painter (2004). "Multispectral and hyperspectral remote sensing of alpine snow properties". In: *Annu. Rev. Earth Planet. Sci.* 32, 465–494. DOI: 10.1146/annurev.earth.32.101802.120404.

Dozier, J., S. R. Schneider, and D. F. McGinnis Jr. (1981). "Effect of grain size and snowpack water equivalence on visible and near-infrared satellite observations of snow". In: *Water Resour. Res.* 17.4, pp. 1213 –1221. DOI: 10.1029/WR017i004p01213.

Dumont, M., O. Brissaud, G. Picard, B. Schmitt, J.-C. Gallet, and Y. Arnaud (2010). "High-accuracy measurements of snow Bidirectional Reflectance Distribution Function at visible and NIR wavelengths – comparison with modelling results". In: *Atmos. Chem. Phys.* 10, 2507–2520. DOI: 10.5194/acp-10-2507-2010.

Dumont, M., E. Brun, G. Picard, M. Michou, Q. Libois, J.-R. Petit, M. Geyer, S. Morin, and B. Josse (2014). "Contribution of light-absorbing impurities in snow to Greenland's darkening since 2009". In: *Nat. Geosci.* 7, pp. 509–512. DOI: 10.1038/ngeo2180.

Flanner, M. G. and C. S. Zender (2006). "Linking snowpack microphysics and albedo evolution". In: *J. Geophys. Res.* 111. DOI: 10.1029/2005JD006834.

Flanner, M. G., C. S. Zender, P. G. Hess, N. M. Mahowald, T. H. Painter, V. Ramanathan, and P. J. Rasch (2009). "Springtime warming and reduced snow

cover from carbonaceous particles". In: *Atmos. Chem. Phys.* 9, pp. 2481–2497. DOI: 10.5194/acp-9-2481-2009.

Flanner, M. G., C. S. Zender, J. T. Randerson, and P. J. Rasch (2007). "Present-day climate forcing and response from black carbon in snow". In: *J. Geophys. Res.* 112. DOI: 10.1029/2006JD008003.

Frankenberg, C., D. Wunch, G. Toon, C. Risi, R. Scheepmaker, J.-E. Lee, P. Wennberg, and J. Worden (2013). "Water vapor isotopologue retrievals from high-resolution GOSAT schortwave infrared spectra". In: *Atmos. Meas. Tech.* 6, pp. 263–274. DOI: 10.5194/amt-6-263-2013.

Funk, C. C., J. Theiler, D. A. Roberts, and C. C. Borel (2001). "Clustering to improve matched filter detection of weak gas plumes in hyperspectral thermal imagery". In: *IEEE T. Geosci. Remote.* 39, pp. 1410–1420. DOI: 10.1109/36.934073.

Gallet, J.-C., F. Domine, and M. Dumont (2014). "Measuring the specific surface area of wet snow using 1310 nm reflectance". In: *Cryosphere* 8, pp. 1139–1148. DOI: 10.5194/tc-8-1139-2014.

Gallet, J.-C., F. Domine, C. S. Zender, and G. Picard (2009). "Measurement of the specific surface area of snow using infrared reflectance in an integrating sphere at 1310 and 1550 nm". In: *Cryosphere* 3, pp. 167–182. DOI: 10.5194/tc-3-167-2009.

Gao, B.-C. (1996). "NDWI - A normalized difference water index for remote sensing of vegetation liquid water from space". In: *Remote Sens. Environ.* 58.3, pp. 257–266. DOI: 10.1016/S0034-4257(96)00067-3.

Gao, B.-C. and A. F. H. Goetz (1990). "Column atmospheric water vapor and vegetation liquid water retrievals from airborne imaging spectrometer data". In: *J. Geophys. Res.* 95(D4), pp. 3549–3564. DOI: 10.1029/JD095iD04p03549.

— (1995). "Retrieval of equivalent water thickness and information related to biochemical components of vegetation canopies from AVIRIS data". In: *Remote Sens. Environ.* 52, pp. 155–162. DOI: 10.1016/0034-4257(95)00039-4.

Gao, B.-C., A. F. H. Goetz, E. R. Westwater, J. E. Conel, and R. O. Green (1993). "Possible near-IR channels for remote sensing precipitable water vapor from geostationary satellite platforms". In: *J. Appl. Meteorol.* 32, 1791–1801. DOI: 10.1175/1520-0450(1993)032<1791:PNICFR>2.0.CO;2.

Goetz, A. F. H., G. Vane, J. E. Salomon, and B. N. Rock (1985). "Imaging spectroscopy for earth remote sensing". In: *Science* 228, pp. 1147–1153. DOI: 10.1126/science.228.4704.1147.

Gorroño, J. and L. Guanter (2021). "Assessing the radiometric impact of the Sentinel 2 orthorectification process". In: *Proc. SPIE 11858, Sensors, Systems, and Next-Generation Satellites XXV* 118580W. DOI: 10.1117/12.2603730.

Govaerts, Y. M., S. Wagner, A. Lattanzio, and P. Watts (2010). "Joint retrieval of surface reflectance and aerosol optical depth from MSG/SEVIRI observations with an optimal estimation approach: 1. Theory". In: *J. Geophys. Res.* 115, p. D02203. DOI: 10.1029/2009JD011779.

Gray, A., M. Krolikowski, P. Fretwell, P. Convey, L. S. Peck, M. Mendelova, A. G. Smith, and M. P. Davey (2020). "Remote sensing reveals Antarctic green snow algae as important terrestrial carbon sink". In: *Nat. Commun.* 11.2527. DOI: 10.1038/s41467-020-16018-w.

Green, R. O., J. E. Conel, J. Margolis, J. C. Bruegge, and L. G. Hoover (1991). "An inversion algorithm for retrieval of atmospheric and leaf water absorption from AVIRIS radiance with compensation for atmospheric scattering". In: *Third Airborne Visible/Infrared Imaging Spectrometer (*AVIRIS*) Workshop*. Ed. by R. O. Green, pp. 51–61.

Green, R. O., J. Dozier, D. A. Roberts, and T. H. Painter (2002). "Spectral snow-reflectance models for grain-size and liquid-water fraction in melting snow for the solar-reflected spectrum". In: *Ann. Glaciol.* 34, pp. 71 –73. DOI: 10.3189/172756402781817987.

Green, R. O., M. L. Eastwood, C. M. Sarture, T. G. Chrien, M. Aronsson, B. J. Chippendale, J. A. Faust, B. E. Pavri, C. J. Chovit, M. Solis, M. R. Olah, and O. Williams (1998). "Imaging spectroscopy and the Airborne Visible/Infrared Imaging Spectrometer (AVIRIS)". In: *Remote Sens. Environ.* 65.3, pp. 227–248. DOI: 10.1016/S0034-4257(98)0064-9.

Green, R. O., N. M. Mahowald, R. N. Clark, B. L. Ehlmann, P. A. Ginoux, O. V. Kalashnikova, R. L. Miller, G. Okin, T. H. Painter, C. Pérez García-Pando, V. J. Realmuto, G. A. Swayze, D. R. Thompson, E. Middleton, L. Guanter, E. Ben Dor, and B. R. Phillips (2018). "NASA's Earth Surface Mineral Dust Source Investigation". In: *AGU Fall Meet.* Abstr. 24.

Green, R. O., T. H. Painter, D. A. Roberts, and J. Dozier (2006). "Measuring the expressed abundance of the three phases of water with an imaging spectrometer over melting snow". In: *Water Resour. Res.* 42, W10402. DOI: 10.1029/2005WR004509.

Grenfell, T. C. and S. G. Warren (1999). "Representation of a nonspherical ice particle by a collection of independent spheres for scattering and absorption of radiation". In: *J. Geophys. Res. (Atmospheres)* 104, pp. 31679 –31709. DOI: 10.1029/1999JD900496.

Guanter, L., L. Alonso, L. Gomez-Chova, and J. Moreno (2008b). "CHRIS/PROBA atmospheric correction module - algorithm theoretical basis document". In: *GeoForschungsZentrum, Potsdam, Germany*.

Guanter, L., L. Alonso, and J. Moreno (2005). "A Method for the Surface Reflectance Retrieval from PROBA/CHRIS Data Over Land: Application to ESA SPARC Campaigns". In: *IEEE T. Geosci. Remote* 43.12, pp. 2908–2917. DOI: 10.1109/TGRS.2005.857915.

Guanter, L., L. Gomez-Chova, and J. Moreno (2008a). "Coupled retrieval of aerosol optical thickness, columnar water vapor and surface reflectance maps from ENVISAT/MERIS data over land". In: *Remote Sens. Environ.* 112, pp. 2898–2913. DOI: 10.1016/J.RSE.2008.02.001.

Guanter, L., H. Kaufmann, K. Segl, S. Foerster, C. Rogass, S. Chabrillat, T. Kuester, A. Hollstein, G. Rossner, C. Chlebek, C. Straif, S. Fischer, S. Schrader, T. Storch, U. Heiden, A. Mueller, M. Bachmann, H. Muehle, R. Mueller, M. Habermeyer, A. Ohndorf, J. Hill, H. Buddenbaum, P. Hostert, S. van der Linden, P. J. Leitao, A. Rabe, R. Doerffer, H. Krasemann, H. Xi, W. Mauser, T. Hank, M. Locherer, M. Rast, K. Staenz, and B. Sang (2015). "The EnMAP spaceborne imaging spectroscopy mission for earth observation". In: *Remote Sens.* 7.7, pp. 8830–8857. DOI: 10.3390/rs70708830.

Guanter, L., R. Richter, and H. Kaufmann (2009). "On the application of the MODTRAN4 atmospheric radiative transfer code to optical remote sensing". In: *Int. J. Remote Sens.* 30.6, pp. 1407–1424. DOI: 10.1080/01431160802438555.

Hadley, O. and W. Kirchstetter (2012). "Black-carbon reduction of snow albedo". In: *Nat. Clim. Change* 2, pp. 437–440. DOI: 10.1038/nclimate1433.

Hall, D. K., G. A. Riggs, and V. V. Salomonson (1995). "Development of methods for mapping global snow cover using moderate resolution imaging spectroradiometer data". In: *Remote Sens. Environ.* 54, pp. 127–140. DOI: 10.1016/0034-4257(95)00137-P.

Hamlin, L., R. Green, P. Mouroulis, M. Eastwood, D. Wilson, M. Dudik, and C. Paine (2011). "Imaging spectrometer science measurements for terrestrial ecology: AVIRIS and new developments". In: *IEEE Aerospace Conference, Big Sky, MT USA*, pp. 1 –7.

Hardisky, M. A., V. Klemas, and R. M. Smart (1983). "The influence of soil-salinity, growth form, and leaf moisture on the spectral radiance of Spartina alterniflora canopies". In: *Photogramm. Eng. Remote. Sens.* 49, pp. 77–83.

Hoham, R. W. and D. Remias (2020). "Snow and Glacial Algae: A Review[1]". In: *J. Phycol.* 56.2, pp. 264–282. DOI: 10.1111/jpy.12952.

Hunt, E. R. and B. N. Rock (1989). "Detection of changes in leaf water content using near- and middle-infrared reflectances". In: *Remote Sens. Environ.* 30, pp. 43 – 54. DOI: 10.1016/0034-4257(89)90046-1.

Hunt, E. R., B. N. Rock, and P. S. Nobel (1987). "Measurement of leaf relative water content by infrared reflectance". In: *Remote Sens. Environ.* 22.3, pp. 429 –435. DOI: 10.1016/0034-4257(87)90094-0.

Hunt, E. R., S. L. Ustin, and D. Riano (2013). "Satellite-based applications on climate change". In: ed. by J. J. Qu, A. M. Powell, and M. V. K. Sivakumar. Springer. Chap. Remote sensing of leaf, canopy, and vegetation water contents for satellite environmental data records, pp. 335–357. DOI: 10.1007/978-94-007-5872-8_20.

Jackson, T. J., D. Chen, M. Cosh, F. Li, M. Anderson, C. Walthall, P. Doriaswamy, and E. R. Hunt (2004). "Vegetation water content mapping using Landsat data derived normalized difference water index for corn and soybeans". In: *Remote Sens. Environ.* 92.4, pp. 475–482. DOI: 10.1016/j.rse.2003.10.021.

Jacquemoud, S. and F. Baret (1990). "PROSPECT: a model of leaf optical properties spectra". In: *Remote Sens. Environ.* 34, pp. 75–91. DOI: 10.1016/0034-4257(90)90100-Z.

— (1992). "Crop structure and light microclimate: characterization and applications". In: ed. by C. Varlet-Grancher, R. Bonhomme, and H. Sinoquet. Editions de l'INRA. Chap. Estimating vegetation biophysical parameters by inversion of a reflectance model on high spectral resolution data, pp. 339–350.

Jacquemoud, S., W. Verhoef, F. Baret, C. Bacour, P. J. Zarco-Tejada, G. P. Asner, C. François, and S. L. Ustin (2009). "PROSPECT + SAIL models: A review of use for vegetation characterization". In: *Remote Sens. Environ.* 113.Supplement 1. Imaging Spectroscopy Special Issue, S56–S66. DOI: 10.1016/j.rse.2008.01.026.

Justice, C. O., J. R. G. Townshend, E. F. Vermote, E. Masuoka, R. E. Wolfe, N. Saleous, D. P. Roy, and J. T. Morisette (2002). "An overview of MODIS Land data processing and product status". In: *Remote Sens. Environ.* 83, pp. 3–15. DOI: 10.1016/S0034-4257(02)00084-6.

Kedenburg, S., M. Vieweg, T. Gissibl, and H. Giessen (2012). "Linear refractive index and absorption measurements of nonlinear optical liquids in the visible and near-infrared spectral region". In: *Opt. Mater. Express* 2.11, pp. 1588–1611. DOI: 10.1364/OME.2.001588.

Kiehl, J. T. and K. E. Trenberth (1997). "Earth's Annual Global Mean Energy Budget". In: *B. Am. Meteorol. Soc.* 78, pp. 197–208. DOI: 10.1175/1520-0477(1997)078<0197:EAGMEB>2.0.CO;2.

Kochanov, R. V., I. E. Gordon, L. S. Rothman, P. Wcislo, C. Hill, and J. S. Wilzewski (2016). "HITRAN Application Programming Interface (HAPI): A comprehensive approach to working with spectroscopic data". In: *J. Quant. Spectrosc. Radiat. Transfer* 177, pp. 15–30. DOI: 10.1016/j.jqsrt.2016.03.005.

Kokhanovsky, A., M. Lamare, O. Danne, C. Brockmann, M. Dumont, G. Picard, L. Arnaud, V. Favier, B. Jourdain, E. Le Meur, B. Di Mauro, T. Aoki, M. Niwano, V. Rozanov, S. Korkin, S. Kipfstuhl, J. Freitag, M. Hoerhold, A. Zuhr, D. Vladimirova, A.-K. Faber, H. C. Steen-Larsen, S. Wahl, J. K. Andersen, B. Vandecrux, D. van As, K. D. Mankoff, M. Kern, E. Zege, and J. E. Box (2019). "Retrieval of Snow Properties from the Sentinel-3 Ocean and Land Colour Instrument". In: *Remote Sens.* 11. DOI: 10.3390/rs11192280.

Kokhanovsky, A. A. (2006). "Scaling constant and its determination from simultaneous measurements of light reflection and methane adsorption by snow samples". In: *Opt. Lett.* 31, 3282–3284. DOI: 10.1364/OL.31.003282.

Kokhanovsky, A. A., J. Box, and B. Vandecrux (2020). "Pre-operational Sentinel-3 Snow and Ice (SICE) Products". In: *Algorithm Theoretical Basis Document, Version 3.1, September 22, 2020.* DOI: 10.20944/preprints202009.0529.v1.

Kokhanovsky, A. A. and E. P. Zege (2004). "Scattering optics of snow". In: *Appl. Optics* 43.7, pp. 1589–1602. DOI: 10.1364/AO.43.001589.

Kou, L., D. Labrie, and P. Chylek (1993). "Refractive indices of water and ice in the 0.65- to 2.5-$\mu m$ spectral range". In: *Appl. Opt.* 32.19, pp. 3531–3540. DOI: 10.1364/AO.32.003531.

Kuester, T. (2011). "Modellierung von Getreidebestandsspektren zur Korrektur BRDF-bedingter Einfluesse auf Vegetationsindizes im Rahmen der EnMAP-Mission". PhD thesis. Humboldt-Universitaet zu Berlin, Mathematisch-Naturwissenschaftliche Fakultaet II.

Kuester, T., S. Foerster, S. Chabrillat, D. Spengler, and L. Guanter (2017). "Assessing The Influence Of Variable Fractional Vegetation Cover On Soil Spectral Features Using Simulated Canopy Reflectance Modeling". In: *10th EARSeL SIG Imaging Spectroscopy Workshop, Zurich, Switzerland.* Zurich, Switzerland.

Kuester, T., D. Spengler, J.-F. Barczi, K. Segl, P. Hostert, and H. Kaufmann (2014). "Simulation of multitemporal and hyperspectral vegetation canopy bidirectional reflectance using detailed virtual 3D canopy models". In: *IEEE T. Geosci. Remote* 52.4, pp. 2096–2108. DOI: 10.1109/TGRS.2013.2258162.

Kuester, Theres and Daniel Spengler (2018). "Structural and Spectral Analysis of Cereal Canopy Reflectance and Reflectance Anisotropy". In: *Remote Sens.* 10.11. DOI: 10.3390/rs10111767.

Lamare, M., M. Dumont, G. Picard, F. Larue, F. Tuzet, C. Delcourt, and L. Arnaud (2020). "Simulating optical top-of-atmosphere radiance satellite images over snow-covered rugged terrain". In: *Cryosphere* 14, 3995–4020. DOI: 10.5194/tc-14-3995-2020.

Lee, C. M., M. L. Cable, S. J. Hook, R. O. Green, S. L. Ustin, D. J. Mandl, and E. M. Middleton (2015). "An introduction to the NASA Hyperspectral InfraRed Imager (HyspIRI) mission and preparatory activities". In: *Remote Sens. Environ.* 167, pp. 6–19. DOI: 10.1016/j.rse.2015.06.012.

Lewis, P. (1999). "Three-dimensional plant modeling for remote sensing simulation studies using the botanical plant modeling system". In: *Agronomie* 19, pp. 185–210. DOI: 10.1051/agro:19990302.

Li, L., Y. B. Cheng, S. L. Ustin, X. T. Hua, and D. Riano (2008). "Retrieval of vegetation equivalent water thickness from reflectance using genetic algorithm (GA)-partial least squares (PLS) regression". In: *Adv. Space Res.* 41, pp. 1755–1763. DOI: 10.1016/j.asr.2008.02.015.

Libois, Q., G. Picard, M. Dumont, L. Arnaud, C. Sergent, E. Pougatch, M. Sudul, and D. Vial (2014). "Experimental determination of the absorption enhancement parameter of snow". In: *J. Glaciol.* 7, 714–724. DOI: 10.3189/2014JoG14J015.

Libois, Q., G. Picard, J. L. France, L. Arnaud, M. Dumont, C. M. Carmagnola, and M. D. King (2013). "Influence of grain shape on light penetration in snow". In: *Cryosphere* 7, pp. 1803–1818. DOI: 10.5194/tc-7-1803-2013.

Lindstrot, R., R. Preusker, H. Diedrich, L. Doppler, R. Bennartz, and J. Fischer (2012). "1D-Var retrieval of daytime total columnar water vapour from MERIS measurements". In: *Atmos. Meas. Tech.* 5, 631– 646. DOI: 10.5194/amt-5-631-2012.

Liu, Y., J. Stanturf, and S. Goodrick (2010). "Trends in global wildfire potential in a changing climate". In: *Forest. Ecol. Manag.* 259, 685–697. DOI: 10.1016/j.foreco.2009.09.002.

Loizzo, R., R. Guarini, F. Longo, T. Scopa, R. Formaro, C. Facchinetti, and G. Varacalli (2018). "PRISMA: The Italian hyperspectral mission". In: *Proc. IGARSS*.

Makarau, A., R. Richter, D. Schlaepfer, and P. Reinartz (2017). "APDA Water Vapor Retrieval Validation for Sentinel-2 Imagery". In: *IEEE Geosci. Remote S.* 14.2, pp. 227–231. DOI: 10.1109/LGRS.2016.2635942.

Malenovský, Z., H. Rott, J. Cihlar, M. E. Schaepman, G. García-Santos, R. Fernandes, and M. Berger (2012). "Sentinels for science: Potential of Sentinel-1, -2, and -3 missions for scientific observations of ocean, cryosphere, and land". In: *Remote Sens. Environ.* 120, pp. 91–101. DOI: 10.1016/j.rse.2011.09.026.

Malinka, A., E. Zege, L. Istomina, G. Heygster, G. Spreen, D. Perovich, and C. Polashenski (2018). "Reflective properties of melt ponds on sea ice". In: *Cryosphere* 12, 1921–1937. DOI: 10.5194/tc-12-1921-2018.

Malinka, A. V. (2014). "Light scattering in porous materials: Geometrical optics and stereological approach". In: *J. Quant. Spectrosc. Ra.* 141, pp. 14–23. DOI: 10.1016/j.jqsrt.2014.02.022.

Masek, J. G., M. A. Wulder, B. Markham, J. McCorkel, C. J. Crawford, J. Storey, and D. T. Jenstrom (2020). "Landsat 9: Empowering open science and applications through continuity". In: *Remote Sens. Environ.* 248, p. 111968. DOI: 10.1016/j.rse.2020.111968.

Meier, U. (1997). *Growth stages of mono- and dicotyledonous plants: BBCH-Monograph.* Blackwell Wissenschafts-Verlag, p. 622.

Milewski, R., S. Chabrillat, M. Brell, A. M. Schleicher, and L. Guanter (2019). "Assessment of the 1.75 $\mu m$ absorption feature for gypsum estimation using laboratory, air- and spaceborne hyperspectral sensors". In: *Int. J. Appl. Earth. Obs.* 77, pp. 69–83. DOI: 10.1016/j.jag.2018.12.012.

Mueller, R., J. Avbelj, E. Carmona, A. Eckhardt, B. Gerasch, L. Graham, B. Guenther, U. Heiden, J. Ickers, G. Kerr, U. Knodt, D. Krutz, H. Krawczyk, A. Makarau, R. Miller, R. Perkins, and I. Walter (2016). "The new hyperspectral sensor DESIS on the multi-payload platform MUSES installed on the ISS". In: *Int. Arch. Photogramm.* 41, pp. 461–467. DOI: 10.5194/isprsarchives-XLI-B1-461-2016.

Munro, R., M. Eisinger, C. Anderson, J. Callies, E. Corpaccioli, R. Lang, A. Lefebvre, Y. Livschitz, and A. P. Albiñana (2006). "GOME-2 on MetOp". In: *Proc. of The 2006 EUMETSAT Meteorological Satellite Conference, Helsinki, Finland*, pp. 12–16.

National Academies of Sciences, Engineering, and Medicine (2018). *Thriving on Our Changing Planet: A Decadal Strategy for Earth Observation from Space.* Washington, DC: National Academies Press. DOI: 10.17226/24938.

Nicodemus, F. E., J. C. Richmond, J. J. Hsia, I. W. Ginsberg, and T. Limperis (1977). *Geometrical Considerations and Nomenclature for Reflectance.* Tech. rep. National Bureau of Standards, Washington, D.C. 20234.

Noël, S., M. Buchwitz, H. Bovensmann, and J. P. Burrows (2002). "Retrieval of total water vapour column amounts from GOME/ERS-2 data". In: *Adv. Space Res.* 29, pp. 1697 –1702. DOI: 10.1016/S0273-1177(02)00099-6.

Nolin, A. W. and J. Dozier (1993). "Estimating snow grain size using AVIRIS data". In: *Remote Sens. Environ.* 44.2-3, pp. 231–238. DOI: 10.1016/0034-4257(93)90018-S.

Nolin, A. W. and J. Dozier (2000). "A hyperspectral method for remotely sensing the grain size of snow". In: *Remote Sens. Environ.* 74.2, pp. 207–216. DOI: 10.1016/S0034-4257(00)00111-5.

Painter, T. H., D. F. Berisford, J. W. Boardman, K. J. Bormann, J. S. Deems, F. Gehrke, A. Hedrick, M. Joyce, R. Laidlawa, D. Marks, C. Mattmanna, B. McGurk, P. Ramirez, M. Richardson, S. M. Skiles, F. C. Seidel, and A. Winstral (2016). "The Airborne Snow Observatory: Fusion of scanning lidar, imaging spectrometer, and physically-based modeling for mapping snow water equivalent and snow albedo". In: *Remote Sens. Environ.* 184, pp. 139–152. DOI: 10.1016/j.rse.2016.06.018.

Painter, T. H. and J. Dozier (2004a). "Measurements of the hemispherical-directional reflectance of snow at fine spectral and angular resolution". In: *J. Geophys. Res* 109.D18115. DOI: 10.1029/2003JD004458.

— (2004b). "The effect of anisotropic reflectance on imaging spectroscopy of snow properties". In: *Remote Sens. Environ.* 89, pp. 409 –422. DOI: 10.1016/j.rse.2003.09.007.

Painter, T. H., J. Dozier, D. A. Roberts, R. E. Davis, and R. O. Green (2003). "Retrieval of subpixel snow-covered area and grain size from imaging spectrometer data". In: *Remote Sens. Environ.* 85, pp. 64–77. DOI: 10.1016/S0034-4257(02)00187-6.

Painter, T. H., B. Duval, and W. H. Thimas (2001). "Detection and quantification of snow algae with an airborne imaging spectrometer". In: *Appl. Environ. Microbiol.* 67.11, pp. 5267–5272. DOI: 10.1128/AEM.67.11.5267-5272.2001.

Painter, T. H., N. Molotch, M. Cassidy, M. Flanner, and K. Steffen (2007). "Contact spectroscopy for the determination of stratigraphy of snow grain size". In: *J. Glaciol.* 53, pp. 121–127. DOI: 10.3189/172756507781833947.

Painter, T. H., F. C. Seidel, A. C. Bryant, S. McKenzie Skiles, and K. Rittger (2013). "Imaging spectroscopy of albedo and radiative forcing by light-absorbing impurities in mountain snow". In: *J. Geophys. Res. Atmos.* 118, pp. 1–13. DOI: 10.1002/jgrd.50520.

Painter, T. H., S. M. Skiles, J. S. Deems, A. C. Bryant, and C. C. Landry (2012). "Dust radiative forcing in snow of the Upper Colorado River Basin: 1. A 6 year record of energy balance, radiation, and dust concentrations". In: *Water Resour. Res.* 48.W07521. DOI: 10.1029/2012WR011985.

Pasqualotto, N., J. Delegido, S. Van Wittenberghe, J. Verrelst, J. P. Rivera, and J. Moreno (2018). "Retrieval of canopy water content of different crop types with two new hyperspectral indices: Water Absorption Area Index and Depth

Water Index". In: *Int. J. Appl. Earth Obs. Geoinformation* 67, pp. 69–78. DOI: 10.1016/j.jag.2018.01.002.

Peñuelas, J., I. Filella, C. Biel, L. Serrano, and R. Savé (1993). "The reflectance at the $950-970nm$ region as an indicator of plant water status". In: *Int. J. Remote Sens.* 14, pp. 1887 –1905. DOI: 10.1080/01431169308954010.

Peñuelas, J., J. Pinol, R. Ogaya, and I. Filella (1997). "Estimation of plant water concentration by the reflectance water index wi (r900/r970)". In: *Int. J. Remote Sens.* 18, pp. 2869 –2875. DOI: 10.1080/014311697217396.

Petty, G. W. (2004). *A First Course in Atmospheric Radiation*. 1. Madison, WI, USA: Sundog Publishing, p. 446.

Pope, A., T. A. Scambos, M. Moussavi, M. Tedesco, M. Willis, D. Shean, and S. Grigsby (2016). "Estimating supraglacial lake depth in West Greenland using Landsat 8 and comparison with other multispectral methods". In: *Cryosphere* 10, pp. 15–27. DOI: 10.5194/tc-10-15-2016.

Preusker, R., C. Carbajal Henken, and J. Fischer (2021). "Retrieval of Daytime Total Column Water Vapour from OLCI Measurements over Land Surfaces". In: *Remote Sens.* 13, p. 932. DOI: 10.3390/rs13050932.

Proksch, M., H. Löwe, and M. Schneebeli (2015). "Density, specific surface area, and correlation length of snow measured by high-resolution penetrometry". In: *J. Geophys. Res.-Earth* 120.2, pp. 346–362. DOI: 10.1002/2014JF003266.

Rango, A. and K. Itten (1976). "Satellite potentials in snowcover monitoring and runoff prediction". In: *Nord. Hydrol.* 7, pp. 209–230. DOI: 10.2166/nh.1976.0014.

Rasmussen, C. E. and C. K. I. Williams (2006). *Gaussian Processes for Machine Learning*. Cambridge, MA, USA: The MIT Press, p. 248.

Rast, M., C. Ananasso, H. Bach, E. Ben Dor, S. Chabrillat, R. Colombo, U. Del Bello, J.-B. Feret, C. Giardino, R. O. Green, L. Guanter, S. Marsh, J. Nieke, C. Ong, G. Rum, M. Schaepman, M. Schlerf, A. K. Skidmore, and P. Strobl (2019). *Copernicus Hyperspectral Imaging Mission for the Environment - Mission Requirements Document*. Tech. rep. ESA-EOPSM-CHIM-MRD-3216. Keplerlaan 1, 2201 AZ Noordwijk, The Netherlands: European Space Agency (ESA).

Riggs, G. A. and D. K. Hall (2015). *MODIS snow products collection 6 user guide*. Tech. rep., p. 66.

Roberts, D., K. Brown, R. Green, S. Ustin, and T. Hinckley (1998a). "Investigating the relationship between liquid water and leaf area in clonal populus". In: *Summaries of the Seventh JPL Airborne Earth Science Workshop January 12-16, 1998* 1, pp. 335–344.

Roberts, D. A., M. Gardner, R. Church, S. Ustin, G. Scheer, and R. O. Green (1998b). "Mapping chaparral in the Santa Monica Mountains using multiple endmember spectral mixture models". In: *Remote Sens. Environ.* 65.3, pp. 267–279. DOI: 10.1016/S0034-4257(98)00037-6.

Roberts, D. A., R. 0. Green, and J. B. Adams (1997). "Tempora1 and Spatial Patterns in Vegetation and Atmospheric Properties from AVIRIS". In: *Remote Sens. Environ.* 62, pp. 223–240. DOI: 10.1016/S0034-4257(97)00092-8.

Rodgers, C. D. (2000). *Inverse Methods for Atmospheric Sounding: Theory and Practice*. Oxford, UK: World Scientific Pub Co., p. 240.

Rothman, L. S., I. E. Gordon, A. Barbe, D. Chris Brenner, P. F. Bernath, M. Birk, V. Boudon, L. R. Brown, A. Campargue, J.-P. Champion, K. Chance, L. H. Coudert, V. Diana, V. M. Devi, S. Fally, J.-M. Flaud, R. R. Gamache, A. Goldman, D. Jacquemart, I. Kleiner, N. Lacome, W. J. Lafferty, J.-Y. Mandin, S. T. Massie, S. N. Mikhailenko, C. E. Miller, N. Moazzen-Ahmadi, O. V. Naumenko, A. V. Nikitin, J. Orphal, V. I. Perevalov, A. Perrin, A. Predoi-Cross, C. P. Rinsland, M. Rotger, M. Simeckova, M. A. H. Smith, K. Sung, S. A. Tashkun, J. Tennyson, R. A. Toth, A. C. Vandaele, and J. Vander Auwera (2009). "The HITRAN 2008 molecular spectroscopic database". In: *J. Quant. Spectrosc. Ra.* 110, pp. 533–572. DOI: DOI:10.1016/j.jqsrt.2009.02.013.

Ryan, J. C., A. Hubbard, M. Stibal, T. D. Irvine-Fynn, J. Cook, L. C. Smith, K. Cameron, and J. Box (2018). "Dark zone of the Greenland Ice Sheet controlled by distributed biologically-active impurities". In: *Nat. Commun.* 9.1065. DOI: 10.1038/s41467-018-03353-2.

Schaepman, M. E., S. L. Ustin, A. J. Plaza, T. H. Painter, J. Verrelst, and S. Liang (2009). "Earth system science related imaging spectroscopy - An assessment". In: *Remote Sens. Environ.* 113, S123–S137. DOI: 10.1016/j.rse.2009.03.001.

Schaepman-Strub, G., M. E. Schaepman, T. H. Painter, S. Dangel, and J. V. Martonchik (2006). "Reflectance quantities in optical remote sensing-definitions and case studies". In: *Remote Sens. Environ.* 103, pp. 27–42. DOI: 10.1016/j.rse.2006.03.002.

Schlaepfer, D., C. C.Borel, J. Keller, and K. I. Itten (1998). "Atmospheric Precorrected Differential Absorption Technique to Retrieve Columnar Water Vapor". In: *Remote Sens. Environ.* 65.3, pp. 353–366. DOI: 10.1016/S0034-4257(98)00044-3.

Schulze, E. D. and A. E. Hall (1982). "Stomatal responses, water loss and CO2 assimilation rates of plants in contrasting environments". In: *Physiological plant ecology II*. Ed. by O. L. Lange, P.S. Nobel, C. B. Osmond, and H. Ziegler. Berlin Heidelberg: Springer, 181–230.

Segl, K., T. Kuester, C. Rogass, H. Kaufmann, B. Sang, and S. Hofer (2012). "EeteS - the EnMAP End-to-End Simulation Tool". In: *IEEE J. Sel. Top. Appl.* 5.2, pp. 522–530. DOI: 10.1109/JSTARS.2012.2188994.

Seidel, F. C., K. Rittger, S. McKenzie Skiles, N. P. Molotch, and T. H. Painter (2016). "Case study of spatial and temporal variability of snow cover, grain size, albedo and radiative forcing in the Sierra Nevada and Rocky Mountain snowpack derived from imaging spectroscopy". In: *Cryosphere* 10, 1229–1244. DOI: 10.5194/tc-10-1229-2016.

Serrano, L., S. L. Ustin, D. A. Roberts, J. A. Gamon, and J. Peñuelas (2000). "Deriving Water Content of Chaparral Vegetation from AVIRIS Data". In: *Remote Sens. Environ.* 74, 570–581. DOI: 10.1016/S0034-4257(00)00147-4.

Sirguey, P., R. Mathieu, and Y. Arnaud (2009). "Subpixel monitoring of the seasonal snow cover with MODIS at 250 m spatial resolution in the Southern Alps of New Zealand: Methodology and accuracy assessment". In: *Remote Sens. Environ.* 113.1, pp. 160–181. DOI: 10.1016/j.rse.2008.09.008.

Skiles, S. M., M. Flanner, J. M. Cook, M. Dumont, and T. H. Painter (2018). "Radiative forcing by light-absorbing particles in snow". In: *Nat. Clim. Change* 8, pp. 964–971. DOI: 10.1038/s41558-018-0296-5.

Skiles, S. M. and T. H. Painter (2018). "Assessment of radiative forcing by light absorbing particles in snow from in situ observations with radiative transfer modeling". In: *J. Hydrometeorol.* DOI: 10.1175/JHM-D-18_0072.1.

Skiles, S. M., T. H. Painter, and G. S. Okin (2017). "A method to retrieve the spectral complex refractive index and single scattering optical properties of dust deposited in mountain snow". In: *J. Glaciol.* 63, pp. 133–147. DOI: 10.1017/jog.2016.126.

Sneed, W. A. and G. S. Hamilton (2011). "Validation of a method for determining the depth of glacial melt ponds using satellite imagery". In: *Ann. Glaciol.* 52.59, pp. 15–22. DOI: 10.3189/172756411799096240.

Spengler, D. (2014). "Charakterisierung von Getreidearten aus hyperspektralen Fernerkundungsdaten auf der Basis von 4D-Bestandsmodellen". PhD thesis. Technische Universitaet Berlin, Fakultaet VI - Planen Bauen Umwelt.

Spengler, D., A. Frick, C. Davey, T. Peisker, and H. Kaufmann (2011). "Estimation of surface soil moisture content using imaging spectroscopy - a simulation case study". In: *7th EARSeL SIG Imaging Spectroscopy Workshop, Edinburgh, Scotland, United Kingdom.*

Spengler, D., T. Kuester, A. Frick, D. Scheffler, and H. Kaufmann (2013). "Correcting the influence of vegetation on surface soil moisture indices by using hyperspectral artificial 3D-canopy models". In: *Proceedings SPIE, Dresden, Germany.* Vol. 8887, p. 9. DOI: 10.1117/12.2028496.

Stamnes, K., S. C. Tsay, W. Wiscombe, and K. Jayaweera (1988). "A numerically stable algorithm for discrete ordinates method radiative transfer in multiple scattering and emitting layered media". In: *Appl. Optics* 27, pp. 2502–2509. DOI: 10.1364/AO.27.002502.

Stibal, M., J. E. Box, K. A. Cameron, P. L. Langen, M. Yallop, R. H. Mottram, A. L. Khan, N. P. Molotch, N. A. M. Chrismas, F. C. Quaglia, D. Remias, C. J. P. Smeets, M. R. van den Broecke, J. C. Ryan, A. Hubbard, M. Tranter, D. van As, and A. P. Ahlstrøm (2017). "Algae drive enhanced darkening of bare ice on the Greenland Ice Sheet". In: *Geophys. Res. Lett.* 44, pp. 11463–11471. DOI: 10.1002/2017GL075958.

Stillinger, T., D. A. Roberts, N. M. Collar, and J. Dozier (2019). "Cloud Masking for Landsat 8 and MODIS Terra Over Snow-Covered Terrain: Error Analysis and Spectral Similarity Between Snow and Cloud". In: *Water Resour. Res.* 55.7, 6169–6184. DOI: 10.1029/2019WR024932.

Susiluoto, J., N. Bohn, A. Braverman, P. G. Brodrick, N. Carmon, M. Gunson, H. Nguyen, D. R. Thompson, and M. Turmon (2021). "Accelerated optimal estimation: high-performance Bayesian retrievals for future imaging spectroscopy missions". In: *Submitted to Atmos. Meas. Tech.*

Takeuchi, N., R. Dial, S. Kohshima, T. Segawa, and J. Uetake (2006). "Spatial distribution and abundance of red snow algae on the Harding Icefield, Alaska derived from a satellite image". In: *Geophys. Res. Lett* 33.L21502. DOI: 10.1029/2006GL027819.

Tedesco, M., S. Doherty, X. Fettweis, P. Alexander, J. Jeyaratnam, and J. Stroeve (2016). "The darkening of the Greenland ice sheet: trends, drivers and projections (1981-2100)". In: *Cryosphere* 10, pp. 477–496. DOI: 10.5194/tc-10-477-2016.

Thompson, D. R., N. Bohn, P. G. Brodrick, N. Carmon, M. L. Eastwood, C. Fichot, J. P. Harringmeyer, H. M. Nguyen, M. Simard, and A. K. Thorpe (2021). "Atmospheric lengthscales for global VSWIR imaging spectroscopy". In: *Submitted to J. Geophys. Res.-Biogeo.*

Thompson, D. R., B.-C. Gao, R. O. Green, D. A. Roberts, P. E. Dennison, and S. R. Lundeen (2015). "Atmospheric correction for global mapping spectroscopy: ATREM advances for the HyspIRI preparatory campaign". In: *Remote Sens. Environ.* 167, pp. 64–77. DOI: 10.1016/j.rse.2015.02.010.

Thompson, D. R., I. McCubbin, B.-C. Gao, R. O. Green, A. A. Matthews, F. Mei, K. G. Meyer, S. Platnick, B. Schmid, J. Tomlinson, and E. Wilcox (2016). "Measuring cloud thermodynamic phase with shortwave infrared imaging spectroscopy". In: *J. Geophys. Res.-Atmos.* 121, pp. 9174–9190. DOI: 10.1002/2016JD024999.

Thompson, D. R., V. Natraj, R. O. Green, M. C. Helmlinger, B.-C. Gao, and M. L. Eastwood (2018). "Optimal estimation for imaging spectrometer atmospheric correction". In: *Remote Sens. Environ.* 216, pp. 355–373. DOI: 10.1016/j.rse.2018.07.003.

Tol, C. van der, W. Verhoef, J. Timmermans, A. Verhoef, and Z. Su (2009). "An integrated model of soil-canopy spectral radiances, photosynthesis, fluorescence, temperature and energy balance". In: *Biogeosciences* 6.12, pp. 3109–3129. DOI: 10.5194/bg-6-3109-2009.

Toon, O. B., C. P. McKay, T. P. Ackerman, and K. Santhanam (1989). "Rapid calculation of radiative heating rates and photodissociation rates in inhomogeneous multiple scattering atmospheres". In: *J. Geophys. Res.* 94.16, pp. 287–301. DOI: 10.1029/JD094iD13p16287.

Trenberth, K. E., J. T. Fasullo, and J. Kiehl (2009). "Earth's Global Energy Budget". In: *B. Am. Meteorol. Soc.* 30, pp. 311–324. DOI: 10.1175/2008BAMS2634.1.

Trombetti, M., D. Riano, M. A. Rubio, Y. B. Cheng, and S. Ustin (2008). "Multitemporal vegetation canopy water content retrieval using artificial neural networks for the USA". In: *Remote Sens. Environ.* 112, pp. 203–215. DOI: 10.1016/j.rse.2007.04.013.

Tuzet, F., M. Dumont, L. Arnaud, D. Voisin, M. Lamare, F. Larue, J. Revuelto, and G. Picard (2019). "Influence of light-absorbing particles on snow spectral irradiance profiles". In: *Cryosphere* 13, pp. 2169–2187. DOI: 10.5194/tc-13-2169-2019.

Tuzet, F., M. Dumont, G. Picard, M. Lamare, D. Voisin, P. Nabat, M. Lafaysse, F. Larue, J. Revuelto, and L. Arnaud (2020). "Quantification of the radiative impact of light-absorbing particles during two contrasted snow seasons at Col du Lautaret (2058 m a.s.l., French Alps)". In: *Cryosphere* 14, pp. 4553–4579. DOI: 10.5194/tc-14-4553-2020.

Vane, G. and A. F. H. Goetz (1988). "Terrestrial imaging spectroscopy for earth remote sensing". In: *Remote Sens. Environ.* 24, pp. 1–29. DOI: 10.1016/0034-4257(88)90003-X.

Vane, G., R. O. Green, T. G. Chrien, H. T. Enmark, E. G. Hansen, and W. M. Porter (1993). "The Airborne Visible/Infrared Imaging Spectrometer (AVIRIS)". In: *Remote Sens. Environ.* 44.2-3, pp. 127 –143. DOI: 10.1016/S0034-4257(93)90012-M.

Vohland, M. (2008). "Using imaging and non-imaging spectroradiometer data for the remote detection of vegetation water content". In: *J. Appl. Remote Sens.* 2.1, p. 023520. DOI: 10.1117/1.2937937.

Wagner, S. C., Y. M. Govaerts, and A. Lattanzio (2010). "Joint retrieval of surface reflectance and aerosol optical depth from MSG/SEVIRI observations with an optimal estimation approach: 2. Implementation and evaluation". In: *J. Geophys. Res.* 115, p. D02204. DOI: 10.1029/2009JD011780.

Wagner, T., S. Beirle, M. Grzegorski, and U. Platt (2006). "Global trends (1996-2003) of total column precipitable water observed by Global Ozone Monitoring Experiment (GOME) on ERS-2 and their relation to near-surface temperature". In: *J. Geophys. Res.* 111, p. D12102. DOI: 10.1029/2005ID006523.

Wagner, T., S. Beirle, H. Sihler, and K. Mies (2013). "A feasibility study for the retrieval of the total column precipitable water vapour from satellite observations in the blue spectral range". In: *Atmos. Meas. Tech.* 6, pp. 2593 –2605. DOI: 10.5194/amt-6-2593-2013.

Wang, S., M. Tedesco, P. M. Alexander, M. Xu, and X. Fettweis (2020). "Quantifying spatiotemporal variability of glacier algal blooms and the impact on surface albedo in southwestern Greenland". In: *Cryosphere* 14, 2687 – 2713. DOI: 10.5194/tc-14-2687-2020.

Wang, S., M. Tedesco, M. Xu, and P. M. Alexander (2018). "Mapping ice algal blooms in southwest Greenland from space". In: *Geophys. Res. Lett.* 45.11, pp. 779 –788. DOI: 10.1029/2018GL080455.

Warren, S. G. (1982). "Optical properties of snow". In: *Rev. Geophys.* 20.1, pp. 67–89. DOI: 10.1029/RG020i001p00067.

— (1984). "Optical constants of ice from the ultraviolet to the microwave". In: *Appl. Optics* 23.8, pp. 1206–1225. DOI: 10.1364/AO.23.001206.

— (2019). "Optical properties of snow and ice". In: *Phil. Trans. R. Soc. A* 337. DOI: 10.1098/rsta.2018.0161.

Warren, S. G. and R. E. Brandt (2008). "Optical constants of ice from the ultraviolet to the microwave: A revised compilation". In: *J. Geophys. Res.* 113. DOI: 10.1029/2007JD009744.

Warren, S. G. and W. J. Wiscombe (1980). "A model for the spectral albedo of snow. II: Snow containing atmospheric aerosols". In: *J. Atmos. Sci.* 37, pp. 2734–2745. DOI: 10.1175/1520-0469(1980)037<2734:AMFTSA>2.0.CO;2.

Widlowski, J.-L., M. Taberner, B. Pinty, V. Bruniquel-Pinel, M. Disney, R. Fernades, J.-P. Gastellu-Etchegorry, N. Gobron, A. Kuusk, T. Lavergne, S. Leblanc, P. Lewis, E. Martin, M. M. Ottus, P. R. J. North, W. Qin, M. Robustelli, N. Rochdi, R. Ruiloba, C. Soler, R. Thompson, W. Verhoef, M. M. Verstraete, and D. Xie (2007). "The third RAdiation transfer Model Intercomparison (RAMI) exercise: Documenting progress in canopy reflectance models". In: *J. Geophys. Res.* 112.D09111, p. 28. DOI: 10.1029/2006JD007821.

Wientjes, I. G. M., R. S. W. Van de Wal, G. J. Reichart, A. Sluijs, and J. Oerlemans (2011). "Dust from the dark region in the western ablation zone of the Greenland ice sheet". In: *Cryosphere* 5, 589–601. DOI: 10.5194/tc-5-589-2011.

Williamson, C. J., A. M. Anesio, J. Cook, A. Tedstone, E. Poniecka, A. Holland, D. Fagan, M. Tranter, and M. L. Yallop (2018). "Ice algal bloom development on the surface of the Greenland Ice Sheet". In: *FEMS Microbiol. Ecol.* 94. DOI: 10.1093/femsec/fiy025.

Wiscombe, W. J. (1980). "Improved Mie scattering algorithms". In: *Appl. Optics* 19.9, pp. 1505–1509. DOI: 10.1364/AO.19.001505.

Wiscombe, W. J. and S. G. Warren (1980). "A model for the spectral albedo of snow. I: Pure snow". In: *J. Atmos. Sci.* 37, pp. 2712–2733. DOI: 10.1175/1520-0469(1980)0372.0.CO;2.

Wocher, M., K. Berger, M. Danner, W. Mauser, and T. Hank (2018). "Physically-Bases Retrieval of Canopy Equivalent Water Thickness Using Hyperspectral Data". In: *Remote Sens.* 10, pp. 1924–1940. DOI: 10.3390/rs10121924.

Xiao, Y., W. Zhao, D. Zhou, and H. Gong (2014). "Sensitivity Analysis of Vegetation Reflectance to Biochemical and Biophysical Variables at Leaf, Canopy, and Regional Scales". In: *IEEE T. Geosci. Remote* 52.7, pp. 4014–4024. DOI: 10.1109/TGRS.2013.2278838.

Yallop, M. L., A. M. Anesio, R. G. Perkins, J. Cook, J. Telling, D. Fagan, J. MacFarlane, M. Stibal, G. Barker, C. Bellas, A. Hodson, M. Tranter, J. Wadham, and N. W. Roberts (2012). "Photophysiology and albedo-changing potential of the ice algal community on the surface of the Greenland ice sheet". In: *ISME J.* 6, pp. 2302–2313. DOI: 10.1038/ismej.2012.107.

Zege, E., I. Katsev, A. Malinka, A. Prikhach, and I. Polonsky (2008). "New algorithm to retrieve the effective snow grain size and pollution amount from satellite data". In: *Ann. Glaciol.* 49, pp. 139–144. DOI: 10.3189/172756408787815004.

Zege, E. P., I. L. Katsev, A. V. Malinka, A. S. Prikhach, G. Heygster, and H. Wiebe (2011). "Algorithm for retrieval of the effective snow grain size and pollution amount from satellite measurements". In: *Remote Sens. Environ.* 115, pp. 2674–2685. DOI: 10.1016/j.rse.2011.06.001.

Zhang, C., E. Pattey, J. Liu, H. Cai, J. Shang, and T. Dong (2017). "Retrieving Leaf and Canopy Water Content of Winter Wheat Using Vegetation Water Indices". In: *IEEE J. Sel. Top. Appl.* 99, pp. 1–15. DOI: 10.1109/JSTARS.2017.2773625.

Zhang, Q. X., Q. B. Li, and G. J. Zhang (2011). "Scattering impact analysis and correction for leaf biochemical parameter estimation using VIS-NIR spectroscopy". In: *Spectroscopy* 26, pp. 28–39.

# Acknowledgments

After an intensive final phase of my PhD, I would like to take this opportunity to thank all the people who supported me during my years as a PhD student and especially during the preparation of this thesis.

Special thanks go to my supervisor and second reviewer Prof. Dr. Luis Guanter, whose professional competence, conceptual advice and valuable support played a major role in the success of this work.

I would like to thank Prof. Dr. Jürgen Fischer for taking over the initial review and for his dedicated help with the formalities, and Dr. René Preusker for providing so much valuable feedback and for always taking time for my questions.

I would also like to thank all my colleagues at the Remote Sensing and Geoinformatics Section of the German Research Centre for Geosciences in Potsdam for their inspiration, helpfulness and pleasant working atmosphere.

Further special thanks go to my colleagues at the NASA Jet Propulsion Laboratory for giving me the opportunity to spend several months at their institute working on my thesis. In particular, I would like to thank Dr. David Thompson and Dr. Nimrod Carmon for their valuable input regarding conceptualization and methodology. I would also like to thank Dr. Robert Green for providing all the hardware and office equipment, and the entire imaging spectroscopy and SBG research topics group for all the worthwhile discussions. Additionally, my thanks go to Dr. Thomas Painter for his support and advice in the field of snow spectroscopy.

I would also like to thank my parents for their financial and moral support during my studies and beyond. In particular, the freedom to make groundbreaking decisions on my own has contributed not least to my successful doctorate.

Most importantly though, I thank Claudia for putting her own interests aside more than once to support and motivate me. Her relief has been most valuable for the success of the thesis, both in good and in bad times.